DEVELOPMENT OF TRANSPORT MODEL FOR WHOLE CORE PIN BY PIN CALCULATION IN 2D GEOMETRY

By

SUHAIL AHMAD KHAN

Enrolment No: PHYS01201004016

BHABHA ATOMIC RESEARCH CENTRE

A thesis submitted to the

Board of Studies in Physical Sciences

In partial fulfillment of requirements

for the Degree of

DOCTOR OF PHILOSOPHY

of

HOMI BHABHA NATIONAL INSTITUTE

August 2017

Homi Bhabha National Institute

Recommendations of the Viva Voce Board

As members of the Viva Voce Board, we certify that we have read the dissertation prepared by **Suhail Ahmad Khan** entitled **"*Development of Transport Model for Whole Core Pin-by-Pin Calculation in 2D Geometry*"** and recommend that it may be accepted as fulfilling the dissertation requirement for the Degree of Doctor of Philosophy.

P Krishnani. **Date: 01/08/2017**

Chairman- **Prof. P. D. Krishnani**

Umasankari Kannan **Date: 01/08/2017**

Guide / Convener- **Prof. Umasankari Kannan**

Date: 01/08/2017

External Examiner- **Prof. P. Mohanakrishnan**

Date: 01/08/2017

Member 1- **Prof. S. B. Degwekar**

I concur with the recommendation of the viva voce Committee.

Date: 01/08/2017

Member 2- **Prof. K. Devan**

V. Jagadeesan **Date: 01/08/2017**

Technology Adviser - **Dr. V. Jagannathan**

Final approval and acceptance of this dissertation is contingent upon the candidate's submission of the final copies of the dissertation to HBNI.

I hereby certify that I have read this dissertation prepared under my direction and recommend that it may be accepted as fulfilling the dissertation requirement.

Date: 01/08/2017

Place: Mumbai

Umasankari Kannan

Prof. Umasankari Kannan

(Guide)

0

STATEMENT BY AUTHOR

This dissertation has been submitted in partial fulfillment of requirements for an advanced degree at Homi Bhabha National Institute (HBNI) and is deposited in the Library to be made available to borrowers under rules of the HBNI.

Brief quotations from this dissertation are allowable without special permission, provided that accurate acknowledgement of source is made. Requests for permission for extended quotation from or reproduction of this manuscript in whole or in part may be granted by the Competent Authority of HBNI when in his or her judgment the proposed use of the material is in the interests of scholarship. In all other instances, however, permission must be obtained from the author.

(Suhail Ahmad Khan)

DECLARATION

I, hereby declare that the investigation presented in the thesis has been carried out by me. The work is original and has not been submitted earlier as a whole or in part for a degree / diploma at this or any other Institution / University.

(Suhail Ahmad Khan)

LIST OF PUBLICATIONS ARISING FROM THE THESIS

Journal

1. ***Suhail Ahmad Khan***, V. Jagannathan, Usha Pal, R. Karthikeyan and Argala Srivastava, "Need for High Temperature Nuclear Data Library for LWR Design Computations", *Journal of the Korean Physical Society*, Vol. 59, No. 1, July 2011 *[DOI: 10.3938/jkps.59.1073]*

2. ***Suhail Ahmad Khan***, Arvind Mathur and V. Jagannathan, "Incorporation of Interface Current Method Based on 2D CP Approach in VISWAM Code System for Hexagonal Geometry", *Annals of Nuclear Energy* **92**,161 *[DOI:* 10.1016/j.anucene.2016.01.041]

3. ***Suhail Ahmad Khan***, V. Jagannathan, Umasankari Kannan and Arvind Mathur, "Study of VVER-1000 OECD LEU and MOX Computational Benchmark with VISWAM Code System", *Nuclear Energy and Technology **2**, 312-334 [DOI: 10.1016/j.nucet.2016.11.008]*

4. ***Suhail Ahmad Khan***, V. Jagannathan and Umasankari Kannan, "Rotational Symmetry Boundary Condition in Current Coupled Whole Core Pin by Pin Transport Theory Code", *Journal of Nuclear Energy Science & Power Generation Technology, Vol 5, Issue 6, 2016 [DOI: 10.4172/2325-9809.1000170]*

5. ***Suhail Ahmad Khan***, Umasankari Kannan and V. Jagannathan, "Development of Whole Core Pin by Pin Transport Theory Model in Hexagonal Geometry", *Annals of Nuclear Energy* **104**, 214 *[DOI:* 10.1016/j.anucene.2017.02.012]

6. Arvind Mathur, Suneet Singh, ***Suhail Ahmad Khan*** and V. Jagannathan, "Analysis of the 2-D C5G7 MOX Benchmark with VISWAM Code", *International Journal of Nuclear Energy Science and Engineering, Vol. 5, 2015[DOI: 10.14355/ijnese.2015.05.003]*

Conference Publications:

1. ***Suhail Ahmad Khan,*** Arvind Mathur and V. Jagannathan, "Using Collision Probability Technique for analysis of HTTR Benchmark", in *ANS MC2015 - Joint International Conference on Mathematics and Computation (M&C), Supercomputing in Nuclear Applications (SNA) and the Monte Carlo (MC) Method* Nashville, TN April 19-23, 2015, American Nuclear Society, LaGrange Park, IL (2015) – *Paper Accepted for Oral Presentation*
2. Arvind Mathur, Suneet Singh, ***Suhail Ahmad Khan*** and V. Jagannathan, "Analysis of LEU Pincell and Assembly Benchmark using VISWAM", *Paper presented in winter meeting of American Nuclear Society (2015)*

Other Publications:

1. ***Suhail Ahmad Khan***, Arvind Mathur and V. Jagannathan, "Development of Interface current Method based on 2D Collision Probability for 2D Hexagonal Geometry", BARC External Report BARC/2015/E/012

(Suhail Ahmad Khan)

Dedicated To

Ammi and Abba

ACKNOWLEDGEMENTS

First and foremost, my praises and thanks go to the all Almighty ALLAH for His showers of blessings throughout this research work and giving me strength to complete this work successfully. My special thanks go to my mother. It would have become impossible to complete this work without her constant support.

I would like to express my deep and sincere gratitude to my current research guide Prof. Umasankari Kannan and former guide and present technology adviser Dr. V. Jagannathan for their constant support and encouragement. This work would not have been possible without their tireless efforts. They were always available despite their busy schedules with their invaluable constructive comments and suggestions throughout the thesis work and have made this research and thesis work successful and presentable in this form.

I would like to thank my doctoral committee members Prof. P. D. Krishnani, Prof. S. B. Degwekar and Prof. K. Devan for their encouragement and suggestions for the successful completion of the thesis work.

I am thankful to my former colleague Cdr. Arvind Mathur for very fruitful discussions, specially, during the development of lattice module of the present study. His queries and parallel development gave the requisite confidence to move ahead. Thanks are due to my colleague Amod Kishore Mallick for useful discussions.

I want to thank all the researchers whose work I have consulted and cited. Though I have not met many of them personally, but their works were very useful during the course of this study.

I want to thank all the people whose contributions to this work I have missed. The direct or indirect support from BARC and HBNI is gratefully acknowledged.

Finally, I would like to thank each member of my family, my parents, my brothers and sisters who were always there to help me whenever I needed it. I would not have completed this work without their help and support. Thank you very much to all of you for being always there for me.

(Suhail Ahmad Khan)

CONTENTS

Page Number

SYNOPSIS

The reactor physics calculations of nuclear reactor core are traditionally performed in two steps. First, the isolated heterogeneous fuel assembly (FA) is treated in detail using multigroup transport theory. This calculation is performed with reflective or zero leakage current boundary condition. Few group homogenized parameters of FA are generated as a result of this calculation. These parameters are used to perform core calculations using traditional finite difference or nodal methods employing diffusion theory. This averaging of the individual FA cell and neutronics properties assumes zero flux gradient at assembly interfaces which is not fully correct as the fuel assemblies in operating reactors are invariably of different enrichments with UOX or MOX type, different fuel burnup and may contain water rod / control absorber rod cells, burnable absorbers of gadolinium or boron type. The few-group homogenized parameters depend on non-local history effects as the fuel burnup is strongly dependent on the spatial neutron spectrum history as well as non-linear neighbor effects arising due to changes in the intra-assembly and intra-group spatial flux gradients caused by changes in the neighboring fuel assemblies or cells such as control rod insertion etc [1]. Also, the micro pin level flux distribution and hot spot thereof are lost in final core calculation and the core results represent average core behavior only.

The safety limitations in a reactor calculation can be relaxed by the application of the advanced core analysis method with higher prediction accuracy [2]. Since the prediction error of such a core analysis code would be smaller compared to the traditional diffusion theory based codes, the design safety margin for an advanced core calculation method can be reduced. When the safety limitations are relaxed, more aggressive fuel loading pattern, which cannot be adopted with the utilization of conventional core analysis method, can be designed thereby increasing the

efficiency of nuclear power generation through reducing fuel cycle cost and increasing plant capacity factor. For these reasons and as a consequence of the heterogeneities described earlier and also to decrease and quantify the uncertainties of the numerical simulations for safety relevant phenomena, there is a need to develop core simulation methods which are based on transport theory and use fine scale discretisation in neutron energies and space.

The objective of this dissertation is to develop a core simulation method that is based solely on transport theory and does not require homogenization of fuel assembly or use of discontinuity factors. For this purpose, we have examined the possibility to use the interface current method based on 2D collision probability theory to study the reactor performance and safety analysis and fuel cycle evaluations for reactor cores employing hexagonal geometry. The other notable codes with the capability to perform 2D whole-core transport calculations are CASMO [3], CRX [4], DeCART [5], PARAGON [6], APOLLO2 [7] and MOCUM [8]. All of these codes except PARAGON use the method of characteristics (MOC) as transport solver. PARAGON employs the interface current method in 2D square geometry. The application of interface current method to perform large whole core pin by pin simulation in hexagonal geometry is novel and not reported in literature and is being done for the first time.

It is observed that the application of 2D CP method for analysis of complex and large cores will ensure increased accuracy and hence would provide a faster and much simpler alternative when compared to much more complicated neutronic computer codes in addressing the feasibility and effectiveness of fuel cycle strategies. The thesis consists of six chapters

Chapter 1 gives the brief introduction and approach to perform reactor core calculations. The need to perform the detailed pin by pin simulation of reactor core and basis to select the interface current method based on 2D collision probability for whole core simulation in 2D

hexagonal geometry is also described. The extant international neutronic codes with the capability to perform full core simulations in 2D geometry are presented in this chapter.

Chapter 2 gives the detailed mathematical description of interface current method based on 2D collision probability. A transport theory code TRANPIN is developed to perform the whole core pin by pin calculation in 2D hexagonal geometry. In the traditional pin by pin analysis, the fuel pin or other heterogeneous cells present in the fuel assembly are homogenized and treated as single mesh. In the present method, the lattice cell is not homogenized. The heterogeneous lattice structure of fuel rod and absorber rod cells are sub divided into finer regions. The transport equation for the full core is solved using the interface current method based on 2D collision probability (CP) method. In the interface current method, the problem domain is split into smaller heterogeneous lattice cells. Here the unit entity is lattice cell consisting of a single fuel or absorber rod and its associated coolant. Each lattice cell is divided into several sub regions. The external boundary of lattice cell is divided into a set of finite surfaces. The zone to zone coupling in the lattice cell is achieved using region to region CPs. The coupling between the cells in the same FA and cells of different FAs is achieved by expanding the angular flux leaving or entering a lattice cell into a finite set of linearly independent functions. We have used a double P_2 (DP2) expansion of angular flux in the half space created by each surface of lattice cell. The approach to perform the whole core pin by pin calculation is developed in two steps. As a first step, the interface current method is applied on a single fuel assembly. This is required because, although 2D CP method is used in codes like CLUB [9], WIMS [10], HELIOS [11] etc, the use of DP2 expansion for hexagonal lattice assembly is not reported in literature. This methodology was developed for a single FA and incorporated in the

lattice analysis code VISWAM. After benchmarking and validating the lattice level results, the method was extended to perform the pin by pin whole core calculation.

Chapter 3 gives the results of benchmarking and validation exercise of application of interface current method at lattice level. The implementation of interface current method in lattice analysis code VISWAM was benchmarked against a simplified heterogeneous benchmark problem that is typical of a high temperature reactor [12]. The primary aim of the benchmark is to assess the accuracy of diffusion or transport methods for reactor calculations. The benchmark is derived from the experimental data of High Temperature Engineering Test Reactor (HTTR) start-up experiments. The benchmark provides the six group macroscopic cross section for all the materials required. The interface current method in VISWAM code was further developed for a detailed burnup analysis of an FA cell. The burnup strategy used in VISWAM code was validated using the theoretical Computational Benchmark of VVER-1000 OECD LEU and MOX FA cells [13]. This benchmark has been proposed to certify the lattice calculation codes for utilizing weapons grade plutonium by converting it to mixed-oxide (MOX) fuel for nuclear reactors. The benchmark model consists of two different assemblies of low enriched uranium (LEU) and MOX that are typical of the advanced designs for the VVER-1000 reactors. The multiplication factor with burnup, fission density distribution and cell averaged isotopic densities are compared and discussed in this chapter. The results obtained using DP2 expansion show least deviation from benchmark mean values. The reactivity loads of (Xe, Sm) and isothermal temperature show an improved prediction by DP1/DP2 models. The detailed results are presented in this chapter.

Chapter 4 gives the scheme and methodology of interface current method used in whole core calculation code TRANPIN. The spatial discretisation of whole core using fine meshes, the

numbering scheme of the meshes, connectivity of the meshes and iteration scheme adopted for the solution method are presented in detail. When the fine energy group structure is used for core calculation, the whole core simulation was seen to be a formidable task demanding very large computer storage and CPU time. The calculation could be performed by using inherent symmetry available in the core geometry. For this purpose a 60° rotational symmetry was introduced in TRANPIN. The methodology to use rotational symmetry boundary condition is also described.

In Chapter 5, the results of benchmarking exercise of TRANPIN code are presented. The code TRANPIN has been validated against two benchmark problems i) a simplified high temperature engineering test reactor (HTTR) benchmark problem [14] and ii) OECD VVER-1000 MOX Core Computational Benchmark [15]. The HTTR benchmark, a heterogeneous 2D problem in hexagonal geometry, is proposed to test the accuracy of modern transport methods for neutronics analysis. This problem was derived from the High Temperature Engineering Test Reactor start-up experiment and is a simplified benchmark problem which is obtained by removing the detailed design specific material and structural details of HTTR while retaining the heterogeneity and major physics properties from the neutronics viewpoint. The benchmark provides the 6-group, transport corrected macroscopic cross section library for four fuel types corresponding to the four enrichment levels considered in the core, four graphite cross sections (corresponding to graphite in fuel blocks, in control rod blocks, and in permanent and replaceable reflector blocks), and cross sections for burnable poison pins and control rods which had been obtained by a detailed lattice calculations using HELIOS code system.

TRANPIN code has been validated against the OECD VVER-1000 MOX Core Computational Benchmark. This benchmark is proposed to investigate the physics of a VVER-

1000 reactor whole core using two-thirds LEU and one-third MOX fuel assemblies and for certification of calculation codes for future MOX fuel utilization in VVER-1000 reactors. This is required due to essential differences in physics behavior of MOX and standard LEU fuels. The benchmark model consists of a full-size 2-D VVER-1000 core with heterogeneous 30% MOX-fuel loading. The core consists of 28 FAs considered in 60° rotational symmetry. The system has an infinite axial dimension and vacuum boundary condition is applied on the side surface. The core is surrounded by a reflector. The reflector is a very complicated structure consisting of a thin film of water gap, steel baffle with water holes, steel barrel, down comer water and steel pressure vessel. The equilibrium VVER-1000 core structure has been simplified in order to consider only two types of fuel assemblies with a fixed set of burn-ups. UOX FAs have average fuel burn-ups of 0, 15, 32 and 40 MWd/kg, and MOX FAs have average fuel burn-ups of 0, 17 and 33 MWd/kg. The benchmark provides the isotopic composition of all the fuel materials at each burnup and various structural materials like clad, guide tube, borated coolant, steel baffle, steel barrel and steel vessel required in the problem. It is to be noted that the OECD benchmark is analyzed using ultra fine WIMS library 'HTEMPLIB' in 172 energy groups for first time using CP method. This approach is novel since the full core calculations are normally performed with cross sections prescribed in few energy groups by energy condensation using some prior transport simulations. The 172 group cross sections of fuel rings and structural materials of core and reflector zones were generated by VISWAM code and were used for core calculations in TRANPIN.

The core k_{eff} obtained using DP2 calculation shows an improved agreement with benchmark results compared to DP0/DP1 result for HTTR analysis. The δk_{eff}, w.r.t benchmark, obtained using DP2 is seen 0.0091 as compared to 0.0192/0.0143 for DP0/DP1 calculation.

The %RMS deviation in block averaged fission density distribution is seen as 0.77%, 0.42% and 0.47% for DP0, DP1 and DP2 calculation respectively. In the OECD VVER-1000 MOX Core Computational Benchmark analysis, the assembly averaged fission density distribution is significantly improved using DP1 model. The detailed discussion of these results is presented in this chapter. Chapter 6 gives the conclusion and summary of the present research. The feasibility of using interface current method based on 2D collision probability, obtained using DP2 expansion of angular flux, is demonstrated for single lattice fuel assembly cell and whole core calculation in 2D hexagonal geometry. The broad observations and scope for future work is discussed in this chapter. The list of publications arising out of this thesis work is given in the end.

References:

1. Aragones J. M., Diop C., Rohde U., "Status and limits of current methods for plant analysis", Nuclear Reactor Integrated Simulation Project (NURISP) – Document D-1.0 (issued on 22/3/2010).
2. Tada K., "Study on pin-by-pin fine mesh core calculation method for BWR core analysis," Ph.D. thesis, Nagoya University, (2012).
3. Smith K.S. and Rhodes III J.D., "Full-Core, 2-D, LWR Core Calculations with CASMO-4E," *Proc. Int. Conf. on Reactor Physics Safety and High-Performance Computing (PHYSOR 2002)*, Seoul, Korea, 7-10 October, 2002 (2002).
4. Cho N.Z., Lee G.S., Hong S.G., Jo C.K. and Lee K.T., "Whole-Core heterogeneous transport calculations and their comparisons with diffusion results," *Trans. Am. Nucl. Soc*., **83**, 292 (2000).

5. Cho J Y., Kim K S., Shim H J., Song J S., Lee C C. and Joo H G., "Whole Core Transport Calculation Employing Hexagonal Modular Ray Tracing and CMFD Formulation," *Journal of Nucl. Sci. and Technology*, **45**, 740-751 (2008).
6. Kucukboyaci V.N., Ouisloumen M., and Franceschini F., "Two-Dimensional Whole Core Transport calculations using PARAGON," *Proc. Int. Conf. on Mathematics,Computational Methods & Reactor Physics (M&C 2009)*, Saratoga Springs, New York, May 3-7, (2009).
7. Huot N., Aggery A., Blanchet D., D'Aletto C., Di Salvo J., Döder-lein C., Sireta1 P. and Willermoz G., "The JHR Neutronics Calculation Scheme Based on the Method of Characteristics," *Proc. Int. Top. Mtg. on Mathematics and Computation, Supercomputing, Reactor Physics and Nuclear and Biological Applications (M&C 2005)*, Avignon, France, Sept 12-15, 2005. (2005).
8. Yang X. and Satvat N., "MOCUM: A two-dimensional method of characteristics code based on constructive solid geometry and unstructured meshing for general geometries", *Ann. Nucl. Energy*, 46, 20, (2012).
9. Krishnani P. D., "CLUB—A multigroup integral transport theory code for analysis of cluster lattices", *Ann. Nucl. Energy*, 9, 255, (1982).
10. Askew, J.R., Fayer, F.J., Kemshell, P.B., "A general description of lattice code WIMSD", Journal of the British Nuclear Energy Society (1966).
11. Villarino E.A., Stamm'ler R.J.J., Ferri A.A., Casal J.J., "HELIOS: angularly dependent collision probabilities" *Nucl. Sci. Eng*. 112, 16–31 (1992).
12. Zhang Z., Rahnema F, Zhang D., Pounders J.M., Ougouag A.M., "Simplified two and three dimensional HTTR benchmark problems", *Ann. Nucl. Energy,* 38, 1172 (2011).

13. A VVER-1000 LEU and MOX Assembly Computational Benchmark, NEA/NSC/DOC (2002)10, (2002).
14. Zhang Z., Rahnema F., Pounders J. M., Zhang D. and Ougouag A. "A Simplified 2D HTTR Benchmark Problem", *Proc. Int. Conf. on Mathematics,Computational Methods & Reactor Physics (M&C 2009)*, Saratoga Springs, New York, May 3-7, 2009. (2009)
15. VVER-1000 MOX Core Computational Benchmark, NEA/NSC/DOC 17 (2005).

LIST OF FIGURES

LIST OF TABLES

CHAPTER – 1

INTRODUCTION

1.1 Background

India is pursuing an active three stage nuclear power program. There are presently 21 nuclear power reactors in operation with an installed capacity of 5780 MW [1]. This includes the developed PHWR–220/540, BWR–160 and VVER–1000 MWe reactor. Four units of 700 MWe PHWR, one unit of 500 MWe PFBR and another unit of VVER–1000 MWe reactor in collaboration with Russia at Kudankulam are in an advanced stage of construction and commissioning. Four more units of VVER–1000 MWe reactor are planned at Kudankulam.

India plans to augment its installed capacity to 63,000 MW by 2032 [2]. The capacity addition plan in the medium term for reaching a capacity of 63,000 MW by 2032 envisages addition of indigenous PHWRs with capacity of 4200 MW (6X700) based on natural uranium, 7000 MW from PHWRs based on reprocessed uranium from LWR spent fuel, 40000 MW from imported LWRs and the balance through 500 MW/1000 MW FBRs. Other reactors like the 300 MWe Advanced Heavy Water Reactor (AHWR), a technology demonstrator for thorium utilization and Indian LWR under development are also planned [2]. India is also carrying out the design of an innovative 600 MWth high temperature reactor (HTR) for commercial hydrogen production.

The LWRs to complete the planned target of 40000MW are expected to be advanced Generation III reactors such as AP1000, EPR, VVER-1200, ESBWR etc. The physics simulation and analysis of these reactors is very challenging due to their complex design. To cater to the challenging physics design requirements of the operating, imported and/or indigenous reactor developments, there is a need to develop indigenous state of the art computational capability.

The reactor physics calculation of nuclear reactor core pertains to the estimation of neutron flux distribution in the reactor system. The neutron distribution in a reactor system is described by the steady state Boltzmann transport equation. The integro–differential form of Boltzmann transport equation is given by

$$\overrightarrow{\Omega}.\,\vec{\nabla}\phi\left(\vec{r},\overrightarrow{\Omega},E\right)+\ \Sigma_t(\vec{r},E)\phi\left(\vec{r},\overrightarrow{\Omega},E\right)=\frac{\chi}{k_{eff}}\int dE'\int d\Omega'\,\Sigma_f(\vec{r},E')\phi\left(\vec{r},\overrightarrow{\Omega'},E'\right)+$$

$$\int dE'\int d\Omega'\,\Sigma_s\left(\vec{r},\overrightarrow{\Omega'}\rightarrow\overrightarrow{\Omega},E'\rightarrow E\right)\phi\left(\vec{r},\overrightarrow{\Omega'},E'\right). \qquad (1.1)$$

where $\vec{r},\overrightarrow{\Omega},E$ represent space, angular direction and energy respectively. Σ_t and Σ_f are the total and fission neutron cross sections respectively and ϕ represents the neutron flux distribution. χ is the normalized fission spectrum, and k_{eff} is the effective neutron multiplication factor or eigenvalue of the system.

The reactor physics calculations are traditionally performed in two steps. First, the isolated heterogeneous fuel assembly (FA) is treated in detail and Eq. (1.1) is solved in multigroup formalism for the 2D FA. This full or symmetric part of FA calculation is performed with reflective or zero leakage current boundary condition. Few group homogenized parameters of FA are generated as a result of this calculation. These parameters are used to perform core calculations using traditional finite difference or nodal methods employing diffusion theory. This averaging of the individual FA cell and neutronics properties assumes zero flux gradient at assembly interfaces which is not a true representation as the fuel assemblies in operating reactors are invariably of different enrichments with UOX or MOX type, different fuel burnup and may contain water rod/control absorber rod cells, burnable absorbers of gadolinium or boron type. The few-group homogenized parameters depend on non-local history effects such as the fuel burnup which is strongly dependent on the spatial neutron spectrum history as well as non–linear

neighbor effects arising due to changes in the intra–assembly and intra–group spatial flux gradients caused by changes in the neighboring fuel assemblies or cells such as control rod insertion etc [3]. Also, the micro pin level flux distribution and hot spot thereof are lost in final core calculation and the core results represent average assembly behavior only.

As a consequence of these heterogeneities, and to decrease and quantify the uncertainties of the numerical simulations for safety relevant phenomena, there is a need to develop core simulation methods that cover several scales in neutron energies and space. The safety limitations in a reactor calculation can be reliably assured or relaxed by the application of the advanced core analysis method with higher prediction accuracy [4]. Since the prediction error of such a core analysis code would be smaller compared to the traditional diffusion theory based codes, the design safety margin for an advanced core calculation method can be reduced. When the safety limitations are ensured, more aggressive fuel loading pattern, which cannot be adopted with the utilization of conventional core analysis method, can be designed thereby increasing the efficiency of nuclear power generation through reducing fuel cycle cost and increasing plant capacity factor. For these reasons and to remove the approximations associated with traditional diffusion theory codes, there is a need to develop core simulation methods which are solely based on transport theory and use fine scale discretisation in neutron energies and space. The application of advanced transport methods for whole core reactor simulation without the intermediate homogenization has become feasible owing to the availability of high speed (a few GHz) large memory (terra bytes) computers and parallel processing algorithms.

1.2 Present Status of Simulation Methods in India

In India for the simulation of thermal reactors the traditional two step core simulation approach is followed currently. The history of the development and usage of this methodology

spans four decades in which many lattice and core level computational tools have been developed. The current status of lattice level and core analysis developments is presented in the following sections.

1.2.1 Lattice Calculation Codes

The following lattice simulation codes have been developed and are being used to perform detailed burnup dependent fuel assembly/cluster calculations.

EXCEL: The lattice burnup code EXCEL [5], based on the combination of 1-D multi–group transport theory and 2–D few group diffusion theory, solves the FA cell problem in hexagonal geometry. The fuel pins in the FA are classified into pin cell types based on enrichment and Dancoff factors. The hexagonal pin cell boundary is cylindricalised to allow 1–D treatment of the Wigner–Seitz cell and uses the white boundary condition. The heterogeneities present in the FA cell such as water rods, burnable poison rods and control rods are treated by special 1–D super cell simulations. For 1–D transport, the code uses the first flight collision probability method. The 2–D fuel assembly cell is treated by few group diffusion theory using centre–mesh finite difference method. The EXCEL code can be used to obtain infinite neutron multiplication factor (k_∞), the few group homogenized lattice parameters of fuel assemblies in the hexagonal lattice and isotopic compositions as a function of burnup, boron in coolant, fuel temperature, moderator (coolant trapped in guide tubes/inter assembly gaps) temperature, coolant temperature/density, saturated xenon and samarium loads, in the absence/presence of control rods.

SUPERB: SUPERB is used to perform FA calculation in square geometry [6]. The solution method and basic approach in SUPERB is similar to EXCEL code system described above.

CLUB: CLUB is a multigroup integral transport theory code for analysis of cluster geometries [7]. CLUB is based on a combination of interface current method and the P_{ij} method. In this method the fuel cluster cell is divided into multiple fuel rings surrounded by annular homogeneous regions of pressure tube, air gap, calandria tube and moderator. Each fuel ring is divided into the individual homogeneous zones containing fuel pins, their clad and the associated coolant regions. The fuel zones can be optionally subdivided into more regions. Disjoint clad regions in the fuel ring are treated as a single region. The associated coolant region can be subdivided by input specification into multiple concentric ring regions. It is assumed that the ring contains same type of fuel rods. The interaction between zones within a ring is obtained using the P_{ij} method. The interaction between the fuel ring regions of the cluster and the outer homogeneous annular regions of PT/Air Gap/CT and moderator regions are obtained using interface currents.

RICANT: RICANT solves FA problem in square geometry. The one–zone rectangular cells in the 2–D FA are solved using interface current method [8]. The interface currents are obtained by expanding the angular flux in un–normalized double P2 expansion functions. The angular flux expansion functions consider all the six terms in the expansion.

LWRBOX: LWRBOX treats the FA problem in square geometry using the interface current method as flux solver [9]. In this method, the lattice cell is divided into several connected cells which can further be subdivided into homogeneous zones. The interaction between various zones within a cell and their contribution to outgoing currents at region interfaces are directly calculated by the CP method [9].

VISWAM: The lattice analysis code VISWAM has been developed with an aim to unify computational tools into a single package [10]. VISWAM can be used to study the lattice FAs in

square, hexagonal and ring cluster geometries. VISWAM has been developed completely in modular structure in FORTRAN 90. Initially, the calculation method adopted in VISWAM was similar to the EXCEL/SUPERB. New calculation modules were added to VISWAM, the details of which are described later.

In addition to these indigenous codes, some international codes such as WIMSD5 are also used to perform lattice calculations.

1.2.2 Core Calculation Codes

The following 3D core calculation codes have been developed and are being used to perform 3D core analysis for various reactor applications.

TRIHEXFA: TRIHEXFA is a few group 3D diffusion theory code for simulating reactor cores in hexagonal geometries [11]. The large hexagonal FA is divided into $6n^2$ triangular meshes, where n is the number of equal divisions on a side of the hexagon. Triangular mesh description of the core is obtained by an auto triangularization procedure by the code itself. TRIHEXFA code reads the few group cross section files generated by EXCEL code for each FA type as a function of burn-up, boron and other reactor state parameters. For a given problem the user needs to specify essentially the core power, flow, burn-up state, coolant temperature, control device configuration etc. The program recognizes the zone of influence of a control device and appropriate control perturbations are taken into account. Space or power dependent cross section perturbations due to saturated Xenon, Sm, Doppler, coolant temperature and density are modeled in five energy group simulations. TRIHEXFA is used for the fuel cycle analysis of 1000 MWe VVER core.

CEMESH/COMESH: CEMESH/COMESH codes are used to perform 3D core calculations for square geometries such as PHWR [12, 13]. COMESH is a corner mesh finite

difference code. It can simulate reactivity devices explicitly using $\alpha = J/\phi$ type boundary conditions in two energy groups. CEMESH code is a centre-mesh finite difference code. It uses the two group lattice parameter database generated by PHANTOM code system [13] for PHWR fuel clusters as a function of burnup, soluble boron in moderator, coolant/moderator temperature, moderator purity values, fuel temperature, saturated xenon and various types of control type perturbations. PHANTOM–CEMESH code system has been validated against the Phase–B physics experiments of NAPS, KAPS reactors and their operational data as a function of core burnup.

HEXPIN: The code HEXPIN has been developed for reactor core analysis with a pincell size mesh description up to pressure vessel in hexagonal geometry [14]. HEXPIN uses the centre mesh finite difference method to solve 3D diffusion equation in few groups. The input to HEXPIN code consists of fuel assembly type disposition in the core. The geometrical disposition of fuel and non–fuel cells within each fuel assembly is constructed by HEXPIN using the output of hexagonal lattice cell burnup code EXCEL for each fuel assembly type.

FEMINA: The 3D diffusion theory code FEMINA uses the flux expansion method [15]. It is a 3D diffusion theory based code for Cartesian geometries. Here the 3D diffusion equations are integrated in the transverse direction and the resulting set of 1-D equation are then solved. The partially integrated fluxes are expanded in terms of local higher order polynomials. The polynomial expansion allows one to use coarser meshes in large sized cores.

ATES3: ATES3 (**A**nisotropic **T**ransport **E**quation **S**olver in **3**D) is an indigenously developed neutral particle transport code in 3-Dimensional Cartesian XYZ geometry [16]. It solves steady state forms of linear multi-group neutron transport equation by discrete ordinates (S_N) method. The spatial variable is discretised by finite difference approximation along with the

well–known Diamond Difference scheme. The angular variable is discretised into discrete directions. The code can handle isotropic as well as anisotropic scattering. It has options to use conventional solution algorithms as well as some modern computational techniques based on Krylov Sub–space methods.

ARCH: ARCH code (Analysis of Reactor Transients in Cartesian and Hexagonal Geometries) solves the neutron diffusion equation in 3D Cartesian and triangular geometry [17]. The solution is performed in few neutron energy groups using Finite Difference Method (FDM). The discretised diffusion equation results in a large linear system of equations in the form of AX = B, which is solved by conventional as well as advanced Krylov Subspace algorithm based schemes.

1.3 Whole Core Pin–by–Pin Simulation without Homogenization

The various core simulation codes described in Section 1.2.2 need few group homogenised parameters obtained using prior isolated transport calculation of a single FA cell. This is true both for core calculation methods based on either assembly homogenization as shown in Fig. 1.1(a) or pin homogenization shown in Fig. 1.1(b). As described in Section 1.1, this transport calculation is performed with reflective/rotational symmetry boundary or zero leakage current boundary condition. The limitations of this calculation have been discussed in detail in Section 1.1. In the recent times, there is a phenomenal improvement in computer processing power. Massive parallel computer with thousands of processors are now available. This has encouraged the development of accurate models for whole core pin–by–pin calculation. The objective of this dissertation is to develop a core simulation method that is based solely on transport theory and does not require homogenization of fuel assembly or use of discontinuity factors. For this purpose, a new transport theory code TRANPIN has been developed to perform

the whole core pin-by-pin calculation in 2D hexagonal geometry. TRANPIN solves the transport equation for the full core using the interface current method based on 2D collision probability (CP) method. Many international labs are engaged in developing the detailed and precise whole core transport theory models in 2D and 3D geometries [18]. Before describing the details of TRANPIN code system, the following section describes in brief the present international status of 2D whole core calculation efforts. The discussion on 3D development is not presented as it is beyond the scope of this thesis work.

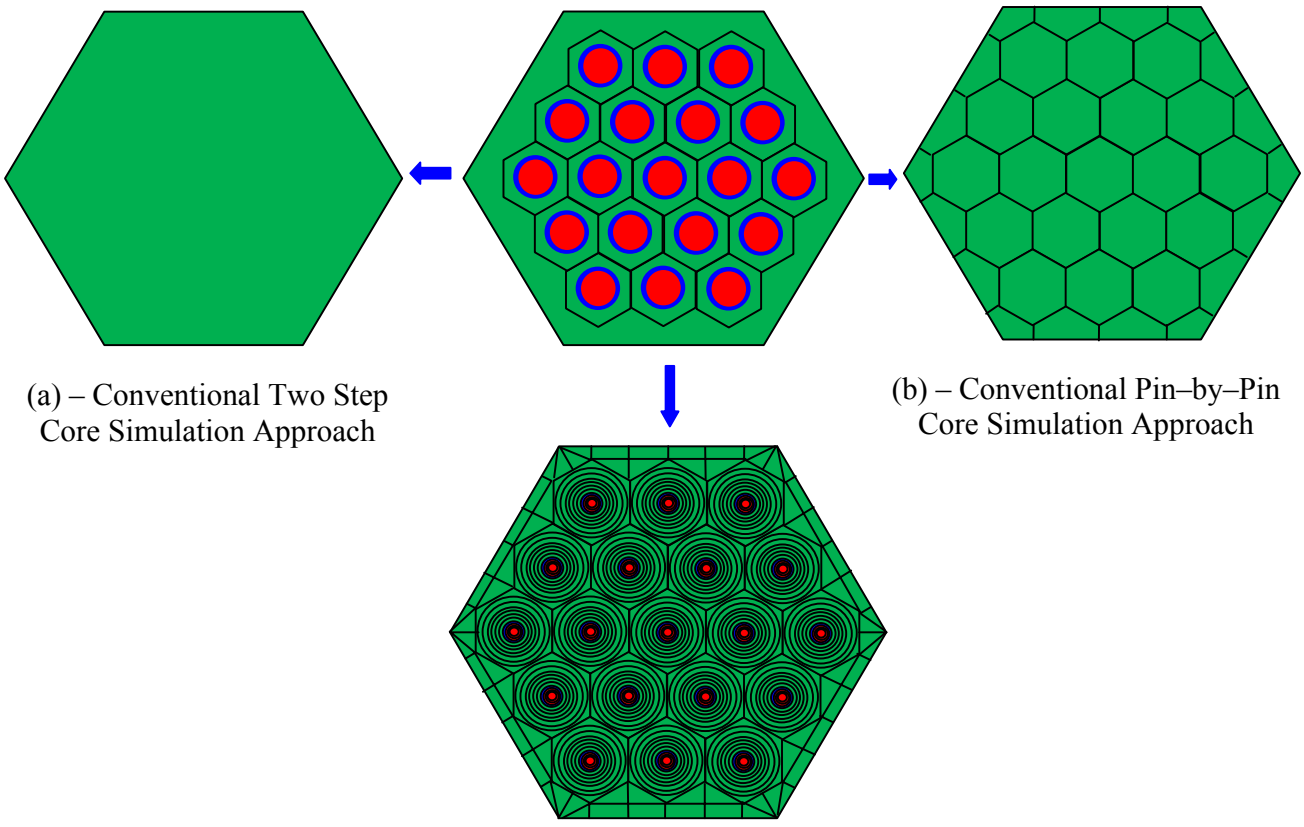

Fig. 1.1 – Comparison of Geometry Discretization in TRANPIN with other Core Simulation Methods

1.3.1 Literature Survey

A detailed literature survey has been done to assess the methodologies developed elsewhere in the world. The following codes are capable of performing 2D whole core calculations [18]:

CASMO: CASMO is a lattice analysis code of Studsvik Inc. of USA which has been used for few group constant generation for BWR and PWR for 25 years [19]. In the recent version of CASMO, CASMO–4, the transport equation is solved using the Method of Characteristics (MOC) in 2D rectangular geometry with completely heterogeneous models up to pin level and used for whole core calculation [19, 20]. The assembly physical mesh is divided into ~5000 regions, with each pincell being split into radial and azimuthal zones [20]. Neutron sources in each zone are approximated as spatially flat and isotropic. The code has been applied and tested against BWR critical assembly geometry and quarter core model of full 2D BWR geometry in eight energy groups [20].

CRX: The Korean assembly calculation code CRX based on the method of characteristics has been extended to treat whole–core heterogeneous calculation [21]. For the heterogeneous transport calculation for such large scale problems, a modular ray tracing in which all lattice cells have the same ray distribution for each direction is used to reduce the computer memory requirement [21]. In this scheme, the ray tracing is performed for only different types of cells. The code has been used to analyse an 8X8 whole core problem consisting of MOX and UO2 fuel assemblies.

DeCART: DeCART code has been developed as part of a U.S.–Korean collaborative INERI project and solves the 2D and 3D whole core transport problem in square and hexagonal geometries [22, 23, 24]. In order to deal with the heterogeneity at the pin cell level, the two-

dimensional (2–D) Method of Characteristics (MOC) is used [22]. The 3–D whole core transport solution is obtained by 2–D/1–D coupling scheme which is realized within the framework of 3–D coarse mesh finite difference (CMFD) formulation which serves the dual functions of accelerating the 2–D radial MOC solutions [22]. The code employs the modular ray tracing scheme. The code has been tested against a number of numerical and critical benchmarks [23, 24].

PARAGON: PARAGON is Westinghouse's state–of–the–art code for two–dimensional lattice calculations. It is based on collision probability and interface current coupling methods and has the ability to solve problems with any size of spatial, angular, and energy discretization [25]. The 2D whole core capability of PARAGON has been tested against a two–dimensional PWR core model in square geometry and its ability to run large problems with increasing coupling–orders of the interface current method is demonstrated [25].

APOLLO2: The APOLLO2 spectral transport code, developed at the CEA France, is widely used for assembly cross section generation and direct transport calculations, including a large range of applications in reactor physics, criticality safety studies and fuel cycle analysis [26]. APOLLO2 flux solvers for 2D square and hexagonal FA geometry are based either on the collision probability method (CPM)–full CPM, interface-current techniques (ICT) and simplified ICT (multi cell methods)–or on different spatial discretization of the discrete ordinates form of the transport equation comprising finite differences, transverse nodal and short and long characteristics (MOC) methods [26]. The 2D whole core calculations with APOLLO2 make use of the MOC module. APOLLO2 whole core calculation has been benchmarked against 2D PWR and HTGR benchmarks [26].

MOCUM: The transport theory code MOCUM is based on the method of characteristics as the flux solver with an advanced general geometry processor for two–dimensional rectangular and hexagonal lattice and full core neutronics modeling [27]. The code uses unstructured meshes for spatial discretization of single pin, assembly and full core geometries. The code has been verified and validated against various benchmarks representing rectangular, hexagonal, plate type and CANDU reactor geometries.

1.3.2 Development of TRANPIN

All the codes except PARAGON listed in the previous section use MOC as transport solver. Due to the availability of computational resources, the methods based on collision probability (CP) have gained renewed interest. Altiparmakov et al [28] proposed a solution method that extends the capabilities of the collision probability approximation to large–size neutron transport problems and successfully applied it to a 2D model of a quarter core of a heavy water power reactor of CANDU type. Hemprabha et al. [29, 30] have recently applied the collision probability method to single pincell and multi–hexagonal assemblies in 3D geometry. It is planned to develop a 3D pin–by–pin transport theory code with fuel depletion capability to augment the indigenous core calculation capabilities described in Section 1.2 and meet the future challenges. As a first step to achieve this goal, a new transport theory code TRANPIN has been developed to perform the whole core pin–by–pin calculation in 2D hexagonal geometry. The following integral form of transport equation (described here in one group form for simplicity) is solved in TRANPIN for the large scale full core problem:

$$\phi\left(\vec{r},\overrightarrow{\Omega}\right) = \phi\left(\overrightarrow{r_S},\overrightarrow{\Omega}\right)e^{-\tau_S} + \frac{1}{4\pi}\int_0^{R_S} dR'\, q\left(\overrightarrow{r'}\right)e^{-\tau(R')}. \tag{1.2}$$

where $\overrightarrow{r_S} = \overrightarrow{r} - R_S\,\overrightarrow{\Omega}$ is an arbitrary point on the line passing through $\overrightarrow{r}$ in the direction $\overrightarrow{\Omega}$ on the surface S bounding the volume V, where boundary conditions will be applied and $\overrightarrow{r'} =$

$\vec{r} - R'\vec{\Omega}$. τ and τ_S are the optical distances between $\vec{r}$ and $\vec{r'}$ and between $\vec{r}$ and $\vec{r_S}$ respectively. The total source density $q(\vec{r})$ for a group of energy *E* is isotropic and defined as

$$q(\vec{r}) = \int dE' \Sigma_s(E' \to E)\phi(\vec{r}, E') + \frac{\chi(E)}{k_{eff}} \int dE' \nu\Sigma_f(E')\phi(\vec{r}, E'). \quad (1.3)$$

TRANPIN employs the interface current method based on 2D collision probability (CP) method for solving Eq. (1.2) for whole core reactor problem. The use of interface current method to perform large scale whole core calculations in hexagonal geometry is not reported in literature. A well known advantage of interface current method based on 2D CP compared to full CP method is that we need to calculate the dense region to region coupling matrices P_{ij} matrices only for distinct lattice cells in the whole core. The use of interface current method alleviates the very important problem of huge memory requirements that arise if a direct CP method is applied to treat large medium whole core problems. Also this reduction in the coupling of the spatial variables in the interface current method permits an iterative cell–by–cell solution.

In the traditional pin–by–pin analysis [14] as shown in Fig. 1.1(b), the fuel pin or other heterogeneous cells present in the FA are homogenized and treated as a single mesh. In the present method, the lattice cell is not homogenized. The heterogeneous lattice structure of fuel rod and absorber rod cells are sub divided into finer regions as shown in Fig. 1.1(c). The region beyond the regular hexagonal lattice is also subdivided in finer regions as shown in Fig. 1.1(c). The external boundary of lattice cell is divided into a set of finite surfaces. The zone to zone coupling in the lattice cell is achieved using region to region CPs. The coupling between the cells in the same FA and cells of different FAs is achieved by expanding the angular flux leaving or entering a lattice cell into a finite set of linearly independent functions. The angular flux in the half space created by each surface of lattice cell has been expanded in a double P_2 (DP2) Legendre polynomial.

The theory of interface current method implemented in TRANPIN is described in detail in Chapter–2. In the TRANPIN code, the discretized flux and outgoing current equations are solved in a multigroup formalism. The code is designed to consider any group structure. TRANPIN can take the microscopic cross sections directly from the cross section libraries used traditionally for lattice calculations. Presently, the 172 group cross section libraries in WIMS format can be used in TRANPIN [31, 32].

TRANPIN is the whole core calculation code which does not require cross sections generated by a prior transport calculation of the FA i.e. no separate lattice calculation is required. However it was decided to first test the interface current method using DP2 expansion for single lattice FA calculation. The CP method is an accurate and versatile method which exists in most of the popular lattice analysis codes. The double P0/P1 (DP0/DP1) Legendre expansions of angular flux had been applied in two–dimensional fuel assembly cell calculation codes such as CASMO [33], PHOENIX [34], APOLLO [35] and DRAGON [36]. Sanchez [37] and Ouisloumen et al [38] have applied the CP method to hexagonal assemblies with DP1 expansion. The use of DP2 expansion for single lattice FA in hexagonal geometry is not reported in literature to the best of our knowledge. Since TRANPIN is expected to include a fuel depletion model for whole core calculation, so the burnup characteristics of the DP2 model for a single FA were needed to be studied before employing this model for performing whole core calculation. Therefore, the DP2 lattice model was incorporated the lattice analysis code VISWAM. The benchmarking and validation exercise of the burn up model is presented in Chapter–3.

In Chapter–4 the spatial discretisation of whole core using fine meshes, the numbering scheme of the meshes, connectivity of the meshes and iteration scheme adopted for the solution method is presented in detail.

Two heterogeneous whole core benchmark problems in 2D geometry were analyzed. The numerical results of benchmarking and validation exercise of TRANPIN are presented in detail in Chapter–5. Chapter–6 provides the summary and conclusion of the present thesis work. The broad observations and scope for future work is discussed in this chapter.

1.4 Summary

India is planning to increase its present nuclear installation capacity to 63GW by 2032. This will be achieved by a mix of indigenously developed and imported nuclear power plants. The physics modeling of these reactors is a very challenging task due to their complex design. To cater to the challenging physics design requirements of the operating, future and indigenous reactor developments, there is a need to develop indigenous state of the art computational capability. Currently the two step core computational methodology is adopted in India. This methodology has its limitations due to assembly homogenization errors. It is planned to develop a state of the art 3D pin–by–pin calculation tool. As a first step to achieve this goal, a whole core transport theory code TRANPIN in 2D hexagonal geometry has been developed. The code performs the full core calculation, without homogenizing the various lattice cells present in the FAs, in multi group formalism. The TRANPIN employs interface current method based on 2D CP. Application of the 2D CP method with DP2 approximation of the angular flux to hexagonal assembly / core geometry is a novel feature of TRANPIN code.

CHAPTER – 2

FORMALISM OF INTERFACE CURRENT METHOD

The interface current method is a form of nodal methods used to study and solve the integral form of transport equation. The idea of a nodal method is to divide the solution domain into regions (or nodes) and to use an approximation to describe the transfer between nodes [39]. The solutions for adjacent nodes are linked by using approximate expansions for the angular fluxes entering and leaving the nodes. In a nodal method, only the unknown fluxes local to a node are directly connected to one another. This results in a set of dense matrices, one for each node, that are connected by means of their interface values. Consequently, such a method can be subjected to a node–by–node iterative solution in which the known incoming angular fluxes and the internal sources are used to calculate the outgoing angular fluxes.

Interface currents are used to link the solutions in cells of optically large solution domain such as whole core. This is especially helpful for treatment of multidimensional whole core geometries where a direct application of the CP method would require accurate multidimensional numerical quadrature over large regions [39]. Also, the interface current method reduces the coupling of the spatial variables, thus permitting an iterative cell–by–cell solution. This results in a reduction of the computing time necessary for the calculation of the collision probability matrix and for the solution of the system of equations for the fluxes. The interface current method based on 2D collision probability (CP) has been implemented in the lattice analysis code VISWAM and a new pin–by–pin whole core code TRANPIN has been developed employing this method.

This chapter describes the theory and formalism of interface current method implemented in VISWAM and TRANPIN code systems. First the integral form of transport equation is derived in Section 2.1. In Section 2.2, this integral form of transport equation is integrated over

the solution domain to derive the discretized form of transport equation. The discretized equation has four collision probability matrices. The properties of these matrices and their formulae are derived in 2D geometry in Sections 2.3 and 2.4. Section 2.5 gives the numerical integration scheme for computing the collision probability integrals. The normalization scheme of these matrices and solution scheme to evaluate scalar flux are described in Sections 2.6 and 2.7 respectively.

2.1 The Integral Form of Transport Equation

The integro-differential form of neutron transport equation is [40, 41, 42, 43]

$$\overrightarrow{\Omega}.\,\vec{\nabla}\phi\left(\vec{r},\overrightarrow{\Omega},E\right)+\ \Sigma(\vec{r},E)\phi\left(\vec{r},\overrightarrow{\Omega},E\right)=\ q\left(\vec{r},\overrightarrow{\Omega},E\right) \tag{2.1}$$

The neutron transport equation in (2.1) essentially gives the exact equation for angular neutron flux by simply balancing the various mechanisms by which neutrons can be gained or lost from an arbitrary volume *V* within the system. The two terms on left give the removal of neutrons due to streaming and neutron loss due to collisions. Here $\Sigma(\vec{r},E)$ is the total neutron cross section. The term on right describes the total neutron production in *V*. The source $q\left(\vec{r},\overrightarrow{\Omega},E\right)$ is given by

$$q\left(\vec{r},\overrightarrow{\Omega},E\right)=\ \int dE'\int d\Omega'\,\Sigma_s\left(\vec{r},\overrightarrow{\Omega'}\rightarrow\overrightarrow{\Omega},E'\rightarrow E\right)\phi\left(\vec{r},\overrightarrow{\Omega'},E'\right)+\ \mathcal{S}(\vec{r},\overrightarrow{\Omega}) \tag{2.2}$$

Here $\mathcal{S}\left(\vec{r},\overrightarrow{\Omega}\right)$ includes fission source and any external source present. In order to simplify the discussion, one group formulation is considered which omits the energy dependence. Here the streaming operator $(\overrightarrow{\Omega}.\,\vec{\nabla})$ is just directional derivative along the direction of neutron travel. If *s* is the distance travelled by neutron along direction $\overrightarrow{\Omega}$, the streaming operator can be written as directional derivative

$$\overrightarrow{\Omega}.\,\vec{\nabla}=\ \frac{d}{ds}$$

If Eq. (2.1) is written at $\vec{r} + s\,\vec{\Omega}$ then

$$\frac{d}{ds}\phi\left(\vec{r} + s\,\vec{\Omega},\vec{\Omega}\right) + \Sigma\left(\vec{r} + s\,\vec{\Omega}\right)\phi\left(\vec{r} + s\,\vec{\Omega},\vec{\Omega}\right) = q\left(\vec{r} + s\,\vec{\Omega},\vec{\Omega}\right) \tag{2.3}$$

To derive the integral transport equation, one has to look back along the line from where neutrons are coming. Therefore defining $R = -s$, from which $d/ds = -d/dR$ and equation (2.3) becomes

$$-\frac{d}{dR}\phi\left(\vec{r} - R\,\vec{\Omega},\vec{\Omega}\right) + \Sigma\left(\vec{r} - R\,\vec{\Omega}\right)\phi\left(\vec{r} - R\,\vec{\Omega},\vec{\Omega}\right) = q\left(\vec{r} - R\,\vec{\Omega},\vec{\Omega}\right) \tag{2.4}$$

The derivative in R is removed by using the integrating factor

$$exp\left[-\int_0^R \Sigma\left(\vec{r} - R'\,\vec{\Omega}\right)dR'\right] \tag{2.5}$$

which has the property

$$\frac{d}{dR}exp\left[-\int_0^R \Sigma\left(\vec{r} - R'\,\vec{\Omega}\right)dR'\right] = -\Sigma\left(\vec{r} - R\,\vec{\Omega}\right)exp\left[-\int_0^R \Sigma\left(\vec{r} - R'\,\vec{\Omega}\right)dR'\right] \tag{2.6}$$

Hence multiplying Eq. (2.4) by the itegrating factor and using the property in (2.6)

$$-\frac{d}{dR}\phi\left(\vec{r} - R\,\vec{\Omega},\vec{\Omega}\right)exp\left[-\int_0^R \Sigma\left(\vec{r} - R'\vec{\Omega}\right)dR'\right] =$$

$$q\left(\vec{r} - R\,\vec{\Omega},\vec{\Omega}\right)exp\left[-\int_0^R \Sigma\left(\vec{r} - R'\,\vec{\Omega}\right)dR'\right] \tag{2.7}$$

Integrating this equation along the neutron path from 0 to R gives

$$\phi\left(\vec{r},\vec{\Omega}\right) = \int_0^R dR'\,q\left(\vec{r} - R\vec{\Omega},\vec{\Omega}\right)exp\left[-\int_0^{R'} \Sigma\left(\vec{r} - R''\,\vec{\Omega}\right)dR''\right]$$

$$+\,\phi\left(\vec{r} - R\,\vec{\Omega},\vec{\Omega}\right)exp\left[-\int_0^R \Sigma\left(\vec{r} - R''\,\vec{\Omega}\right)dR''\right] \tag{2.8}$$

The expressions in the exponentials are line integrals of the total cross section along the line of neutron travel. From the analogy to the transmission of light, the optical path between $\vec{r}$ and $\vec{r} - R'\vec{\Omega}$ is referred as

$$\tau(\vec{r}, \vec{r} - R'\vec{\Omega}) = \int_0^{R'} \Sigma(\vec{r} - R''\,\vec{\Omega})\, dR'' \tag{2.9}$$

Using this definition of optical path, Eq. (2.8) takes the following form

$$\phi(\vec{r}, \vec{\Omega}) = \phi(\vec{r} - R\,\vec{\Omega}, \vec{\Omega}) exp[-\tau(\vec{r}, \vec{r} - R\,\vec{\Omega})] + \int_0^R dR'\, q(\vec{r} - R'\,\vec{\Omega}, \vec{\Omega}) exp[-\tau(\vec{r}, \vec{r} - R'\vec{\Omega})] \tag{2.10}$$

Equation (2.10) is the required form of integral transport equation. If the nature of source defined in Eq. (2.2) is isotropic in the laboratory system or assumed to be isotropic by utilizing the transport approximation to the scattering cross section, the angular dependence of q in above equation can also be omitted and the equation (2.10) takes the following form

$$\phi(\vec{r}, \vec{\Omega}) = \phi(\vec{r} - R\,\vec{\Omega}, \vec{\Omega}) exp[-\tau(\vec{r}, \vec{r} - R\,\vec{\Omega})] + \frac{1}{4\pi} \int_0^R dR'\, q(\vec{r} - R'\,\vec{\Omega}) exp[-\tau(\vec{r}, \vec{r} - R'\vec{\Omega})] \tag{2.11}$$

If the medium is bound by a surface S, Eq. (2.11) can be written in terms of the known incoming neutrons by taking R as the distance from $\vec{r}$ back along the flight path in the direction $\vec{\Omega}$ to the point, $\vec{r} - R\,\vec{\Omega}$, where the neutrons enter the problem domain. Therefore Eq. (2.11) can be written as

$$\phi(\vec{r}, \vec{\Omega}) = \phi(\vec{r_S}, \vec{\Omega}) e^{-\tau_S} + \frac{1}{4\pi} \int_0^{R_S} dR'\, q\left(\vec{r'}\right) e^{-\tau(R')} \tag{2.12}$$

where $\vec{r_S} = \vec{r} - R_S\,\vec{\Omega}$ is an arbitrary point on the line passing through $\vec{r}$ in the direction $\vec{\Omega}$ on the surface S and $\vec{r'} = \vec{r} - R'\vec{\Omega}$.

The equation for scalar flux is obtained by integrating equation (2.12) over all angles. Thus

$$\phi(\vec{r}) = \int \phi\left(\vec{r}, \overrightarrow{\Omega}\right)\, d\overrightarrow{\Omega} = \int_S \phi\left(\overrightarrow{r_S}, \overrightarrow{\Omega}\right) e^{-\tau_S}\, d\overrightarrow{\Omega} + \frac{1}{4\pi}\int_S \int_0^{R_S} q\left(\overrightarrow{r'}\right) e^{-\tau(R')}\, dR'\, d\overrightarrow{\Omega} \quad (2.13)$$

Now

$$d\overrightarrow{\Omega} = \frac{(\overrightarrow{\Omega}.\hat{n})dS}{R_S^2} \text{ and } d\overrightarrow{r} = R^2 dR\, d\overrightarrow{\Omega} \quad (2.14)$$

Using these, above equation can be rewritten as

$$\phi(\vec{r}) = \int_S \frac{e^{-\tau_S}}{R_S^2}\left(\overrightarrow{\Omega}.\ \hat{n}_-\right) \phi_-\left(\overrightarrow{r_S}, \overrightarrow{\Omega}\right) dS + \int_V \frac{e^{-\tau(R)}}{4\pi R^2} q\left(\overrightarrow{r'}\right) d\overrightarrow{r'} \quad (2.15)$$

where $\phi_-\left(\overrightarrow{r_S}, \overrightarrow{\Omega}\right)$is the incoming angular flux at surface *S*.

The outgoing flux at surface S can be obtained from Eq. (2.12) as it is valid at any point. The outgoing flux is given by

$$\phi_+\left(\overrightarrow{r'_S}, \overrightarrow{\Omega}\right) = \phi_-\left(\overrightarrow{r_S}, \overrightarrow{\Omega}\right) e^{-\tau_S} + \frac{1}{4\pi}\int_0^{R_S} dR'\, q\left(\overrightarrow{r'}\right) e^{-\tau(R')} \quad (2.16)$$

A boundary condition is required in order to close the system of Eqs. (2.15) and (2.16). The boundary condition can be written in terms of a relation between the outgoing and incoming angular flux on the surface *S* as [40]

$$\phi_-\left(\overrightarrow{r_S}, \vec{\Omega}\right)) = \int t\left(\overrightarrow{r_S}, \overrightarrow{\Omega'} \rightarrow \vec{\Omega}\right) \phi_+\left(\overrightarrow{r_S}, \overrightarrow{\Omega'}\right)\, d\overrightarrow{\Omega'}. \quad (2.17)$$

where *t* describes the transmission or albedo factors at the surface *S*.

2.2 Discretized Flux Equation

The system of Eqs. (2.15) and (2.16) gives an exact description of the flux distribution inside the region under consideration as well as the outgoing angular flux through the surface enclosing the region for a given incoming angular flux. In order to solve these equations, some numerical approximations are required for the scalar fluxes inside the cells and for the angular fluxes leaving and entering the cell surfaces. In the present research work, the flat flux

approximation is considered inside the region, i.e. scalar flux $\phi(\vec{r})$ is constant in each region of the solution domain. Also the cross sections and the source inside each region are assumed constant. If solution domain is divided into N_V regions of volume V_i then [41]

$$\Sigma(\vec{r}) = \Sigma_i \text{ for } r \in V_i ,$$

$$q(\vec{r}) = q_i \text{ for } r \in V_i .$$

Here, the external boundary S is considered to be composed of N_S surfaces of area S_α. The angular flux on these surfaces is approximated by a series expansion in terms of half–range spherical harmonics

$$\phi_{\pm}(\overrightarrow{r_S}, \overrightarrow{\Omega}) \sim \frac{1}{\pi}\sum_{\nu=0}^{N_\nu} J_{\pm}^{\nu}(\overrightarrow{r_S})\psi^{\nu}(\overrightarrow{\Omega}, \overrightarrow{n_{\pm}}). \tag{2.18}$$

where N_ν is the number of terms retained in the expansion, $J_{\pm}^{\nu}$ are the expansion coefficients and ψ^{ν} are the linearly independent functions which are taken as orthonormal and satisfy the following orthonormality condition

$$\int(\overrightarrow{\Omega}, \overrightarrow{n_{\pm}})\psi^{\nu}(\overrightarrow{\Omega}, \overrightarrow{n_{\pm}})\psi^{\nu}(\overrightarrow{\Omega}, \overrightarrow{n_{\pm}})d\overrightarrow{\Omega} = \pi\delta_{\mu\nu} \tag{2.19}$$

The spatially averaged fluxes and partial currents are defined as

$$\phi_j = \frac{1}{V_j}\int_{V_j} \phi(\vec{r})\, d\vec{r} \tag{2.20a}$$

$$J_{\alpha}^{+} = \frac{1}{S_\alpha}\int_{S_\alpha} J(\vec{r})\, dS \tag{2.20b}$$

Now Eq. (2.15) can be integrated over each region i of the solution domain. Therefore integrating Eq. (2.15) over volume V_j of j[th] zone and multiplying the result by Σ_j

$$\Sigma_j \int_{V_j} \phi(\vec{r})\, d\vec{r} = \Sigma_j \sum_{\alpha=1}^{N_S} \int_{V_j}\int_{S} \frac{e^{-\tau_S}}{R_S^2}(\overrightarrow{\Omega}.\ \hat{n}_-)\, \phi_-(\overrightarrow{r_S}, \overrightarrow{\Omega}) dS\, d\vec{r}$$

$$+ \Sigma_j \sum_{i=1}^{N_V} \int_{V_j}\int_{V_i} \frac{e^{-\tau(R)}}{4\pi R^2} q\left(\overrightarrow{r'}\right) d\overrightarrow{r'}\, d\vec{r} \tag{2.21}$$

Now using Eq. (2.20) in Eq. (2.21) and defining

$$P_{ji} = \frac{\Sigma_j}{V_i}\int_{V_j}\int_{V_i}\frac{e^{-\tau(R)}}{4\pi R^2}d\overrightarrow{r'}\,d\vec{r}\,. \tag{2.22a}$$

$$P^{\nu}_{j\alpha} = \frac{\Sigma_j}{S_\alpha}\int_{V_j}\int_{S_\alpha}\frac{e^{-\tau_S}}{4\pi R_S^2}\psi^{\nu}(\overrightarrow{\Omega},\overrightarrow{n_-})\left(\overrightarrow{\Omega}.\hat{n}_-\right)dS\,d\vec{r}\,. \tag{2.22b}$$

Eq. (2.21) becomes

$$\Sigma_j V_j \phi_j = \sum_{\alpha=1}^{N_S}\sum_{\nu=0}^{N_\nu} P^{\nu}_{j\alpha} S_\alpha J^{\nu}_{-,\alpha} + \sum_{i=1}^{N_V} P_{ji}\, q_i. \tag{2.23}$$

Here $q_i = S_i V_i + \Sigma_{si} V_i \phi_i$ is the total source in region *i*, S_i is the fission and scattering source in a group and Σ_{si} is the self scattering cross section within the group. Here P_{ji} is called the region to region collision probability and is defined as the probability of a neutron emitted uniformly and isotropically in region *i* and having its first collision in region *j*. $P^{\nu}_{j\alpha}$ is called surface to region collision probability and is defined as the probability of neutron entering through surface α in mode *v* and having first collision in region *j*.

The expression for outgoing current through each discretized surface is obtained using Eq. (2.16). For current through surface α, multiplying Eq. (2.16) with $\overrightarrow{\Omega}.\,\hat{n}_+ d\vec{\Omega}$ and integrating over surface

$$\begin{aligned}
&\int_{S_\alpha}\phi_+\left(\overrightarrow{r'_S},\overrightarrow{\Omega}\right)\overrightarrow{\Omega}.\,\hat{n}_+\,d\vec{\Omega}dS \\
&\qquad = \sum_{\beta=1}^{N_S}\int_S e^{-\tau_S}\,\phi_-\left(\overrightarrow{r_S},\overrightarrow{\Omega}\right)\overrightarrow{\Omega}.\,\hat{n}_+ d\vec{\Omega}dS \\
&\qquad + \sum_{i=1}^{N_V}\int\frac{1}{4\pi}\int_0^{R_S} dR'\,q\left(\overrightarrow{r'}\right)e^{-\tau(R')}\,\overrightarrow{\Omega}.\,\hat{n}_+ d\vec{\Omega}d\vec{r}\,dS
\end{aligned} \tag{2.24}$$

Now using Eq. (2.20) and

$$R_S^2 d\vec{\Omega} = \overrightarrow{\Omega}.\,\hat{n}\_ dS$$

$$R^2 d\vec{\Omega} dR = d\vec{r}$$

and defining

$$P_{\alpha i}^{\nu} = \frac{1}{V_i}\int_{S_\alpha}\int_{V_i}\frac{e^{-\tau_S}}{4\pi R^2}\psi^{\nu}(\overrightarrow{\Omega},\overrightarrow{n_+})\,\overrightarrow{\Omega}.\hat{n}_+\,d\vec{r}dS\,. \tag{2.25a}$$

$$P_{\alpha\beta}^{\nu\mu} = \int\int\frac{e^{-\tau_{SS'}}}{4\pi R_S^2}\psi^{\nu}\left(\overrightarrow{\Omega},\overrightarrow{n_+}\right)\psi^{\mu}\left(\overrightarrow{\Omega},\overrightarrow{n_-}\right)\overrightarrow{\Omega}.\hat{n}_+\;\overrightarrow{\Omega}.\hat{n}_-\;dS'dS\,. \tag{2.25b}$$

Eq. (2.24) becomes

$$S_\alpha J_{+,\alpha}^{\nu} = \sum_{\beta=1}^{N_S}\sum_{\mu=0}^{N_\mu} P_{\alpha\beta}^{\nu\mu}\,J_{-,\beta}^{\mu}S_\beta + \sum_{i=1}^{N_V} P_{\alpha i}^{\nu}\,q_i\,. \tag{2.26}$$

Here $P_{\alpha i}^{\nu}$, called escape probability, is defined as the probability that neutrons emitted uniformly and isotropically in region *i* will escape through surface α in mode *ν*. $P_{\alpha\beta}^{\nu\mu}$ is called the surface to surface transmission probability and defined as the probability of neutrons entering through surface β in mode μ to be transmitted through the cell and out through surface α in mode *ν* without making a collision. It should be noted that all the probability matrices in Eqs. (2.22) & (2.25) have a physical meaning of probabilities only for $\mu, \nu = 0$. For higher values of μ & ν, they are components of probabilities and are traditionally called probabilities [44].

Eqs. (2.23) & (2.26) are the required discretized equations for a cell under consideration. The physical interpretation of Eq. (2.23) is that the two terms on the right are the contributions to the collision rate in a region of cell from the neutrons entering through all the surfaces of the cell and sources within all the regions respectively. Similarly, in Eq. (2.26), the two terms on right give the contribution to the outward current through a surface of cell from the inward currents from all other surfaces of the cell plus the sources within all regions of the cell [44]. The boundary condition given in Eq. (2.17) closes this system of equations. Here, the albedo boundary condition of the following form [40, 41] has been used

$$\phi_{-}\left(\vec{r_S}, \vec{\Omega} - 2(\vec{n_S} . \vec{\Omega})\right) = \beta\left(\vec{r_S}, \vec{\Omega}\right)\phi_{+}\left(\vec{r_S}, \vec{\Omega}\right) \tag{2.27}$$

where $\beta\left(\vec{r_S}, \vec{\Omega}\right)$ is the reflection coefficient at the surface S and $\vec{\Omega} - 2(\vec{n_S} . \vec{\Omega})$ is the final direction in which neutron travels after reflection as shown in Fig. 2.1.

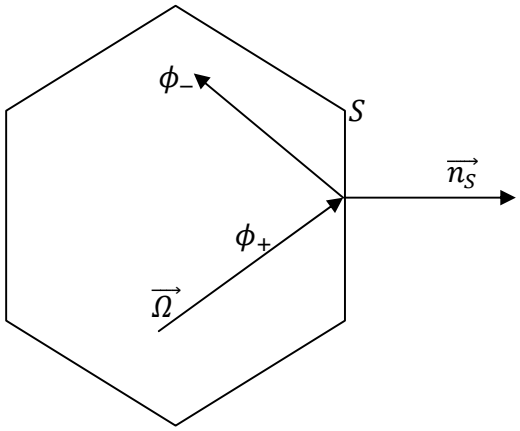

Fig. 2.1 – Specular Reflection of neutron at the surface

Under the approximations described above, Eq. (2.27) takes the following discretized form

$$J^{\nu}_{-,\alpha} = \sum_{\beta=1}^{N_S} \sum_{\mu=0}^{N_\mu} A^{\nu\mu}_{\alpha\beta} J^{\mu}_{+,\beta}. \tag{2.28}$$

where $A^{\nu\mu}_{\alpha\beta}$ is the boundary condition matrix which gives a relation between the outgoing current on a given surface and the incoming current on different surfaces. Typically for purely reflective boundary conditions this matrix will be equivalent to the product of two Kronecker delta functions $\delta_{\alpha,\beta}$ and $\delta_{\mu,\nu}$.

2.3 Properties of the Collision Probability Matrices

The four types of collision probabilities defined in Eqs. (2.22) and (2.25) satisfy some reciprocity and conservation relations. The reciprocity relations arise due to the symmetry of the optical distance i.e. $\tau\left(\vec{r}, \vec{r'}\right) = \tau\left(\vec{r'}, \vec{r}\right)$. The collision probabilities satisfy the following reciprocity relations

$$\Sigma_j V_j P_{ij} = \Sigma_i V_i P_{ji}. \tag{2.29a}$$

$$P_{i\alpha}^{\nu} = \frac{4\Sigma_i V_i}{S_\alpha} P_{\alpha i}^{\nu}. \tag{2.29b}$$

$$S_\alpha P_{\beta\alpha}^{\nu\mu} = S_\beta P_{\alpha\beta}^{\mu\nu}. \tag{2.29c}$$

where it is assumed that the angular representation functions satisfy [40]

$$\psi_{+,\alpha}^{\nu}(\overrightarrow{\Omega}) = \psi_{-,\alpha}^{\nu}(-\overrightarrow{\Omega}) \tag{2.30}$$

The following classical conservation relations satisfied by collision probability matrices can be derived using integro-differential transport equation:

$$\sum_{j=1}^{N_V} P_{ji} + \sum_{\alpha=1}^{N_S} P_{\alpha i}^{0} = 1. \tag{2.31a}$$

$$\sum_{j=1}^{N_V} P_{j\alpha}^{\nu} + \sum_{\beta=1}^{N_S} P_{\beta\alpha}^{\nu 0} = \delta_{0\nu}. \tag{2.31b}$$

The physical interpretation of Eq. (2.31a) is that a neutron born in region *i* must either collide in the other regions or escape from it. Similarly, Eq. (2.31b) represents that a neutron entering through a surface should either collide in one of the zones or escape through one of the surfaces. These reciprocity and conservation relations should be utilized to reduce the number of collision probability calculations and guarantee the neutron conservation.

2.4 Calculation of Collision Probabilities

Eqs. (2.22) and (2.25) give the general form for the four types of collision probability matrices in 3D geometry. Here, the description pertains to the application in 2D hexagonal geometry. Here the term '2D geometry' is referred to the geometry which is infinite in z direction but finite in the plane perpendicular to it. The general two dimensional space element used for calculating collision probabilities is shown in Fig. 2.2. Out of the four collision probability matrices, the surface to region probabilities are normally not computed by direct numerical integration to save computational efforts. Reciprocity relation in Eq. (2.29b) is utilized

to directly calculate these probabilities from escape probability. So here only the description of remaining three collision probability matrices is discussed. For calculating the different components of collision probabilities, the angular flux in each of the half space created by every bounding surface is expanded into P_2 Legendre polynomials. The following properly orthonormalized angular representation functions for DP2 expansion of angular flux are used [9, 41]

$$\psi^{0}_{\pm,\alpha} = 1. \tag{2.32a}$$

$$\psi^{1}_{\pm,\alpha} = 2\sin\vartheta\sin\omega. \tag{2.32b}$$

$$\psi^{2}_{\pm,\alpha} = 3\sqrt{2}(\sin\vartheta\cos\omega - \tfrac{2}{3}). \tag{2.32c}$$

$$\psi^{3}_{\pm,\alpha} = \tfrac{20}{\sqrt{17}}(\sin^2\vartheta - \tfrac{3}{5}\sin\vartheta\cos\omega - \tfrac{7}{20}). \tag{2.32d}$$

$$\psi^{4}_{\pm,\alpha} = \sqrt{306}(\sin^2\vartheta\cos^2\omega - \tfrac{2}{51}\sin^2\vartheta - \tfrac{20}{17}\sin\vartheta\cos\omega + \tfrac{16}{51}). \tag{2.32e}$$

$$\psi^{5}_{\pm,\alpha} = \tfrac{30}{\sqrt{11}}(\sin^2\vartheta\cos\omega\sin\omega - \tfrac{8}{15}\sin\vartheta\sin\omega). \tag{2.32f}$$

Here ϑ is the angle between neutron tracking direction and polar axis, and ω is the angle which projection of the neutron direction on 2D plane makes with the outward (+) or inward (-) normal to surface α as shown in Fig. 2.3. Here first function (Eq. 2.32a) corresponds to the P0 expansion, the first three functions (Eq. 2.32a to 2.32c) correspond to the P1 expansion and all six functions (Eq. 2.32) constitute the P2 expansion.

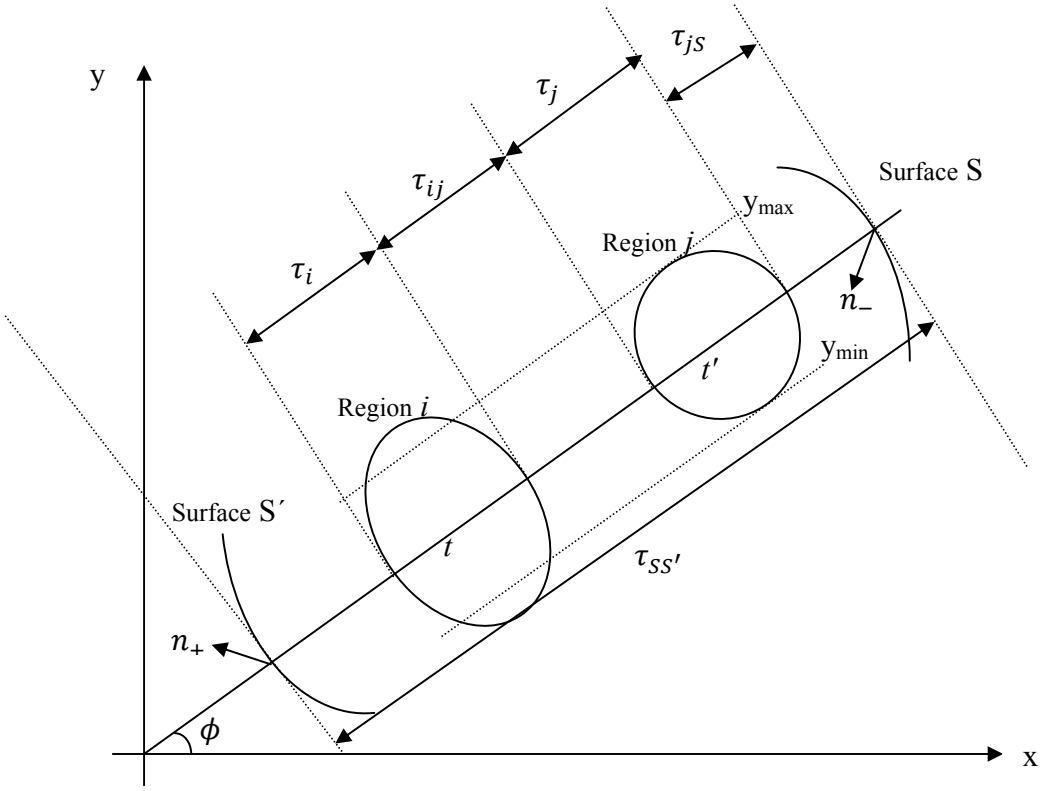

Fig. 2.2 – Definition of 2D Space element

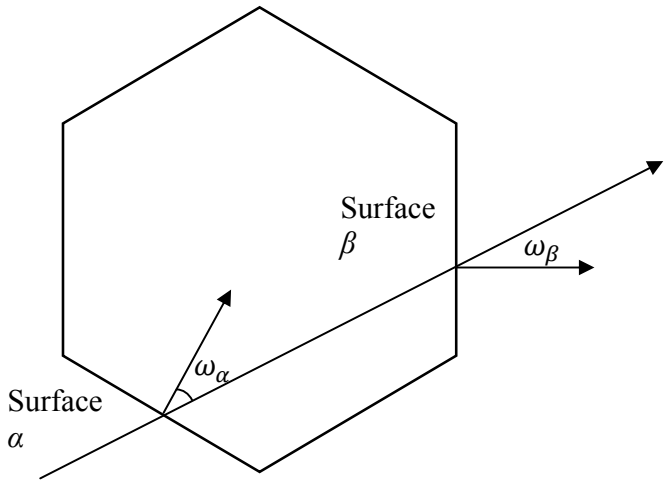

Fig. 2.3 – Angle of projection of neutron direction on 2D plane with inward/outward normal to lattice cell surfaces

Here, first general 3D volume and surface integrals are simplified in 2D geometry. For this purpose, spherical coordinate system is used. The volume element $d\vec{r}$ and surface element dS in spherical coordinate system is written as

$$d\vec{r} = R^2 dR \sin\vartheta \, d\vartheta d\phi. \tag{2.33a}$$

$$R_S^2 \sin\vartheta \, d\vartheta d\phi = \vec{\Omega}.\, \hat{n}\_dS. \tag{2.33b}$$

Using this the volume and surface integrals for a function $f(\vec{r})$ are simplified as [41]

$$\int \frac{f(\vec{r})}{R^2} d\vec{r} = \int_0^{2\pi} d\phi \int_{-\frac{\pi}{2}}^{\frac{\pi}{2}} \sin\vartheta \, d\vartheta \int f(\phi, \vartheta, R) dR. \tag{2.34}$$

$$\int \frac{f(\vec{r})}{R^2} \vec{\Omega}.\, \hat{n}\_dS = \int_0^{2\pi} d\phi \int_{-\frac{\pi}{2}}^{\frac{\pi}{2}} \sin\vartheta \, d\vartheta f(\phi, \vartheta, R_S). \tag{2.35}$$

Using the notation, $t = R\sin\vartheta$ (see Fig 2.2) and if $f(\phi, \vartheta, R) = f(\phi, \pi - \vartheta, R)$ is symmetric in polar angle, Eqs. (2.34) and (2.35) become

$$\int \frac{f(\vec{r})}{R^2} d\vec{r} = 2\int_0^{2\pi} d\phi \int_0^{\frac{\pi}{2}} d\vartheta \int f(\phi, \vartheta, t) dt. \tag{2.36}$$

$$\int \frac{f(\vec{r})}{R^2} \vec{\Omega}.\, \hat{n}\_dS = 2\int_0^{2\pi} d\phi \int_0^{\frac{\pi}{2}} \sin\vartheta \, d\vartheta \int f(\phi, \vartheta, t_S) dt. \tag{2.37}$$

2.4.1 Region to Region Collision Probabilities

Using the result in Eq. (2.36), Eq. (2.22a) reduces to

$$P_{ji} = \frac{\Sigma_j}{2\pi V_i} \int_0^{2\pi} d\phi \int_0^{\frac{\pi}{2}} d\vartheta \int_{y\in j} dy \int dt' \int dt \, e^{-\tau(R)}. \tag{2.38}$$

The optical distance $\tau(R)$ in Fig. (2.2) can be written as

$$\tau(R) = \begin{cases} \frac{\Sigma_i(t_i - t') + \sum_{k=i+1}^{j-1} \Sigma_k t_k + \Sigma_j t}{\sin\vartheta} & for\ i > j \\ \frac{\Sigma_i(t_i - t')}{\sin\vartheta} & for\ i = j \end{cases} \tag{2.39}$$

Using this definition of $\tau(R)$ in Eq. (2.38), the equation becomes

$$P_{ji} = \frac{\Sigma_j}{2\pi V_i} \int_0^{2\pi} d\phi \int_0^{\frac{\pi}{2}} d\vartheta \int_{y\in j} dy \int_0^{t_i} dt' \int_0^{t_j} dt \, e^{-\frac{\Sigma_i(t_i - t') + \sum_{k=i+1}^{j-1} \Sigma_k t_k + \Sigma_j t}{\sin\vartheta}}.$$

On solving the integration over t and t' and doing some algebra the following expression is obtained

$$P_{ji} = \frac{1}{2\pi\Sigma_i V_i}\int_0^{2\pi} d\phi \int_{y_{min}}^{y_{max}} \left[Ki_3(\tau_{ij}) - Ki_3(\tau_{ij}+\tau_i) - Ki_3(\tau_{ij}+\tau_j) + Ki_3(\tau_{ij}+\tau_i+\tau_j)\right] dy\,. \tag{2.40}$$

where the analytical integration over polar angle ϑ is absorbed in the Bickley-Naylor function of third order Ki_3. The general Bickley-Naylor function of order 'n' is defined as

$$Ki_n(\tau) = \int_0^{\pi/2} d\vartheta\, sin^{n-1}\vartheta\, e^{-\frac{\tau}{\sin\vartheta}} \tag{2.41}$$

When $i = j$, the integral over t in Eq. (2.36) must be divided into two different parts since the expression for τ with $t \leq t'$ is different from the one when $t > t'$ [41]. Therefore

$$P_{ii} = \frac{\Sigma_i}{2\pi V_i}\int_0^{2\pi} d\phi \int_0^{\frac{\pi}{2}} d\vartheta \int_{y\in i} dy \int_0^{t_i} dt' \left[\int_0^{t'} e^{-\frac{\Sigma_i(t'-t)}{\sin\vartheta}} dt + \int_{t'}^{t_i} e^{-\frac{\Sigma_i(t-t')}{\sin\vartheta}} dt\right].$$

Solving the integration, the following expression for self collision probability P_{ii} is obtained

$$P_{ii} = 1 - \frac{1}{2\pi\Sigma_i V_i}\int_0^{2\pi} d\phi \int_{y_{min}}^{y_{max}} [Ki_3(0) - Ki_3(\tau_i)]\, dy\,. \tag{2.42}$$

Eqs. (2.40) and (2.42) are the required expressions for the region to region collision probabilities. Since the sources and scattering are assumed to be isotropic, the region to region collision probabilities have no angular dependence. Here it is to be noted that the limits of y integration in Eqs. (2.40) and (2.42) depend on the azimuthal angle ϕ. It is limited to the minimum and maximum values of y at that angle as shown in Fig 2.2. Since all the chords do not pass for all the y values through the regions i/j, only part of the y interval contribute to P_{ji} or P_{ii}.

2.4.2 Region to Surface Escape Probability

Using the expression for volume element in Eq. (2.33) and the result in Eq. (2.37), the escape probability for a neutron born isotropically in region *i* through surface α in mode ν in Eq. (2.25a) reduces to the following form in 2D geometry

$$P_{\alpha i}^{\nu} = \frac{1}{2\pi V_i}\int_0^{2\pi} d\phi \int_0^{\frac{\pi}{2}} d\vartheta \int dy \int dR \sin\vartheta\, \psi^{\nu}\left(\overrightarrow{\Omega}, \overrightarrow{n_+}\right) e^{-\tau_S(R)} . \tag{2.43}$$

Now using $t = R\sin\vartheta$, above Eq. reduces to

$$P_{\alpha i}^{\nu} = \frac{1}{2\pi V_i}\int_0^{2\pi} d\phi \int_0^{\frac{\pi}{2}} d\vartheta \int dy \int_0^{t_i} dt\, \psi^{\nu}(\overrightarrow{\Omega}, \overrightarrow{n_+})\, e^{-\tau_S(t)/\sin\vartheta}. \tag{2.44}$$

The optical distance $\tau_S(t)$ from region *i* is written as

$$\tau_S(t) = \frac{\Sigma_i(t_i - t) + \sum_{k=i+1}\Sigma_k t_k}{\sin\vartheta} \tag{2.45}$$

Using this definition of optical distance in Eq. (2.44) and performing the integration over t

$$P_{\alpha i}^{\nu} = \frac{1}{2\pi\Sigma_i V_i}\int_0^{2\pi} d\phi \int_0^{\frac{\pi}{2}} d\vartheta \int_{y_{min}}^{y_{max}} dy\, \psi^{\nu}(\overrightarrow{\Omega}, \overrightarrow{n_+})\, sin^2\theta\, (e^{-\frac{\tau_S}{\sin\theta}} - e^{-\frac{(\tau_i+\tau_S)}{\sin\theta}}). \tag{2.46}$$

The different components of region to surface escape probability are obtained using expansion functions (2.32) in Eq. (2.46). Substituting these functions in Eq. (2.46) and using the definition of Bickley-Naylor function in Eq. (2.41), the following expressions for different components are obtained

$$P_{\alpha i}^{0} = \frac{1}{2\pi\Sigma_i V_i}\int_0^{2\pi} d\phi \int_{y_{min}}^{y_{max}} [Ki_3(\tau_{iS}) - Ki_3(\tau_i + \tau_{iS})] dy . \tag{2.47a}$$

$$P_{iS_\alpha}^{1} = \frac{2}{2\pi\Sigma_i V_i}\int_0^{2\pi} d\phi \int_{y_{min}}^{y_{max}} \sin\omega_\alpha\, [Ki_4(\tau_s) - Ki_4(\tau_i + \tau_s)]\, dy. \tag{2.47b}$$

$$P_{iS_\alpha}^{2} = -2\sqrt{2}\, P_{iS_\alpha}^{0} + \frac{3\sqrt{2}}{2\pi\Sigma_i V_i}\int_0^{2\pi} d\phi \int_{y_{min}}^{y_{max}} \cos\omega_\alpha\, [Ki_4(\tau_s) - Ki_4(\tau_i + \tau_s)]\, dy. \tag{2.47c}$$

$$P_{iS_\alpha}^{3} = \frac{1}{\sqrt{17}}\left[-15\, P_{iS_\alpha}^{0} - 2\sqrt{2}\, P_{iS_\alpha}^{2} + \frac{20}{2\pi\Sigma_i V_i}\int_0^{2\pi} d\phi \int_{y_{min}}^{y_{max}} [Ki_5(\tau_s) - Ki_5(\tau_i + \tau_s)] dy\right]. \tag{2.47d}$$

$$P_{iS_\alpha}^4 = \frac{\sqrt{306}}{51}\Big[-24\,P_{iS_\alpha}^0 - 10\sqrt{2}\,P_{iS_\alpha}^2 + \frac{1}{2\pi\Sigma_i V_i}\int_0^{2\pi} d\phi \int_{y_{min}}^{y_{max}} (51cos^2\omega_\alpha - 2)[Ki_5(\tau_s) - Ki_5(\tau_i + \tau_s)]dy\Big]. \quad (2.47e)$$

$$P_{iS_\alpha}^5 = \frac{1}{\sqrt{11}}\Big[-8\,P_{iS_\alpha}^1 + \frac{30}{2\pi\Sigma_i V_i}\int_0^{2\pi} d\phi \int_{y_{min}}^{y_{max}} \cos\omega_\alpha \sin\omega_\alpha [Ki_5(\tau_s) - Ki_5(\tau_i + \tau_s)]\,dy\Big]. \quad (2.47f)$$

Here not all the directions of ϕ and intervals of y contribute to the integration. The integration over ϕ is limited to those directions which pass through surface α and integration over y is limited to y values passing through the region i.

2.4.3 Surface to Surface Transmission Probability

Using the result of surface integral in Eq. (2.37), the expression for surface to surface collision probability in Eq. (2.25b) becomes

$$P_{\alpha\beta}^{\nu\mu} = \frac{2}{\pi\, S_\alpha}\int_0^{2\pi} d\phi \int_0^{\frac{\pi}{2}} d\vartheta \int dy \sin^2\vartheta\, \psi^\nu\big(\overrightarrow{\Omega}, \overrightarrow{n_+}\big)\, \psi^\mu\big(\overrightarrow{\Omega}, \overrightarrow{n_-}\big) e^{-\tau_S(R)}. \quad (2.48)$$

The optical path between the surfaces α and β is written as

$$\tau_S(R) = \frac{\sum_{k=1}^{N_V} \Sigma_k t_k}{\sin\vartheta} = \frac{\tau_{\alpha\beta}}{\sin\vartheta} \quad (2.49)$$

Substituting this in Eq. (2.48) gives

$$P_{\alpha\beta}^{\nu\mu} = \frac{2}{\pi\, S_\alpha}\int_0^{2\pi} d\phi \int_0^{\frac{\pi}{2}} d\vartheta \int_{y_{min}}^{y_{max}} dy \sin^2\vartheta\, \psi^\nu\big(\overrightarrow{\Omega}, \overrightarrow{n_+}\big)\, \psi^\mu\big(\overrightarrow{\Omega}, \overrightarrow{n_-}\big) e^{-\frac{\tau_{\alpha\beta}}{\sin\vartheta}}. \quad (2.50)$$

This gives the general expression for transmission probability from surface β to surface α. The different components of transmission probability are obtained by using the expansion functions in Eq. (2.32) for incoming and outgoing angular fluxes in above equation. These expressions are given in Appendix A for different combinations of μ and ν. It is to be noted that all the components of $P_{\alpha\beta}^{\nu\mu}$ given in Appendix A are not computed numerically. Reciprocity relation in Eq. (2.29c) is utilized to minimize the computational efforts. Here too, only those y and ϕ intervals contribute to integration which pass through both surfaces α and β.

2.5 Computation of Collision Probability Integrals

2.5.1 Evaluation of Bickley-Naylor function

As seen in above expressions for collision probabilities, the integration over polar angle is replaced by the Bickley-Naylor functions defined in Eq. (2.41). With the usage of angular flux expansion functions in Eq. (2.32), the Bickley-Naylor functions of the order of 3 to 7 need to be numerically evaluated. In the present research work, the method given in [41 and 45] has been adopted. This method uses the Rational Chebyshev Approximations to evaluate the Bickley-Naylor functions $Ki_n(x)$ for n=1 to 10. The Bickley-Naylor functions satisfy a recursive relation enabling a function of any order to be found if three Bickley-Naylor functions of consecutive order are known. These formulae known as forward and backward recursion formula are given by the following equations:

$$(n-1)\,Ki_n(x) = x\,[Ki_{n-3}(x) - Ki_{n-1}(x)] + (n-2)\,Ki_{n-2}(x) - forward \qquad (2.51a)$$

$$x\,Ki_n(x) = (n+2)\,Ki_{n+3}(x) + x\,Ki_{n+2}(x) - (n+1)Ki_{n+1}(x) - backward \qquad (2.51b)$$

To get the best accuracy [45], forward recursion formula is used for $0 \le x \le 6$ and backward recursion formula is used for $x > 6$. For $x > 6$, $Ki_8(x)$, $Ki_9(x)$ and $Ki_{10}(x)$ are calculated and used in backward recursion to derive $Ki_n(x)$ for n= 7, 6,...,1. For $0 \le x \le 6$, $Ki_1(x)$, $Ki_2(x)$ and $Ki_3(x)$ are calculated and used in forward recursion to derive $Ki_n(x)$ for n=4, 5,...,10.

2.5.2 Quadrature Set Used

The calculation of probabilities using Eqs. (2.40), (2.42), (2.47) and different components of Eq. (2.50) given in Appendix A involves the evaluation of double integrals over y and ϕ numerically. These integrations are approximated by using numerical quadrature for angle and space. The problem domain is considered under different angles of rotation. For each value of ϕ

in the quadrature, a set of parallel lines, called tracks, are drawn. In the present work, the equidistant ray tracking method has been used. The tracking method is described in detail in Appendix B. If w_y and w_A are the weights associated with y and ϕ respectively then

$$\int f(y,\theta)\, dy\, d\phi = \sum_p \sum_q w_{yp} w_{Aq} f(y_p, \phi_q). \tag{2.52}$$

For evaluating these probabilities, two types of quadrature *viz.* equiangular and Gauss-Legendre quadrature can be used for angular variable ϕ. If N angles are chosen between 0 and π, then weights for equiangular quadrature are given by

$$w_A = \frac{(b-a)}{N} = \frac{\pi}{N}. \tag{2.53}$$

And the angular points are given by

$$\theta_i = \left(i - \frac{1}{2}\right) w_A = \left(i - \frac{1}{2}\right) \frac{\pi}{N} \;;\; \forall\, i = 1, N. \tag{2.54}$$

The integration points and weights can also be obtained using the Gauss–Legendre quadrature. The integration points and weights in the Gauss–Legendre quadrature are selected in such a way that:

$$\int_{-1}^{1} f(x)\, dx = \sum_{i=1}^{N} w_i\, f(x_i). \tag{2.55a}$$

is exact when $f(x)$ is a polynomial of order (2N–1) or lower [46]. This can be ensured by selecting x_i for each order N as the zeros of the Legendre polynomials $P_N(x)$. Once the integration points have been computed, the associated weights can be obtained using:

$$w_i = \frac{2}{(1-x_i^2)[P_N'(x_i)]^2}. \tag{2.55b}$$

If the limits of integration are *a* & *b,* the following transformation can be used

$$\int_a^b f(x)\, dx = \sum_{i=1}^{N} w_i'\, f(x_i'). \tag{2.56a}$$

such that

$$w_i' = \frac{(b-a)}{2} w_i. \tag{2.56b}$$

$$x_i' = \frac{(b-a)}{2} x_i + \frac{(b+a)}{2}. \quad (2.56c)$$

For integration limits of 0 to π, Gauss–Legendre points and weights corresponding to N=2 to 20, and for 24, 28, 32, 64 and 96 can be used in VISWAM and TRANPIN code systems.

For *y* integral, trapezoidal quadrature set is used. If the limits of *y* integration are from *a* to *b* and if N_y parallel lines are drawn, the separation between two lines or weight is given by

$$w_y = dy = \frac{(b-a)}{N_y}. \quad (2.57)$$

Here it should be noted that the tracking needs to be done only for a=0 to b=π, since the contribution from π to 2π will be associated with the probability P_{ij} which is symmetric to P_{ji}.

2.6 Normalization of Collision Probabilities

The collision probabilities calculated should satisfy the reciprocity and conservation relations given in Eqs. (2.29) & (2.31). Since the collision probabilities are computed using numerical integrations , the conservation relations may not get satisfied due to discretizing error. The conservation relations can be enforced by several normalizing schemes [41]. A method proposed by Villarino *et al* [47] has been adopted in the present work. In this method, we define

$$P_{ij}^H = (w_i + w_j) P_{ij}. \quad (2.58a)$$

$$P_{\alpha\beta}^H = (w_\alpha + w_\beta) P_{\alpha\beta}. \quad (2.58b)$$

Where P_{ij}^H and $P_{\alpha\beta}^H$ are the corrected probabilities and P_{ij} and $P_{\alpha\beta}$ are the uncorrected ones. The conservation laws are ensured by requiring

$$\sum_a (w_a + w_b) P_{ab} = 1. \quad (2.59a)$$

$$\sum_a w_a P_{ab} + w_b \sum_a P_{ab} = 1. \quad (2.59b)$$

$$\Rightarrow \quad w_b = \frac{1 - \sum_{a, a \neq b} w_a P_{ab}}{P_{bb} + \sum_a P_{ab}}. \quad (2.59c)$$

where the indices *a* and *b* run over all regions and surfaces. The Eq. (2.59c) is iteratively solved. Initially all the *w's* are assigned a value of 0.5, which is the value they would have if there were no errors in the probabilities. The iteration process uses an under relaxation factor of 0.7 [47]. The solution for w_a^{k+1} is assumed converged if

$$\max\left(\frac{w_a^{k+1}-w_a^k}{w_a^{k+1}}\right) \leq \epsilon. \tag{2.60}$$

or after a preset number of iterations, currently 20. The value used for ϵ is 10^{-5}. The advantage of this method is that by using weight factors, probabilities which are zero remain zero e.g., the self transmission probabilities $P_{\alpha\alpha}$.

To enforce the conservation relation (2.31b) for higher components of probabilities, the diagonal normalization scheme has been used. In this scheme, the error is found using (2.31b) as

$$\varepsilon_\alpha^\nu = \delta_{0\nu} - \sum_{j=1}^{N_V} P_{j\alpha}^\nu - \sum_{\beta=1}^{N_S} P_{\beta\alpha}^{0\nu} \qquad \forall\, \nu > 0. \tag{2.61}$$

This error is adjusted in the diagonal elements of transmission probability *i.e.*

$$P_{\alpha\alpha}^\nu = P_{\alpha\alpha}^\nu + \varepsilon_\alpha^\nu. \tag{2.62}$$

2.7 Use of Boundary Condition and Solution of CP Equations

The multigroup transport equations to be solved in a cell containing N_V regions form a linear system. The solution method described in [43] has been adopted. In the two linear equations defined by Eqs. (2.23) & (2.26), the source q_i , written in terms of group source and self scattering source, is given by

$$q_i = \Sigma_i^s \phi_i V_i + S_i V_i. \tag{2.63}$$

The group source S_i is defined as

$$S_i = \left(\sum_{\substack{g'=1 \\ g' \neq g}}^{G} \Sigma_{si}^{g' \to g} \phi_i^{g'} + \frac{\chi_g}{k} \sum_{g'=1}^{G} \nu \Sigma_{fi}^{g'} \phi_i^{g'} \right). \tag{2.64}$$

Defining the vectors for collision rate

$$\{\mathbf{f}\}_i \equiv \Sigma_i \phi_i V_i. \tag{2.65a}$$

the partial currents

$$\{\mathbf{j}_+\}_\alpha \equiv S_\alpha J^\nu_{+,\alpha}. \quad \text{and} \quad \{\mathbf{j}_-\}_\alpha \equiv S_\alpha J^\nu_{-,\alpha}. \tag{2.65b}$$

and the source

$$s_i \equiv S_i V_i. \tag{2.65c}$$

the source q_i given by Eq. (2.63) can be written in the vector form as

$$\mathbf{q} = \mathbf{C}\,\mathbf{f} + \mathbf{s}. \tag{2.66}$$

where **C** is a diagonal matrix defined by

$$\{\mathbf{C}\}_{ij} = \delta_{ij} \frac{\Sigma_j^s}{\Sigma_j}. \tag{2.67}$$

Thus Eqs. (2.23) & (2.26), can be written in the matrix for as

$$\mathbf{f} = \mathbf{P_{VV}}\,\mathbf{q} + \mathbf{P_{VS}}\,\mathbf{J}^-. \tag{2.68}$$

$$\mathbf{J}^+ = \mathbf{P_{SV}}\,\mathbf{q} + \mathbf{P_{SS}}\,\mathbf{J}^-. \tag{2.69}$$

where P_{VV} is defined as the matrix of region to region, P_{VS} as the matrix of surface to region, P_{SV} as the matrix of region to surface and P_{SS} as the surface to surface collision probabilities respectively. The boundary condition used here is in the form of a relation between the average outgoing angular flux on surface S_β and the average incoming angular flux on a different surface S_α. In matrix form this can be written as

$$\mathbf{J}^- = \mathbf{A}\,\mathbf{J}^+. \tag{2.70a}$$

In case of albedo boundary condition, the coupling boundary condition matrix can be written as

$$A^{\nu\mu}_{\alpha\beta} = \beta_\alpha \delta_{\alpha\beta} \delta^{\nu\mu}. \tag{2.70b}$$

where β_α is the reflection coefficient at surface α. In the case of vacuum boundary condition $\beta_\alpha = 0$ will be used (as in TRANPIN) whereas in the case of total reflection at surface α, $\beta_\alpha = 1$ (for VISWAM) is used.

So Eq. (2.69) takes the form

$$\mathbf{J}^{+} = (\mathbf{I} - \mathbf{A}\mathbf{P}_{\mathbf{SS}})^{-\mathbf{1}}\, \mathbf{P}_{\mathbf{SV}}\, \mathbf{q}. \tag{2.71}$$

Eqs. (2.68) & (2.71) are iteratively solved using the conventional inner-outer iteration scheme to calculate partial currents across the surfaces and collision rates in each region. Also a self scattering reduction scheme is adopted for Eq. (2.68) *i.e.* all the information of self scattering of a group is transferred to left side so that Eq. (2.68) takes the following form

$$\mathbf{f} = (\mathbf{I} - \mathbf{C})^{-\mathbf{1}}(\mathbf{P}_{\mathbf{VV}}\, \mathbf{s} + \mathbf{P}_{\mathbf{VS}}\, \mathbf{J}^{-}). \tag{2.72}$$

2.8 Summary

The detailed theoretical formulation of interface current method based on 2D collision probability, implemented in lattice code VISWAM and core calculation TRANPIN, is presented in this Chapter. The interface current method is based on the integral form of transport of equation. Starting with the integro–differential form of transport equation, the integral transport equation is derived for an arbitrary volume *V* within the system. The integral transport equation is discretized over the solution domain which results in two linear equations for collision densities in the discretized zones of region *V* and outgoing currents from the surfaces of region *V*. The two linear equations for collision densities and outgoing neutron current have four collision probability matrices. These collision probability matrices are simplified for application to the hexagonal 2D geometry. The expressions for the matrices are obtained by simplifying the 3D space and surface integrals for application to 2D geometry. The expressions for angular dependent components of the collision probability matrices are obtained by considering the

angular flux expansion in double P_2 Legendre polynomials. Two quadrature sets for angular variable and one for the ordinate variable are available for numerical evaluation of the collision probability matrices. A numerical scheme is used to modify the collision probability matrices so as to preserve the conservation relations in order to guarantee neutron balance. The power iteration method is used to solve the linear set of discretized equations.

CHAPTER – 3

BENCHMARKING AND VALIDATION OF SINGLE ASSEMBLY CALCULATION

As discussed in Chapter 1, the application of DP2 expansion of angular flux in hexagonal geometry is not reported in literature. So it was essential to test this method for single fuel assembly (FA) before employing this method for core calculation. Therefore the interface current method using DP2 expansion was implemented in the lattice analysis code VISWAM [10, 48]. The mathematical formulation of the interface current method is described in detail in Chapter 2 and the Appendices thereof. A detailed benchmarking and validation exercise was taken up for the present method incorporated in VISWAM. Two benchmark problems, viz. a heterogeneous benchmark problem that is typical of a high temperature reactor (HTTR) proposed by Zhang et al. [49] and VVER – 1000 OECD lattice burnup computational benchmark [50], are studied using VISWAM. The present research work is oriented towards the development of TRANPIN code into a full 3D whole core transport theory code to study burnup dependent fuel cycle characteristics. The VVER – 1000 OECD computational benchmark was specially chosen to study the detailed lattice level burnup characteristics with the DP2 method incorporated in VISWAM as this study is not available in literature. This chapter gives the results of benchmarking and validation exercise in VISWAM.

3.1 HTTR Benchmark

Zhang et al. [49] have proposed a simplified heterogeneous benchmark problem that is typical of a high temperature reactor. The primary aim of benchmark is to assess the accuracy of diffusion or transport methods for reactor calculations. The benchmark is derived from the

experimental data of High Temperature Engineering Test Reactor (HTTR) start-up experiments, which was built by Japan in the late 1990s. The HTTR is a high-temperature gas cooled prismatic block reactor. The HTTR has helium as coolant and graphite in fuel blocks serves as the moderator. The fuel pins consist of fuel compacts, which are composed of coated UO2 fuel particles (TRISO) embedded in a graphite matrix. For reactivity control, the reactor contains burnable poison (BP) rods, composed of boron carbide and carbon, and control rods (CR), consisting of B4C and carbon inside an Alloy 800H sleeve [49]. However in the present benchmark, many design specific details of HTTR have been simplified. For instance the coated fuel particles and the graphite matrix are homogenized into a mixed fuel material. The benchmark problem is therefore heterogeneous down to the pin level. Due to this no double heterogeneity treatment of TRISO fuel particle is required. The problem, however, retains the significant features from a neutronics point of view such as realistic heterogeneity at the block level. The details of physics simplifications and justifications thereof can be found in [49].

Two geometric configurations in [49] have been analyzed *viz*. the single pincell and single fuel block in the present work. The fuel block and fuel pin considered in the benchmark problem, shown in Fig. 3.1, have a hexagonal shape. The fuel pin pitch is 5.15cm and fuel pin diameter is 4.1cm. The fuel block consists of 33 fuel pins, 3 burnable poison (BP) rods and one central graphite pin as shown in Fig. 3.1. The BP rod has a diameter of 1.5 cm. The fuel block pitch is 36cm. The fuel pin and fuel block consider seven cases of fuel enrichment ranging from 3.4 to 9.9 wt%. The benchmark provides the six group macroscopic cross section for all the materials required. These cross sections had been obtained by the benchmark proposers using detailed lattice calculations by HELIOS code system. The benchmark gives the results calculated using MCNP5 with this 6-group cross section library.

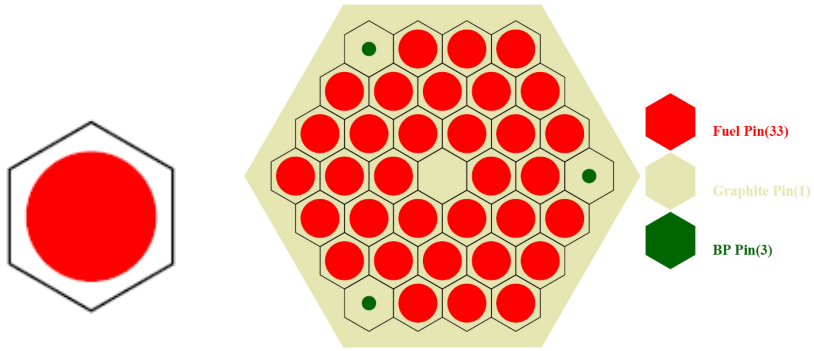

Fig. 3.1 – Fuel Pin and Fuel Assembly Cell

3.2 Discretization of the Geometry

In order to calculate multiplication factor and flux we need to calculate the four types of collision probability (CP) matrices defined in Eqs. (2.40), (2.42), (2.47) and (2.50). For pincell geometry, the mesh structure considered is shown in Fig. 3.2. The fuel and coolant regions were divided into finer circular regions. The fuel region was divided in three regions of equal volume and outside coolant region was divided into eight regions of equal thickness. As a result the pincell has annular shells embedded in the hexagonal geometry. Due to annular structure inside the hexagon, 1D annular treatment was done to calculate region to region collision probabilities for circular regions i.e. the integration over azimuthal angle in Eqs. (2.40) & (2.42) is performed analytically and only y integration is evaluated numerically. Only for the outermost region 2D method was required. The albedo boundary condition with reflection coefficient of unity is used at each of the six surfaces of the hexagonal pincell for single pincell calculation.

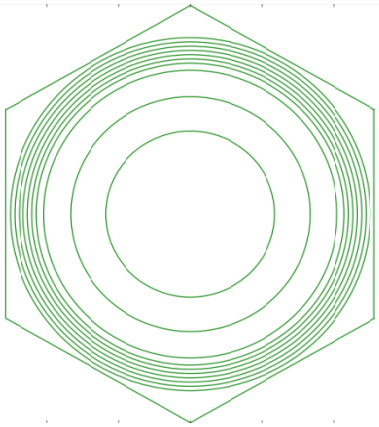

Fig. 3.2 – Mesh Division inside Single Hexagonal Pincell

For fuel assembly calculation, the collision probability matrices need to be calculated only for materially and geometrically distinct regions. The geometry of the hexagonal FA is modeled exactly. As seen in Fig. 3.1, there is a thin layer of coolant/moderator beyond the regular hexagonal structure in the fuel assembly. It is important to treat this region accurately. It is noted that in some recipes this thin region is artificially expanded into full regular hexagonal structure [10]. Any inaccurate modeling of this layer could create unwarranted errors in core calculation. To alleviate this problem in the fuel assembly cell, beyond the regular hexagonal structure, two different geometric meshes are identified which are designated as side mesh (Fig. 3.3a) and corner mesh (Fig. 3.4a). The mesh division in the regular hexagonal cells is similar to what was used for pincell calculation. The mesh division in the side and corner cells is as shown in the Figs. 3.3b & 3.4b. For HTTR benchmark, within the regular hexagon structure, three materially distinct regions were identified *viz*. fuel pin, BP pin and graphite pin. Thus there are totally five identified distinct zones (three regular hexagon + side + corner cells) for the fuel assembly calculation. Once the CP matrices are computed for these distinct zones, the flux and multiplication factor is calculated by an iterative procedure. The boundary condition is applied at the outer boundary surfaces of side and corner meshes.

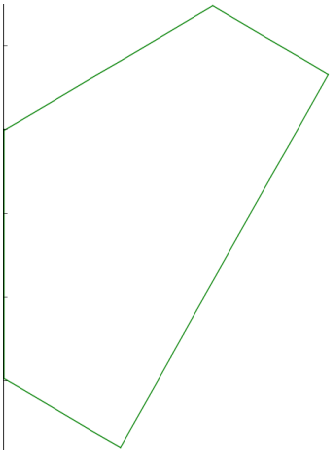

Fig. 3.3a – Side Mesh

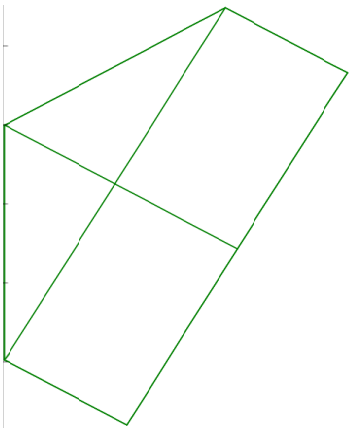

Fig. 3.3b – Mesh Division Inside Side Mesh

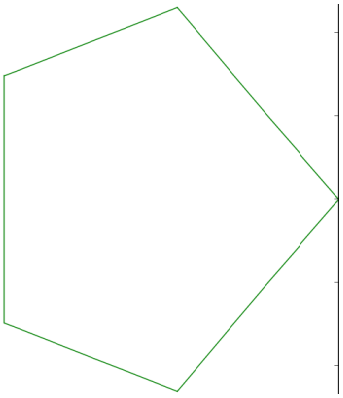

Fig. 3.4a – Corner Mesh

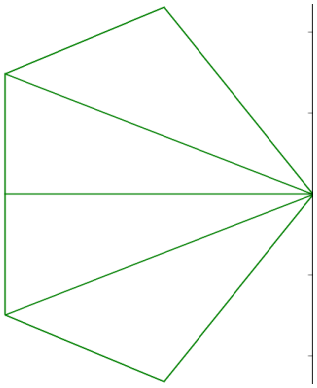

Fig. 3.4b – Mesh Division inside Corner Mesh

3.3 Results of HTTR Benchmark

The VISWAM results for single pincell and fuel block are compared with the benchmark results. The results of MOCUM code system of Yang et al. [27] are also included for comparison. MOCUM is based on the method of characteristics (MOC) and uses fine unstructured triangular meshes for discretization of the geometry. The convergence criterion for pincell calculation was taken as 10^{-9} for k_{∞} and 10^{-8} for flux, whereas, for FA calculation these criterions are 10^{-7} and 10^{-6} respectively. All the VISWAM results are obtained with 32 azimuthal angles and a ray separation of 0.0396cm. Gauss–Legendre quadrature is used for angular integration of collision

probability integrals. Table 3.1 gives the comparison of multiplication factor calculated with DP0 model for single pincell (DP1/DP2 model is not applicable to single pincell) with MOCUM & Monte Carlo results of benchmark for all seven fuel enrichments. The MOCUM code has used 1/12 hexagon for unit cell calculation and 1/6 hexagon for assembly calculation. The discretization parameters used in MOCUM are: 24 azimuthal angles, 0.01 cm ray spacing and 10^{-7} multiplication factor convergence criterion [27]. The results show a good agreement with a maximum deviation of 0.01% in k_∞ w.r.t. the Benchmark and MOCUM results.

Table 3.2 gives the comparison of k_∞ for seven fuel assembly types with DP0 model in VISWAM. The deviation of (–0.182%) w.r.t. benchmark is obtained for first enrichment (–0.148% w.r.t. MOCUM) whereas the deviation for all other enrichments is within ±0.08% (±0.06% w.r.t. MOCUM). Table 3.3 gives the results with VISWAM k_∞ obtained using DP1 and DP2 expansion of angular flux. The results with DP1/DP2 expansion show maximum error of –0.176%/–0.168% for first enrichment. The maximum error for other enrichments is found within ±0.08% for both DP1 and DP2 results. In the current problem with graphite moderator there is no steep flux gradient within the fuel assembly as may be present in an assembly with light water as moderator. Therefore the use of DP1 expansion is rather adequate to get the results within desirable accuracy. Use of higher order DP2 expansion functions gives nearly the same eigenvalue.

Tables 3.1 & 3.2 also compare the typical running time for VISWAM and MOCUM results. The VISWAM results are obtained on a windows machine equipped with 3.0GHz dual core processor and 2GB RAM. It is seen that VISWAM CPU time is significantly less compared to MOCUM but the accuracy achieved is comparable. Also it should be noted that MOCUM code is parallelized version and runs on advanced configuration machines whereas the VISWAM is running in serial mode only. It is seen from Table 3.3 that the DP1 and DP2 models require 8

or 13 sec compared to 5 sec of DP0 model due to the computation of extra components of CPs for higher angular flux expansion.

Fig. 3.5 gives the comparison of fission density distribution, obtained using DP2 expansion, for first enrichment type with benchmark results. The statistical uncertainties for benchmark results are less than 0.01%. The comparison is good and shows a maximum absolute deviation of 0.78%. The RMS error in the power distribution is seen as 0.13%. No significant differences in fission density distribution were noted with DP0 and DP1 expansion for first enrichment. Figs. 3.6 to 3.11 give the fission density distribution for other enrichment types using DP0 and DP2 expansion functions. This data is not available in the benchmark. The maximum absolute deviation of 0.2% is observed for enrichments of 4.8% & 5.2% between DP0 and DP2 values. This maximum absolute deviation is seen as 0.3% for enrichments of 6.3%, 6.7%, 7.9% and 9.9%. The %RMS errors for fuel of enrichments 4.8% & 5.2% are 0.02%, 0.03% for enrichments of 6.3%, 6.7%, 7.9%, and 0.04% for enrichment of 9.9% respectively.

Table 3.1 – Comparison of k_∞ for Pincell with VISWAM DP0 Model

Enrichment (wt.%)	k_∞			Δk/k(%) w.r.t.		Run Time(sec)	
	VISWAM	MOCUM	Benchmark (±0.00002)	Benchmark	MOCUM	VISWAM	MOCUM
3.4	1.13512	1.13516	1.13519	0.01	0.00	1.0	19.1
4.8	1.19575	1.19584	1.19577	0.00	0.01	1.0	14.5
5.2	1.20683	1.20694	1.20688	0.00	0.01	1.0	13.2
6.3	1.23524	1.23530	1.23531	0.01	0.01	1.0	12.0
6.7	1.24322	1.24333	1.24326	0.00	0.01	1.0	11.7
7.9	1.26042	1.26044	1.26044	0.00	0.00	1.0	10.7
9.9	1.28922	1.28926	1.28933	0.01	0.00	1.0	10.4

Table 3.2 – Comparison of k_∞ for Fuel Assembly with VISWAM DP0 Model

Enrichment (wt.%)	k_∞			Δk/k(%) w.r.t.		Run Time	
	VISWAM	Benchmark (±0.00002)	MOCUM	Benchmark	MOCUM	VISWAM (sec)	MOCUM (min)
3.4	1.03930	1.04119	1.04084	–0.182	–0.148	5.0	4.48
4.8	1.15214	1.15307	1.15283	–0.080	–0.060	5.0	3.76
5.2	1.17212	1.17287	1.17265	–0.064	–0.045	5.0	3.61
6.3	1.22183	1.22212	1.22192	–0.024	–0.007	5.0	3.31
6.7	1.23790	1.23802	1.23787	–0.010	0.002	5.0	3.05
7.9	1.27344	1.27323	1.27305	0.016	0.030	5.0	2.80
9.9	1.32022	1.31962	1.31951	0.046	0.054	5.0	2.40

Table 3.3 – Comparison of k_∞ for Fuel Assembly with Higher Expansion of Angular Flux

Enrichment (wt.%)	k_∞			Δk/k(%) w.r.t. Benchmark		VISWAM Run Time (sec)	
	VISWAM		Benchmark (±0.00002)	DP1	DP2	DP1	DP2
	DP1	DP2					
3.4	1.03936	1.03944	1.04119	–0.176	–0.168	8.0	13.0
4.8	1.15238	1.15244	1.15307	–0.060	–0.054	8.0	13.0
5.2	1.17238	1.17245	1.17287	–0.041	–0.036	8.0	13.0
6.3	1.22217	1.22223	1.22212	0.004	0.009	8.0	13.0
6.7	1.23821	1.23826	1.23802	0.015	0.019	8.0	13.0
7.9	1.27385	1.27390	1.27323	0.049	0.052	8.0	13.0
9.9	1.32070	1.32074	1.31962	0.081	0.084	8.0	13.0

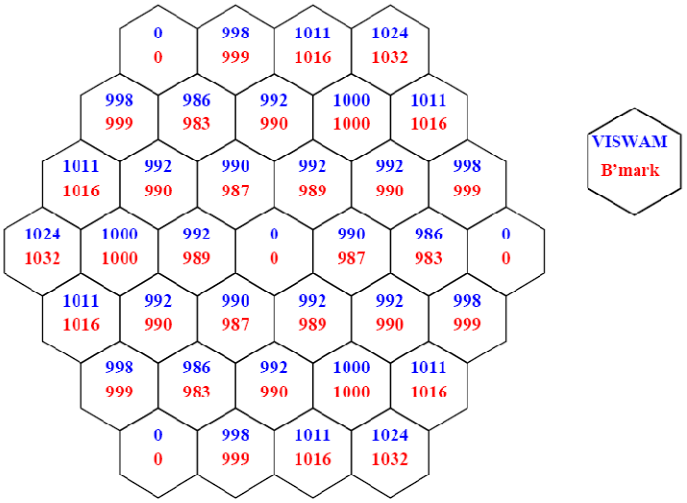

Fig. 3.5 – Comparison of Fission Density Distribution for 3.4% Enrichment (Uncertainty in Benchmark Results <0.01%)

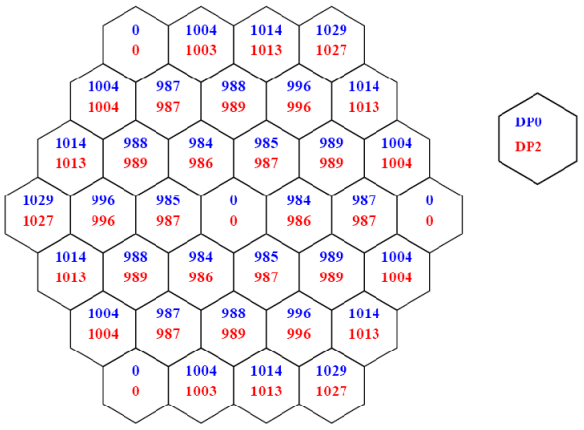

Fig. 3.6 – Fission Density Distribution for 4.8% Enrichment

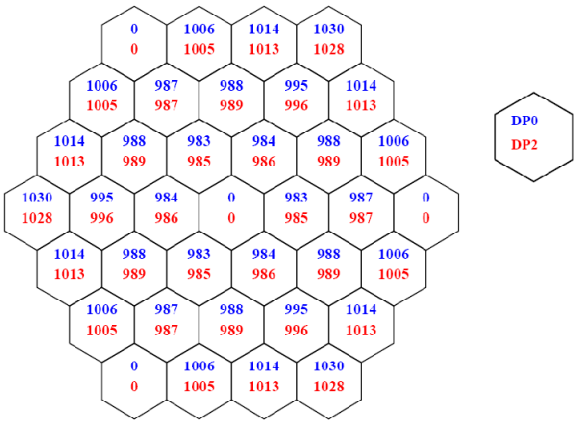

Fig. 3.7 – Fission Density Distribution for 5.2% Enrichment

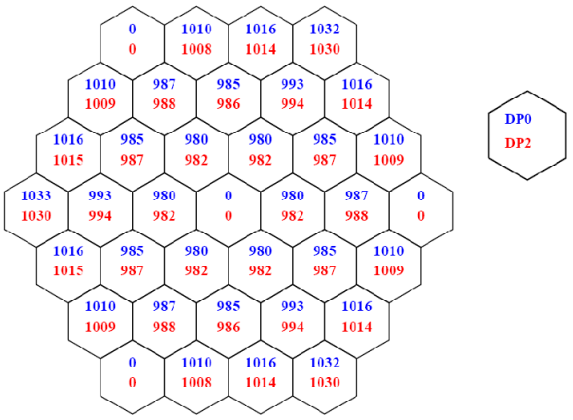

Fig. 3.8 – Fission Density Distribution for 6.3% Enrichment

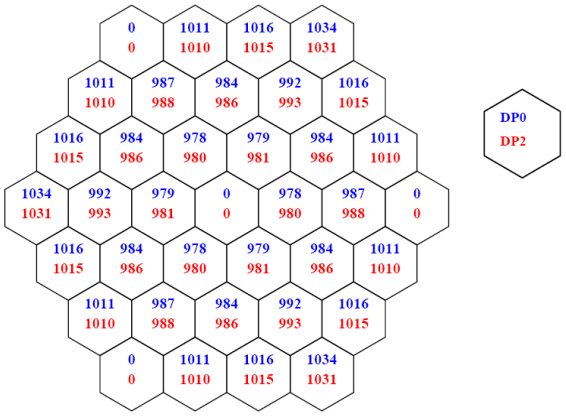

Fig. 3.9 – Fission Density Distribution for 6.7% Enrichment

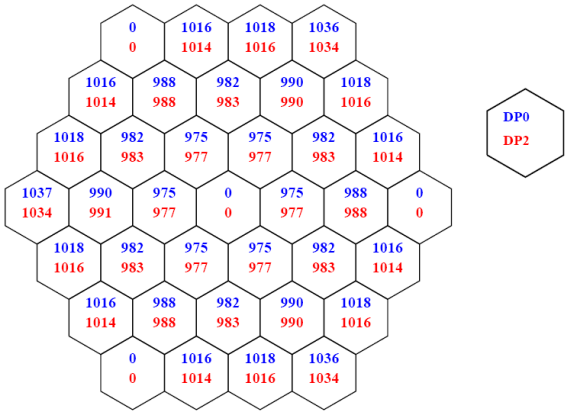

Fig. 3.10 – Fission Density Distribution for 7.9% Enrichment

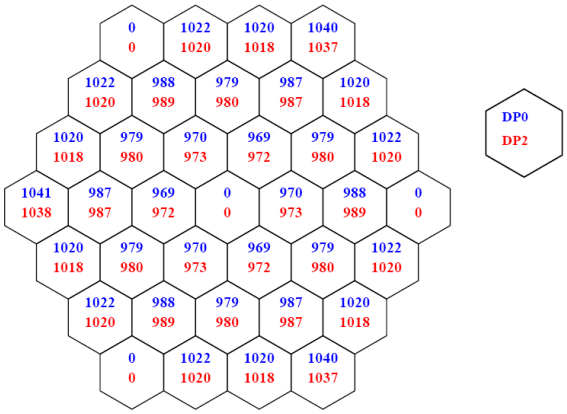

Fig. 3.11 – Fission Density Distribution for 9.9% Enrichment

3.3.1 Sensitivity of k_∞ on Discretization Parameters

The k_∞ of the fuel assembly depends on the discretization parameters used to calculate the collision probability matrices of the distinct zones and the expansion of angular flux on the surfaces of these zones. In order to evaluate these effects, a sensitivity study was performed by varying the discretization parameters for fuel of enrichment 4.8%. Two azimuthal angle sets of 32 & 64 are used. Four track separations of 0.1189, 0.0595, 0.0238 & 0.0119cm are used for each azimuthal angle set. The angular flux expansions of DP0, DP1 & DP2 were used for each combination of azimuthal angle and track separation. Table 3.4 gives the k_∞ values obtained for each discretization set using three angular expansions and their % deviation from the benchmark value. A horizontal glance in Table 3.4 shows that once an optimum discretization parameter set is obtained, there is no significant improvement in the Eigenvalue. Therefore four sets of track separation were only studied. Also the finer angular discretization of azimuthal angles doesn't change the k_∞ values significantly, but it increases the virtual memory requirement and

computation time for the problem. However, the expansion of the angular flux affects the Eigenvalue more strongly as seen from Table 3.4.

The k_∞ of the fuel assembly can also depend on the mesh discretization considered within the single pincell shown in Fig. 3.2. Table 3.5 gives the results of the sensitivity study of this discretization on k_∞. In this study three configurations are considered in which the fuel region of the pincell is divided in 3, 4 and 5 concentric rings. For each of this configuration, the outer graphite region of the pincell is varied by dividing it into a set of 7, 8, 9 and 10 rings. 32 azimuthal angles and a track separation of 0.0396 cm is used for evaluation the collision probability matrices. As seen from Table 3.5, the finer mesh discretization does not affect the Eigenvalue strongly in comparison to angular flux expansion. It may be noted that the above observation is specific to the problem analyzed. In some other problem with steep flux gradients fine mesh discretization may be warranted

Table 3.4 – Sensitivity of k_∞ with Discretization Parameters *vis–a–vis* Angular Expansion of Flux for Fuel Assembly (for 4.8% Fuel)

Order of Angular Expansion of Flux	Number of Azimuthal Angles							
	32				64			
	Track separation (cm)				Track separation (cm)			
	0.1189	0.0595	0.0238	0.0119	0.1189	0.0595	0.0238	0.0119
DP0	1.15202	1.15214	1.15214	1.15215	1.15204	1.15214	1.15215	1.15216
DP1	1.15224	1.15238	1.15237	1.15239	1.15225	1.15237	1.15239	1.15239
DP2	1.15230	1.15244	1.15244	1.15246	1.15231	1.15243	1.15246	1.15246
	Δk/k(%) w.r.t. Benchmark value of 1.15307(±0.00002)							
DP0	–0.091	–0.080	–0.081	–0.079	–0.090	–0.081	–0.080	–0.079
DP1	–0.072	–0.060	–0.061	–0.059	–0.071	–0.061	–0.059	–0.059
DP2	–0.066	–0.054	–0.055	–0.053	–0.066	–0.055	–0.053	–0.053

Table 3.5 – Sensitivity of k_∞ with Mesh Discretization within Pincell for Fuel Assembly (for 4.8% Fuel)

Order of Angular Expansion of Flux	Number of Azimuthal Angles=32, Track Separation = 0.0396 cm											
	No. of fuel rings=3				No. of fuel rings=4				No. of fuel rings=5			
	No. of coolant rings				No. of coolant rings				No. of coolant rings			
	7	8	9	10	7	8	9	10	7	8	9	10
DP0	1.152196	1.152194	1.152193	1.152193	1.152195	1.152194	1.152193	1.152192	1.152195	1.152194	1.152193	1.152193
DP1	1.152443	1.152441	1.152441	1.152440	1.152442	1.152441	1.152440	1.152440	1.152443	1.152441	1.152440	1.152440
DP2	1.152510	1.152508	1.152507	1.152507	1.152509	1.152508	1.152507	1.152507	1.152510	1.152508	1.152507	1.152507

3.4 VVER–1000 OECD Computational Benchmark

The VVER–1000 computational benchmark has been proposed by the expert group at OECD/NEA. The primary aim of the benchmark is to certify the calculation codes for utilizing weapons grade (WG) plutonium by converting it to mixed–oxide (MOX) fuel for nuclear reactors. The benchmark model consists of two different assemblies that are typical of the advanced Russian designs of the VVER–1000 reactor [50]. The benchmark exercise consists of two assembly types: a uniform LEU fuel assembly with 12 U/Gd rods (UGD variant) and a profiled MOX fuel assembly with 12 U/Gd rods (MOXGD variant). The VVER–1000 FA is hexagonal in shape having 331 lattice locations. In the UGD FA, 331 locations are distributed into 312 fuel pin locations (12 of which are U/Gd rods), one central tube and 18 guide tubes as shown in Fig. 3.12. The fuel pins in UGD FA have 3.7 wt.% enrichment. The 12 U/Gd pins have a ^{235}U enrichment of 3.6 wt.% and a Gd_2O_3 content of 4.0 wt.%. The MOXGD assembly, shown in Fig. 3.13, contains fuel rods with three different plutonium loadings. The central region of 138 fuel pins contains MOX with 4.2 wt.% fissile plutonium (containing 93 wt.% ^{239}Pu), two rings of 96 fuel rods has 3.0 wt.% fissile plutonium, and an outer ring of 66 fuel rods is loaded with 2.0 wt.% fissile plutonium. The 12 U/Gd rods in MOXGD FA are in the same locations as in the UGD assembly configuration and have the same Uranium and Gd content.

The benchmark exercise required the calculations to be performed in various reactor states. These states are listed in Table 3.6. The calculation in S1 state is to be performed up to burnup of 40 MWd/KgHM using the power density of 108 MWth/m^3 (corresponding linear heat rate of 166.2 W/cm). The calculation at other states (S2 to S5) is to be done using the number densities generated in S1 state at burnup levels of 0, 20 & 40 MWd/KgHM. The requested results include k_∞, assembly average isotope concentrations and average concentrations in selected cells

with burn-up for S1 state and k_∞ and fission rate distributions at burnup 0, 20, and 40 MWd/kgHM for states S2 to S5.

Table 3.6 – Calculation States

State	Description	Fuel Temp(K)	Non–Fuel Temp(K)	^{135}Xe & ^{149}Sm	Boron (ppm)	Moderator Density(g/cc)
S1	Operating poisoned state	1027	575	Equilibrium Conc.	600	0.7235
S2	Operating non–poisoned state	1027	575	0.0	600	0.7235
S3	Hot state	575	575	0.0	600	0.7235
S4	Hot state without boric acid	575	575	0.0	0	0.7235
S5	Cold state	300	300	0.0	0	1.0033

3.5 Nuclear Data Used

The benchmark provides the isotopic composition of all the materials required in the problem. VISWAM uses multi group cross section libraries in WIMS/D format for lattice level calculations. The present calculations were done using a high temperature library 'HTEMPLIB' based on JEFF–3.1 nuclear data library [31]. This library has cross section data for 185 nuclides in 172 energy groups. The burnup chain in HTEMPLIB library is extended up to ^{252}Cf. The library has resonance tabulation for 48 nuclides. The resonance integral tables are available up to a temperature of 2500 K. Equivalence relations are used for obtaining resonance self-shielded cross sections. Mutual shielding of a mixture of resonance nuclides is treated in accordance with the procedures described by Stammler and Abbate [51]. For the burnable poison nuclide Gd, only five isotopes viz. ^{154}Gd, ^{155}Gd, ^{156}Gd, ^{157}Gd, ^{158}Gd are available in the HTEMPLIB library. The isotopes ^{152}Gd &^{160}Gd are not available. Since their absorption cross sections are negligible compared to those of ^{155}Gd or ^{157}Gd, the concentration of ^{152}Gd & ^{160}Gd given in benchmark specification were added to those of ^{154}Gd &^{158}Gd respectively. It is believed that this approximation would have negligible influence on the quality of results of the analysis.

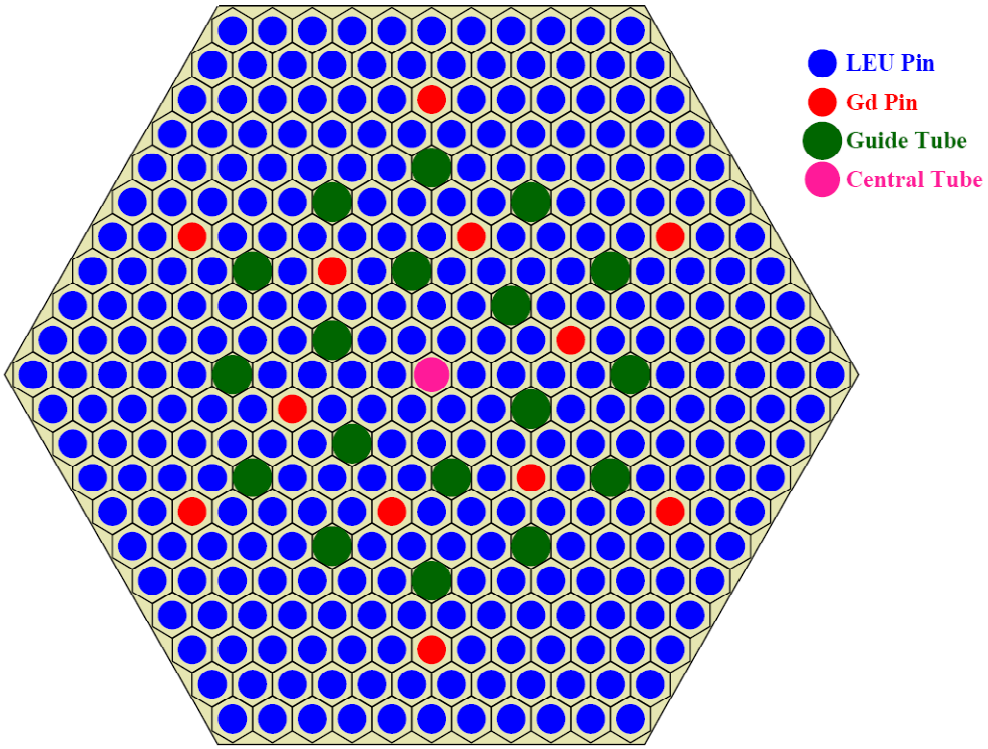

Fig. 3.12 – UGD Fuel Assembly

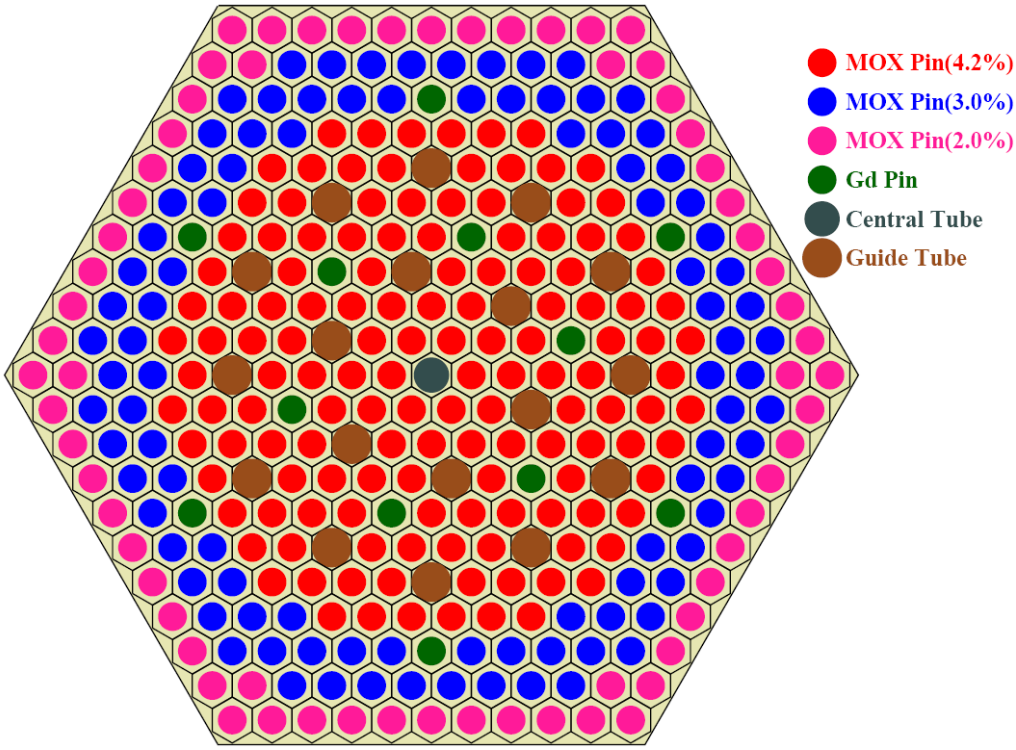

Fig. 3.13 – MOXGD Fuel Assembly

3.6 Results of VVER–1000 OECD Computational Benchmark

The two lattice analysis methods available in VISWAM code system, as described in Chapter 1, are used to study the present benchmark. In the tables and figures, the hybrid method of 1D transport and 2D diffusion theory is denoted by PIJ=1 and the interface current method is described by PIJ=2. The results of PIJ=2 are further split into three descriptions: DP0, DP1 and DP2. These three descriptors correspond to the results obtained by using DP0, DP1 and DP2 expansion of angular fluxes respectively, at the surfaces of distinct cells. All the results are obtained with convergence criterion of 10^{-7} & 10^{-5} for multiplication factor and scalar flux respectively. The results in the following Section 3.6.1 discusses the need to consider higher order expansion of angular flux in interface current method. The detailed benchmark results and comparison thereof is presented in subsequent sections. The mesh division inside single pincell, side and corner mesh in the fuel assembly is similar to that discussed in Section 3.2. The fuel region is divided in three regions of equal volume, one region is considered in clad and outside coolant region is divided into seven regions of equal thickness.

3.6.1 Effect of Expansion of Angular Flux

The Eigenvalue depends on the discretization parameters of the problem and order of expansion terms in the angular flux. In order to quantify the effects of the angular expansion of the interface current on the solution vis–à–vis the discretization parameters of the problem, a sensitivity study is performed. This study is performed only for UGD FA in S2 state at zero burnup. All the results in this section are obtained using 172 group JEFF–2.2 library [32] since the reference MCNP4B results available in the benchmark report [50] have used this data library in continuous energy format. Table 3.7 gives the k_∞ values obtained using two azimuthal angle sets. The track separation for each angular set is varied from 0.03 cm to 0.003 cm. As seen from

Table 3.7, the k_∞ values do not vary significantly after an optimum discretization. However, the k_∞ obtained by using higher order flux anisotropy shows an improved matching with reference MCNP result. The results obtained using DP1 anisotropy show an improvement of around 4 mk in k_∞ as compared to DP0 values and 0.5 mk using DP2 anisotropy w.r.t. DP1 values. Here it should be noted that the difference in eigenvalue w.r.t. MCNP can be due to certain approximations used in VISWAM code, notably the resonance self shielding model using equivalence principles and the treatment of overlapping of resonance absorption of various fuel nuclides. However, since these approximations are present in all the three calculations using DP0, DP1 and DP2 anisotropy, the relative difference between the three calculations gives the numerical estimate of the effect of angular flux expansion.

Table 3.8 gives the comparison of k_∞ and deviation in mk from reference MCNP values for states S2 to S5 for UGD & MOXGD FAs. The results obtained using DP0, DP1 & DP2 terms are compared with reference MCNP values. As seen from Table 3.7, the discretization parameters of 32 azimuthal angles and track separation of 0.01cm are optimum. The results in Table 3.8 and subsequent sections are obtained using this set of discretization parameters. As seen from Table 3.8, the multiplication factor k_∞, for both UGD & MOXGD FAs, shows a gradually improved matching with MCNP results as the order of flux anisotropy is increased. The results with DP2 anisotropy are closest to MCNP values. This shows the need to consider higher order anisotropy in angular flux in the codes using interface current method.

Table 3.7 – Variation of k_∞ with Discretization Parameters and Angular Expansion of Flux for UGD Fuel Assembly in S2 state

Order of Angular Expansion of Flux	Number of Azimuthal Angles							
	32				64			
	Track separation (cm)				Track separation (cm)			
	0.03	0.01	0.006	0.003	0.03	0.01	0.006	0.003
DP0	1.16932	1.17069	1.17059	1.17065	1.16936	1.17048	1.17065	1.170648
DP1	1.17479	1.17624	1.17604	1.17612	1.17449	1.17582	1.17613	1.17609
DP2	1.17552	1.17694	1.17679	1.17687	1.1751	1.17649	1.17683	1.17679
	$\Delta\rho$ (in mk) w.r.t. Benchmark value of 1.18000							
DP0	7.74	6.74	6.82	6.77	7.71	6.89	6.77	6.77
DP1	3.76	2.71	2.85	2.80	3.98	3.01	2.79	2.82
DP2	3.23	2.16	2.32	2.26	3.54	2.53	2.28	2.31

Table 3.8 – Comparison of Eigenvalue with Reference MCNP Results in Different States

Results of UGD FA								
	k_∞				$\Delta\rho$ (mk) w.r.t. MCNP			
	S2	**S3**	**S4**	**S5**	**S2**	**S3**	**S4**	**S5**
MCNP	1.18000	1.19250	1.25310	1.32350	–	–	–	–
DP0	1.17069	1.18630	1.24524	1.31307	6.74	4.38	5.04	6.00
DP1	1.17624	1.19118	1.25113	1.31784	2.71	0.93	1.26	3.24
DP2	1.17694	1.19187	1.25207	1.31875	2.16	0.44	0.66	2.72
Results of MOXGD FA								
MCNP	1.19220	1.20910	1.24300	1.32560	–	–	–	–
DP0	1.18122	1.20008	1.23407	1.31521	7.79	6.21	5.82	5.96
DP1	1.19002	1.20811	1.24349	1.32301	1.54	0.68	–0.32	1.48
DP2	1.19118	1.20918	1.24485	1.32424	0.72	–0.06	–1.20	0.78

The detailed pin by pin fission density distribution in 1/6th UGD fuel assembly for S2 state at zero burnup is compared with MCNP values. The pin wise location map of 1/6th fuel assembly, given in benchmark report, used for fission density comparison is shown in Fig. 3.14. The fission density distribution obtained using DP0, DP1 & DP2 expansion is compared with MCNP values in Fig. 3.15. The fission density distribution, in general, shows a satisfactory comparison with MCNP result. The maximum % relative deviation from MCNP values for DP0, DP1 and DP2 expansion is seen as –2.55%, 2.23% and 2.02% respectively. The %RMS

deviation in fission densities for three cases is seen to be 1.03%, 0.549% & 0.462% respectively. The minimum RMS deviation is seen for results obtained using DP2 expansion.

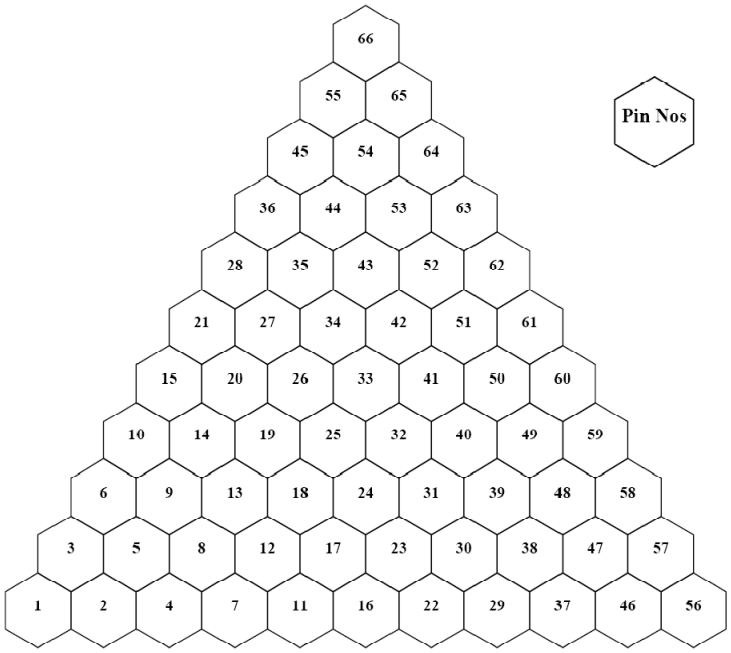

Fig. 3.14 – Pin numbers in 1/6th FA for fission density Comparison

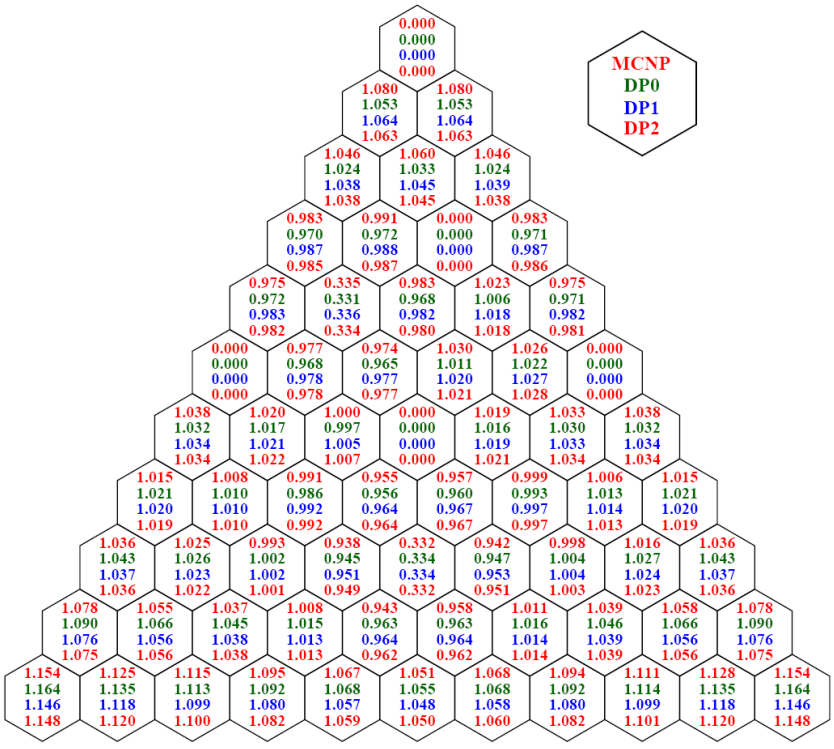

Fig. 3.15 – Fission density for 1/6th UGDFA in S2 state

3.6.2 Burnup Strategy for the Benchmark Analysis

With burnup, calculating CP matrices for all the fuel pins in the assembly is computationally expensive. In VISWAM, the unit cells are divided into fuel and non–fuel cells. The fuel cells are further divided into groups based on the enrichment and Dancoff factor, proximity to water pins and their location in the layer of fuel pins. Using this criterion, 6 non–fuel and 16 distinct fuel cells are identified for UGD FA. Six non–fuel and 17 distinct fuel cells are identified for MOXGD FA. The burnup type distribution is shown in Fig. 3.16 for both LEU & MOX FAs. The full hexagons in the outermost layer shown in the Fig. 3.16 are for representation purpose only. Actual size and shape of the meshes in outermost water layer is considered for simulation purpose. For burnup calculation, out of 397 locations (312 fuel pin cells and 19 water rod cells of regular hexagonal shape and 60 meshes of shape shown in Fig. 3.3a (side cells) and 6 meshes of shape shown in Fig. 3.4a (corner cells) pertaining to the thin outer water layer beyond regular cells), CP matrices are calculated for these geometrically and materially distinct cells only. At higher burnup, the CP calculation for non–fuel cells need not be performed. The S1 state was followed up to 40 MWD/KgHM using the power density of 108 MW/m^3 given in benchmark. The calculation is performed using burn up step of 0.25 up to 6 MWD/KgHM, 0.5 up to 10 MWD/KgHM, 1.0 up to 20 MWD/KgHM and 2.0 up to 40 MWD/KgHM. The fine burn up steps were selected up to 10 MWD/KgHM to model Gd depletion accurately. The calculation for states S2 to S5 are performed using the number densities generated in S1 state after setting the nuclide density of some nuclides like Xe, Sm to zero as may be required. It may be noted that for S1 state at zero burnup ^{135}Xe and ^{149}Sm are considered to be having equilibrium concentrations. In VISWAM code saturated xenon is considered at all burnups and samarium was considered to build up naturally. It normally

requires a few weeks to reach its equilibrium value. For the present analysis a special provision was made to compute the equilibrium concentration of ^{149}Sm at zero burnup.

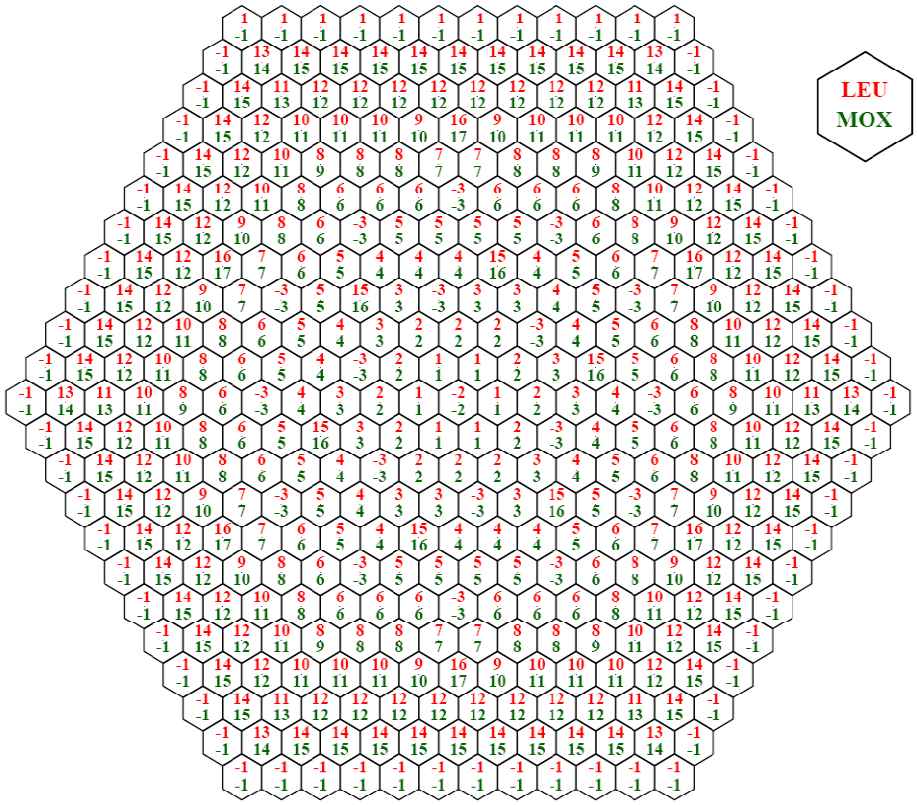

Fig. 3.16 – Burnup type Distribution considered in VISWAM for the two FA types of LEU & MOX (Negative nos. are for non fuel cells like water slots/GTs)

3.6.3 Comparison of Multiplication factor (k_∞)

Figs. 3.17 and 3.18 show the variation of k_∞ with burnup for S1 state for UGD FA and MOXGD FA respectively as compared with five other evaluations of MCU, TVS–M, WIMS8A, HELIOS, MULTICELL and benchmark mean (BM) values. Here the BM values refer to the arithmetic mean of all the submitted evaluations [50]. These values are given in Tables 3.9 and 3.10 for UGD FA and MOXGD FA respectively. Deviations in k_∞ from the BM values were estimated for the four VISWAM models as a function of burnup. For UGDFA, k_∞ obtained using PIJ=1 and PIJ=2 :(DP0, DP1 and DP2) show a deviation of –7.11, –9.50, –5.40 and –4.87 mk

respectively w.r.t. BM values at zero burnup. This deviation reduces to –5.64, –1.45, +0.81, +1.05 mk respectively at the burnup of 40 MWD/KgHM. At burnup of 7 MWD/KgHM the peak value of k_∞ is seen for PIJ=2 models whereas PIJ=1 model predicts the Gd peak at 6 MWD/KgHM. At this burnup the deviations in k_∞ are seen as –10.47, –8.08, –2.16 and –1.60mk respectively for the four VISWAM models. The Gd burning characteristics and peak is more accurately predicted with DP1/DP2 model. This is expected as DP1/DP2 model can predict the steep flux gradients across the Gd pincell more precisely compared to isotropic flux expansion and diffusion theory model. The MOXGD FA shows a difference of –7.04, –5.72, +0.32 and +1.11 mk for PIJ=1 and PIJ=2:(DP0, DP1 and DP2) models respectively w.r.t. BM values at zero burnup. These difference values are –6.71, –1.22, 0.00 & +0.07mk respectively at 40 MWD/KgHM burnup. The results for MOXGD FA show relatively less deviation in k_∞ with BM values compared to UGD FA with DP1 & DP2 models. It should be noted that the present analysis has been carried out using JEFF 3.1 dataset whereas the benchmark values are obtained using JEFF–2.2 or ENDFB–VI datasets. Overall the calculation with DP1/DP2 shows a satisfactory matching with BM and other evaluations given in benchmark report for both the variants of UGD FA and MOXGD FA.

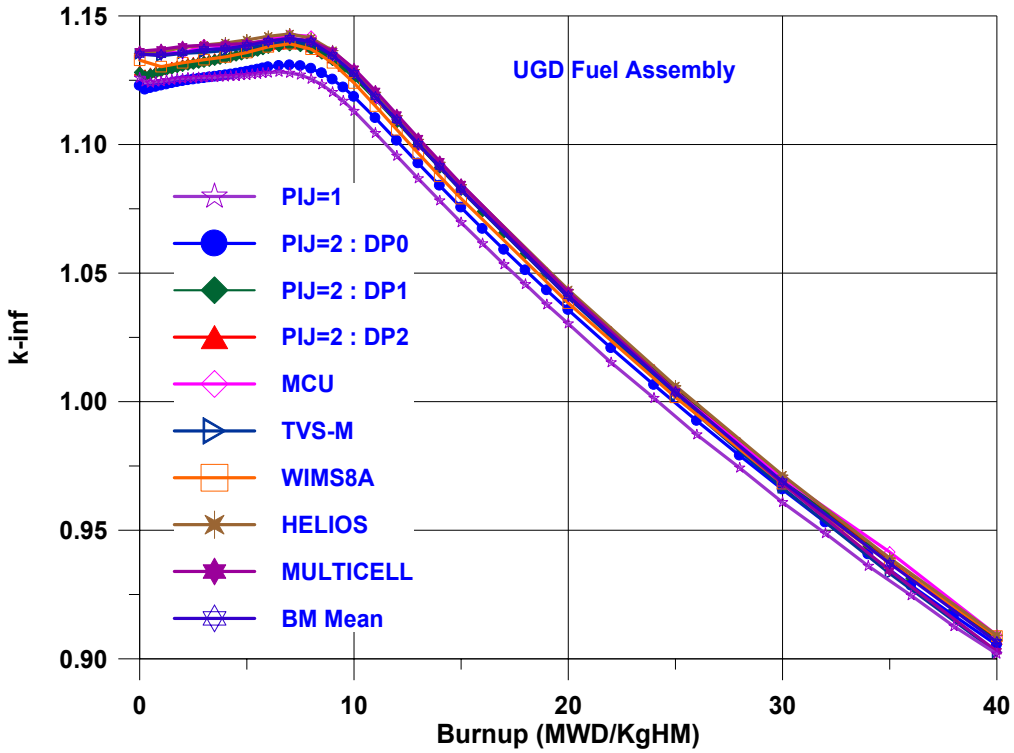

Fig 3.17 – Comparison of Multiplication Factor with burnup for UGD FA in S1 State

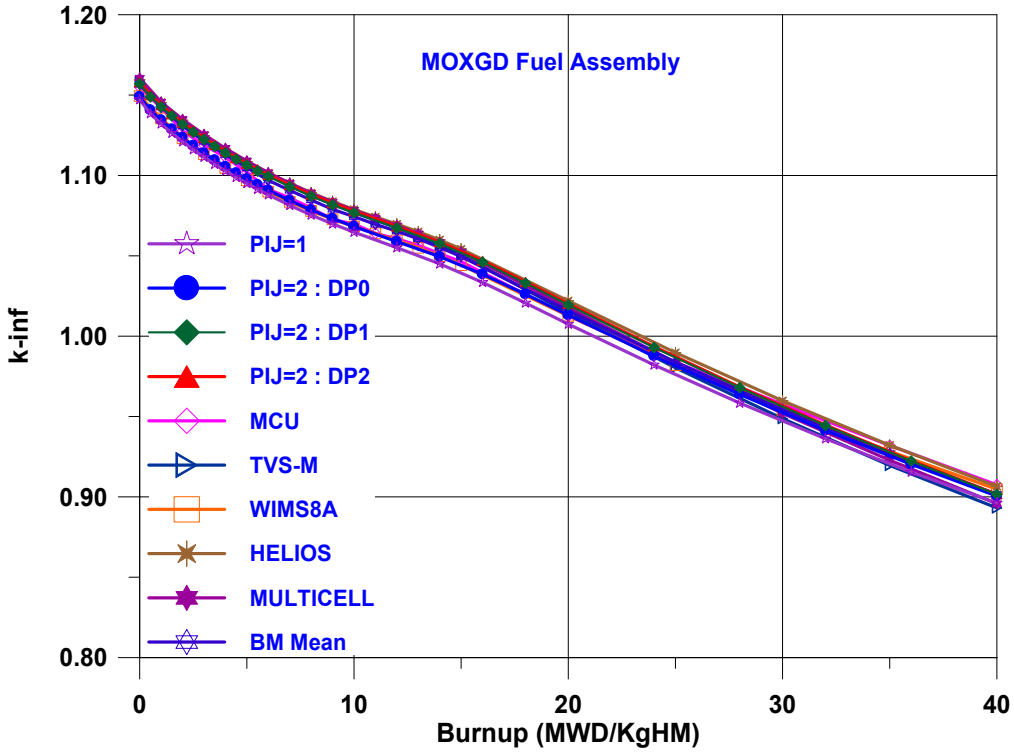

Fig 3.18 – Comparison of Multiplication Factor with burnup for MOXGD FA in S1 State

Table 3.9 – k_∞ of UGD FA in S1 state with burnup

Burnup (MWd/kgHM)	k_∞									
	PIJ=1	PIJ=2			MCU	TVS-M	WIMS8A	HELIOS	MULTICELL	BM MEAN
		DP0	DP1	DP2						
0	1.1259	1.1229	1.1281	1.1288	1.1353	1.1353	1.1328	1.1355	1.1363	1.1350
1	1.1245	1.1229	1.1284	1.1291	1.1364	1.1345	1.1303	1.1361	1.1370	1.1349
2	1.1256	1.1247	1.1305	1.1312	1.1354	1.1355	1.1318	1.1377	1.1382	1.1357
3	1.1260	1.1259	1.1321	1.1328	1.1388	1.1359	1.1330	1.1387	1.1386	1.1370
4	1.1264	1.1270	1.1336	1.1344	1.1377	1.1365	1.1341	1.1395	1.1389	1.1373
5	1.1269	1.1283	1.1354	1.1362	1.1390	1.1375	1.1358	1.1407	1.1394	1.1385
6	1.1279	1.1301	1.1375	1.1383	1.1408	1.1390	1.1380	1.1421	1.1404	1.1401
7	1.1278	1.1309	1.1385	1.1392	1.1427	1.1403	1.1392	1.1430	1.1414	1.1413
8	1.1255	1.1295	1.1371	1.1379	1.1421	1.1390	1.1371	1.1414	1.1404	1.1400
9	1.1204	1.1253	1.1328	1.1336	1.1344	1.1346	1.1318	1.1365	1.1363	1.1347
10	1.1130	1.1186	1.1259	1.1267	1.1284	1.1273	1.1240	1.1291	1.1295	1.1277
11	1.1044	1.1103	1.1175	1.1183	1.1178	1.1185	1.1150	1.1203	1.1209	1.1185
12	1.0956	1.1015	1.1086	1.1094	1.1099	1.1092	1.1058	1.1112	1.1117	1.1096
13	1.0867	1.0927	1.0997	1.1005	1.0996	1.1000	1.0966	1.1020	1.1025	1.1002
14	1.0782	1.0840	1.0909	1.0917	1.0923	1.0910	1.0877	1.0931	1.0935	1.0915
15	1.0696	1.0755	1.0823	1.0831	1.0827	1.0821	1.0790	1.0843	1.0846	1.0825
20	1.0303	1.0357	1.0419	1.0426	1.0403	1.0405	1.0383	1.0435	1.0427	1.0411
25	1.0014	1.0065	1.0120	1.0126	1.0039	1.0022	1.0017	1.0061	1.0041	1.0036
30	0.9608	0.9659	0.9701	0.9706	0.9703	0.9665	0.9681	0.9714	0.9681	0.9689
35	0.9361	0.9406	0.9439	0.9443	0.9415	0.9332	0.9372	0.9391	0.9343	0.9371
40	0.9019	0.9053	0.9072	0.9074	0.9091	0.9025	0.9088	0.9091	0.9029	0.9065

Table 3.10 – k_∞ of MOXGD FA in S1 state with burnup

Burnup (MWd/kgHM)	k_∞									
	PIJ=1	PIJ=2			MCU	TVS-M	WIMS8A	HELIOS	MULTICELL	BM MEAN
		DP0	DP1	DP2						
0	1.1473	1.1490	1.1570	1.1581	1.1551	1.1585	1.1494	1.1595	1.1606	1.1566
1	1.1322	1.1345	1.1427	1.1438	1.1421	1.1448	1.1355	1.1454	1.1457	1.1427
2	1.1211	1.1235	1.1319	1.1329	1.1278	1.1337	1.1232	1.1344	1.1349	1.1308
3	1.1114	1.1140	1.1224	1.1235	1.1188	1.1241	1.1133	1.1249	1.1255	1.1213
4	1.1028	1.1055	1.1140	1.1150	1.1114	1.1154	1.1047	1.1164	1.1169	1.1130
5	1.0950	1.0978	1.1063	1.1074	1.1020	1.1074	1.0970	1.1086	1.1090	1.1048
6	1.0879	1.0908	1.0994	1.1004	1.0914	1.1002	1.0899	1.1016	1.1017	1.0970
7	1.0814	1.0843	1.0929	1.0940	1.0860	1.0936	1.0836	1.0951	1.0951	1.0907
8	1.0754	1.0785	1.0871	1.0881	1.0798	1.0875	1.0779	1.0892	1.0890	1.0847
9	1.0698	1.0731	1.0817	1.0827	1.0725	1.0820	1.0728	1.0838	1.0834	1.0789
10	1.0647	1.0682	1.0768	1.0777	1.0698	1.0769	1.0682	1.0788	1.0783	1.0744
11	1.0598	1.0634	1.0719	1.0729	1.0640	1.0722	1.0639	1.0742	1.0735	1.0696
12	1.0550	1.0589	1.0673	1.0683	1.0606	1.0675	1.0596	1.0697	1.0688	1.0653
13	1.0502	1.0543	1.0626	1.0635	1.0565	1.0624	1.0550	1.0650	1.0638	1.0605
14	1.0450	1.0495	1.0575	1.0584	1.0514	1.0567	1.0498	1.0599	1.0583	1.0552
15	1.0394	1.0442	1.0520	1.0529	1.0463	1.0504	1.0442	1.0542	1.0523	1.0495
20	1.0075	1.0131	1.0194	1.0201	1.0126	1.0148	1.0127	1.0220	1.0178	1.0160
25	0.9821	0.9877	0.9929	0.9935	0.9837	0.9803	0.9820	0.9897	0.9836	0.9839
30	0.9471	0.9524	0.9560	0.9564	0.9577	0.9487	0.9540	0.9598	0.9520	0.9544
35	0.9256	0.9306	0.9332	0.9334	0.9320	0.9196	0.9283	0.9321	0.9228	0.9270
40	0.8961	0.9005	0.9015	0.9016	0.9075	0.8931	0.9048	0.9065	0.8958	0.9015

3.6.4 Reactivity Effects in different states

The different loads of reactivity in mk are calculated using the formula described below

$$\Delta\rho\ (in\ mk) = \left(\frac{1}{k_{final}} - \frac{1}{k_{initial}}\right) \times 1000$$

where the initial and final states are as given in Table 3.11.

Table – 3.11 Initial and Final States for Reactivity Loads

Reactivity Effect	Initial State	Final State
Xe+Sm	S1	S2
Doppler	S3	S2
Boron	S3	S4
Isothermal	S4	S5

3.6.4.1 Equilibrium Xe and Sm Poisoning Effect

Table 3.12 gives the equilibrium Xe and Sm loads for UGD and MOXGD FA variants calculated using four models. These results are compared with BM values. The calculated loads show a good agreement with BM values. Maximum difference is seen for DP0 model at zero burnup for both UGDFA and MOXGD FA. They are –0.41 mk and –0.99 mk respectively w.r.t. the BM values of 30.28 mk and 24.20 mk for the two types of FAs. At 40 MWD/KgHM burnup, the maximum deviation from BM values is observed for PIJ=1 results. They are –1.57 mk and –1.55 mk for the two fuel types w.r.t. BM values of 38.63 and 36.65 mk. It is seen that the DP1 and DP2 models are better than the DP0 and the diffusion calculation (PIJ=1) at all burnups. The thermal flux gradient in coolant region is predicted more accurately by full transport theory simulation (PIJ=2) as compared to hybrid method of transport and diffusion calculation (PIJ=1). This may explain the relatively larger deviation in xenon and samarium load calculated using PIJ=1 option.

3.6.4.2 Fuel Temperature Effect

Table 3.13 gives the comparison of fuel temperature effect or Doppler load obtained using four models with BM values for UGD and MOXGD FAs. The Doppler load is calculated corresponding to a change in fuel temperature from 1027K to 575K. It is observed that the Doppler load calculated by VISWAM models increase less with burnup compared to the change in BM values. For UGD fuel it is calculated to be higher than the BM value while at higher burnup they are lower than the BM value. At zero burnup, a maximum deviation of +1.85 mk from BM value of 9.8 mk is seen for DP0 model for UGD FA. The minimum difference of +1.27 mk is noted for DP2 method for this case. At 20 MWD/KgHM the deviations are the least and are less than –0.6 mk. At 40 MWD/KgHM, the maximum deviation is seen to be –2.8 mk w.r.t. BM value of 15.63 mk for DP2 method. The closest matching is seen for DP0 model (–1.54 mk). For MOXGD FA, the comparison is better at 0 & 20 MWD/KgHM. The maximum difference of 0.22 mk is seen for PIJ=1 at zero burnup w.r.t. BM value of 12.18 mk. At 20 MWD/KgHM the maximum deviation is –0.98 mk for DP2 model w.r.t. BM value of 13.84 mk. At 40 MWD/KgHM this deviation increases further to –3.16 mk for DP2 calculation w.r.t. BM value of 15.98 mk. The relatively large deviation in the Doppler load can be related to the resonance treatment in the multiple fuel rings. This will be discussed further along with the results of radial distribution of ^{239}Pu in Gd fuel pin later in Section 3.6.5.3.

3.6.4.3 Soluble Boron Effect

Table 3.14 gives the effect of soluble boron or boron load for UGD and MOXGD FAs. The boron load corresponds to the change in boron concentration of 600 ppm between isothermal states S3 and S4. Both for LEU and MOX assemblies, the boron load obtained using four methods are over–predicted compared to the BM values. For UGD FA, at zero burnup, the

maximum deviation of –1.79 mk is noted for PIJ=1 method w.r.t. BM value of –40.27 mk. At 40 MWD/KgHM, the maximum difference becomes –2.55 mk for DP2 method w.r.t. BM value of –51.37 mk. For MOXGD FA, the maximum deviation is seen for DP2 model. It is –1.18 mk at zero burnup w.r.t. BM value of –23.2 mk and –2.45 mk at 40 MWD/KgHM w.r.t. BM value of –42.64 mk. The minimum deviation in boron load is obtained with DP0 model at all the three burnup points for both the FA variants.

3.6.4.4 Isothermal Temperature Effect

The isothermal temperature load is obtained for an isothermal temperature change from 575K in S4 state to 300K in S5 state. Table 3.15 gives the comparison of isothermal temperature load obtained using VISWAM with BM values. The isothermal temperature load is over predicted by PIJ=1 and DP0 models for both LEU and MOX cases. DP1/DP2 model shows much less over–prediction. For UGD FA, at zero burnup, the maximum difference of –6.21 mk is seen for PIJ=1 and the minimum difference of –0.41 mk is seen for DP2 method w.r.t. BM value of –41.69 mk. At 40 MWD/KgHM, these values become –7.56 mk and –2.29 mk respectively w.r.t. BM value of –50.36 mk. For MOXGD FA, the same trend as for UGD FA is observed. The maximum and minimum deviations in MOXGD FA are seen as –4.81 mk & +0.08 mk respectively at zero burnup for PIJ=1 and DP2 models w.r.t. BM value of –47.96 mk. At 40 MWD/KgHM burnup, these values change to –8.15 mk and –2.16 mk respectively w.r.t. BM value of –52.73 mk. The relatively larger deviations are also seen for DP0 model. The DP1/DP2 models take care of the flux anisotropy near strong absorber like Gd or near water GTs more accurately. Hence the thermal flux gradients near Gd and in coolant regions are accurately calculated using these models.

Table 3.12 –Equilibrium Xe & Sm Poisoning Effect

Burnup (MWD/KgHM)	UGD Fuel Assembly														
	k_∞ in Operating poisoned state (S1)					k_∞ in Operating non-poisoned state (S2)					Equilibrium Xe+Sm Load (mk)				
	PIJ=2			PIJ=1	BM Mean	PIJ =2			PIJ =1	BM Mean	PIJ =2			PIJ =1	BM Mean
	DP0	DP1	DP2			DP0	DP1	DP2			DP0	DP1	DP2		
0	1.12289	1.12808	1.12876	1.12591	1.13500	1.16297	1.16826	1.16898	1.16588	1.17540	–30.69	–30.49	–30.48	–30.45	–30.28
20	1.03567	1.04191	1.04263	1.03033	1.04110	1.07552	1.08210	1.08287	1.07077	1.08070	–35.78	–35.65	–35.64	–36.66	–35.20
40	0.90533	0.90721	0.90741	0.90189	0.90650	0.93840	0.94033	0.94053	0.93582	0.93940	–38.93	–38.82	–38.81	–40.20	–38.63
MOXGD Fuel Assembly															
0	1.14900	1.15703	1.15809	1.14726	1.15660	1.18325	1.19065	1.19178	1.18103	1.18990	–25.19	–24.40	–24.41	–24.92	–24.20
20	1.01314	1.01943	1.02015	1.00748	1.01600	1.04738	1.05411	1.04599	1.04250	1.05040	–32.27	–32.27	–32.28	–33.34	–32.23
40	0.90059	0.90157	0.90163	0.89608	0.90150	0.93152	0.93260	0.92453	0.92784	0.93230	–36.87	–36.91	–36.91	–38.20	–36.65

Table 3.13 –Fuel Temperature Reactivity Effect

Burnup (MWD/KgHM)	UGD Fuel Assembly														
	k_∞ in Hot State (S3)					k_∞ in Operating non-poisoned state (S2)					Doppler Load (mk)				
	PIJ=2			PIJ=1	BM Mean	PIJ =2			PIJ =1	BM Mean	PIJ =2			PIJ =1	BM Mean
	DP0	DP1	DP2			DP0	DP1	DP2			DP0	DP1	DP2		
0	1.17894	1.18367	1.18431	1.18161	1.18910	1.16297	1.16826	1.16898	1.16588	1.17540	11.65	11.14	11.07	11.42	9.80
20	1.09090	1.09674	1.09742	1.08531	1.09590	1.07552	1.08210	1.08287	1.07077	1.08070	13.11	12.34	12.24	12.51	12.83
40	0.95097	0.95195	0.95202	0.94760	0.95340	0.93840	0.94033	0.94053	0.93582	0.93940	14.09	12.98	12.83	13.28	15.63
	MOXGD Fuel Assembly														
0	1.20059	1.20841	1.20944	1.19859	1.20740	1.20740	1.19065	1.19178	1.18103	1.18990	12.21	12.34	12.25	12.40	12.18
20	1.06294	1.06874	1.06940	1.05702	1.06590	1.06590	1.05411	1.04599	1.04250	1.05040	13.98	12.99	12.86	13.18	13.84
40	0.94403	0.94403	0.94396	0.93948	0.94640	0.94640	0.93260	0.92453	0.92784	0.93230	14.23	12.98	12.82	13.35	15.98

Table 3.14 – Soluble Boron Effect

Burnup (MWD/KgHM)	UGD Fuel Assembly														
	k_∞ in Hot State (S3)					k_∞ in Hot State without boric acid(S4)					Boron Load (mk)				
	PIJ=2			PIJ=1	BM Mean	PIJ =2			PIJ =1	BM Mean	PIJ =2			PIJ =1	BM Mean
	DP0	DP1	DP2			DP0	DP1	DP2			DP0	DP1	DP2		
0	1.17894	1.18367	1.18431	1.18161	1.18910	1.23873	1.24447	1.24536	1.24340	1.24890	–40.94	–41.28	–41.39	–42.06	–40.27
20	1.09090	1.09674	1.09742	1.08531	1.09590	1.14575	1.15352	1.15455	1.14060	1.15070	–43.88	–44.88	–45.09	–44.66	–43.46
40	0.95097	0.95195	0.95202	0.94760	0.95340	1.00003	1.00310	1.00353	0.99687	1.00250	–51.59	–53.57	–53.92	–52.16	–51.37
	MOXGD Fuel Assembly														
0	1.20059	1.20841	1.20944	1.19859	1.20740	1.23564	1.24487	1.24619	1.23452	1.24220	–23.63	–24.24	–24.38	–24.28	–23.20
20	1.06294	1.06874	1.06940	1.05702	1.06590	1.10140	1.10897	1.10997	1.09600	1.10420	–32.85	–33.94	–34.18	–33.65	–32.54
40	0.94403	0.94403	0.94396	0.93948	0.94640	0.98372	0.98564	0.98592	0.97949	0.98620	–42.74	–44.72	–45.09	–43.48	–42.64

Table 3.15 – Isothermal Temperature Effect

Burnup (MWD/KgHM)	UGD Fuel Assembly														
	k_∞ in Hot State without boric acid(S4)					k_∞ in Cold State without boric acid(S5)					Isothermal Temperature Load (mk)				
	PIJ=2			PIJ=1	BM Mean	PIJ =2			PIJ =1	BM Mean	PIJ =2			PIJ =1	BM Mean
	DP0	DP1	DP2			DP0	DP1	DP2			DP0	DP1	DP2		
0	1.23873	1.24447	1.24536	1.24340	1.24890	1.30878	1.31338	1.31426	1.32214	1.31750	–43.21	–42.16	–42.10	–47.90	–41.69
20	1.14575	1.15352	1.15455	1.14060	1.15070	1.21796	1.22326	1.22410	1.21369	1.21790	–51.75	–49.42	–49.21	–52.80	–47.95
40	1.00003	1.00310	1.00353	0.99687	1.00250	1.06001	1.05941	1.05951	1.05795	1.05580	–56.58	–52.99	–52.65	–57.92	–50.36
	MOXGD Fuel Assembly														
0	1.23564	1.24487	1.24619	1.23452	1.24220	1.31649	1.32408	1.32527	1.32055	1.31940	–49.70	–48.06	–47.88	–52.77	–47.96
20	1.10140	1.10897	1.10997	1.09600	1.10420	1.17722	1.18167	1.18244	1.17216	1.18140	–58.48	–55.48	–55.22	–59.28	-54.28
40	0.98372	0.98564	0.98592	0.97949	0.98620	1.04503	1.04248	1.04233	1.04160	1.05300	–59.64	–55.32	–54.89	–60.88	-52.73

3.6.5 Comparison of Fuel Isotopic Composition with Burnup

The isotopic composition of fuel nuclides ^{235}U, ^{236}U, ^{238}U, ^{239}Pu, ^{240}Pu, ^{241}Pu, ^{242}Pu, fission products ^{135}Xe & ^{149}Sm and burnable poison isotopes ^{155}Gd & ^{157}Gd are compared with BM values and other evaluations in benchmark report. These isotopic compositions were requested as assembly averaged compositions and compositions in the corner cell 1 & gadolinium cell 24 in Fig. 3.14.

3.6.5.1 Assembly Average Isotopic Composition

Figs 3.19 to 3.29 give the assembly averaged isotopic compositions of the above eleven nuclides for UGD and MOXGD FAs. The plots include the four VISWAM models, the BM mean and five other evaluations of MCU, TVS–M, WIMS8A, HELIOS and MULTICELL. There is good agreement between all the evaluations for main fuel isotopes of ^{235}U, ^{238}U & ^{239}Pu. Hence they are seen nearly as a single graph. From the figures it is seen that there is a wider spread in the calculated number densities of fuel isotopes ^{236}U, ^{240}Pu, ^{241}Pu & ^{242}Pu as evaluated by various submission groups for both UGD and MOXGD FAs. The isotopic compositions obtained using four methods of VISWAM lie within the band of spread of all submissions for UGD and MOXGD FAs.

In UGD case, the isotopic compositions of ^{135}Xe obtained using four methods are similar up to about 10 MWD/KgHM but differ subsequently. Beyond 10 MWD/KgHM, the results of DP1/DP2 are closer to the BM values. Higher concentrations are seen for DP0/PIJ=1 method compared to the BM values. For MOXGD FA, the difference between DP1/DP2 and other models starts from zero burnup and continue till 40 MWD/KgHM. In this case, the BM results are closer to DP0/PIJ=1 values.

As seen from Fig. 3.27, the ^{149}Sm concentrations show larger spread for evaluations by various groups. Equilibrium concentration of ^{149}Sm at zero burnup is considered only in TVS–M and HELIOS. Since in VISWAM code we have considered equilibrium ^{149}Sm at zero burnup, the mean of these two codes is used for benchmark comparison purpose. The results obtained with DP1/DP2 model always predict lower concentrations compared to DP0/PIJ=1 method. The BM values are seen to be closely matching with DP1/DP2 values.

The calculated concentrations of ^{155}Gd & ^{157}Gd from PIJ=2 are seen higher compared to those calculated from PIJ=1 method with burnup. This observation is true for both UGD and MOXGD FAs. This indicates faster depletion of Gd in PIJ=1 model. This also results in shifting of peak k_∞ to earlier burnup (Fig.3.17).

3.6.5.2 Isotopic Composition in Corner and Gadolinium Pins

The benchmark required the isotopic compositions of various nuclides in two individual cells 1 & 24 (see Fig. 3.14). Cell 1 is a corner pin which is UO2 pin in UGD FA and MOX pin MOXGD FA. Cell 24 is gadolinium pin in both the FA types. Figs. 3.30 to 3.38 give the isotopic composition of various nuclides in cell 1 for UGD and MOXGD FAs. Figs. 3.39 to 3.49 give the isotopic composition of various nuclides in cell 24 for UGD and MOXGD FAs. The observations described in previous paragraph are, in general, true for the Figs 3.30 to 3.49. The isotopic compositions of VISWAM generally agree with BM values and lie within the band of variation of other evaluations.

3.6.5.3 Radial Variation of Isotopic Composition

The radial variation of isotopic composition was studied for cell 24 with Gd. The fuel region is divided into five rings of equal volume. Figs. 3.50 & 3.51 give the variation of isotopic

composition of ^{235}U & ^{239}Pu with fuel ring radius at 40 MWD/KgHM for UGD and MOXGD FAs. Figs. 3.52 & 3.53 give the variation of isotopic composition of ^{155}Gd & ^{157}Gd with fuel ring radius at 2 MWD/KgHM for the two FA variants. The VISWAM values show a good agreement with benchmark values for Gd isotopes. For ^{235}U, the values predicted by VISWAM are lower compared to BM value and other evaluations for UGD FA, whereas, the values are higher for MOXGD FA. For ^{239}Pu, no radial variation is observed. The reason for this was scrutinized and it was observed that radial shape is present at early stages of burnup. This is seen in Fig 3.51a, where the ^{239}Pu concentration is plotted at 5 MWD/KgHM. However, as burnup progresses, the ^{239}Pu in the outer ring, though produced more, depletes also faster compared to inner rings. Hence at 40 MWD/KgHM, the ^{239}Pu attains nearly equal value in all the rings in VISWAM models. The BM values however show an enhanced level of ^{239}Pu in the outer ring even at higher burnup. It may be stated here that in VISWAM code there is no provision to distinguish the background cross section in the five fuel rings, i.e., the ^{238}U capture cross section is nearly the same in all five fuel rings for resonance groups. If one can consider the inner rings to be shielded by the outer ones, it may be possible to prescribe higher resonance capture cross section for the outer rings [52]. This could increase the ^{239}Pu formation in the outer ring. It is felt that such improved resonance treatment would also influence the Doppler load calculation and can help in better agreement with BM values for Doppler load.

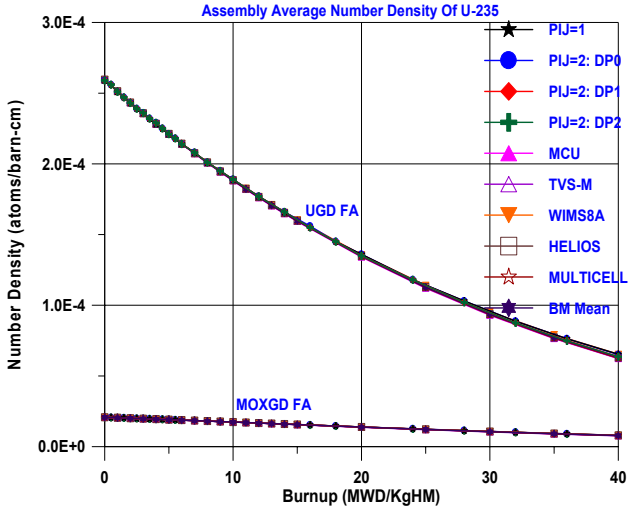

Fig 3.19 Assembly Average number density of ^{235}U with burnup

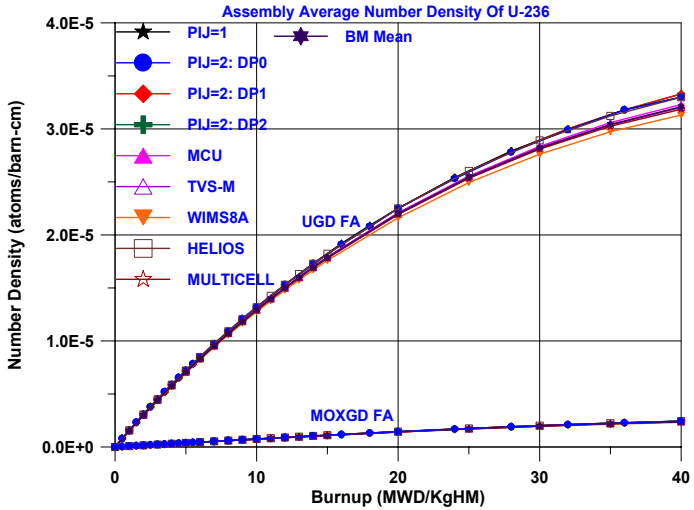

Fig 3.20 Assembly Average number density of ^{236}U with burnup

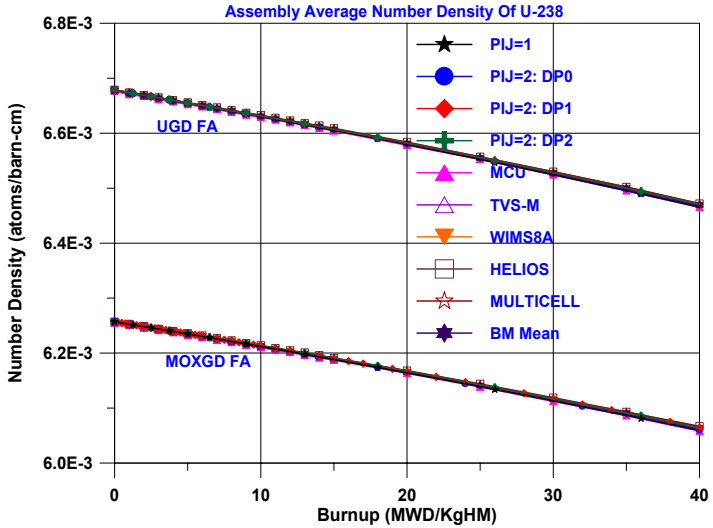

Fig 3.21 Assembly Average number density of ^{238}U with burnup

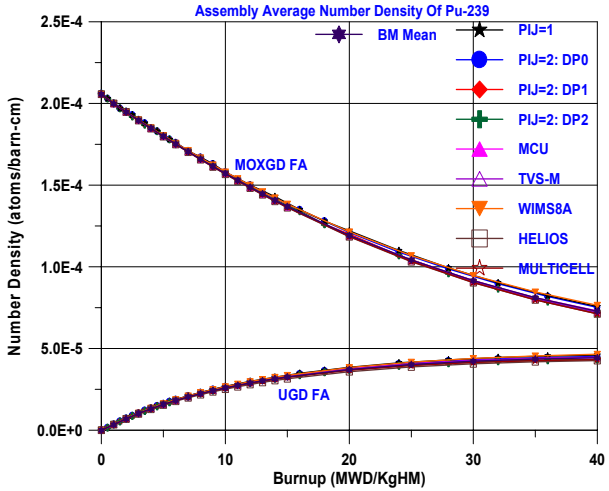

Fig 3.22 Assembly Average number density of ^{239}Pu with burnup

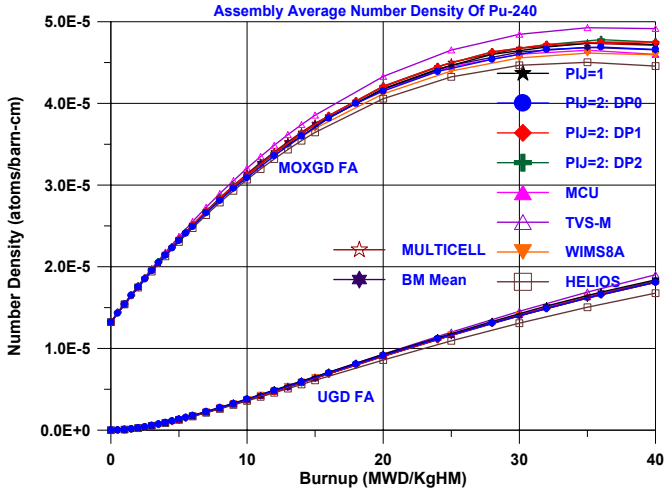

Fig 3.23 Assembly Average number density of ^{240}Pu with burnup

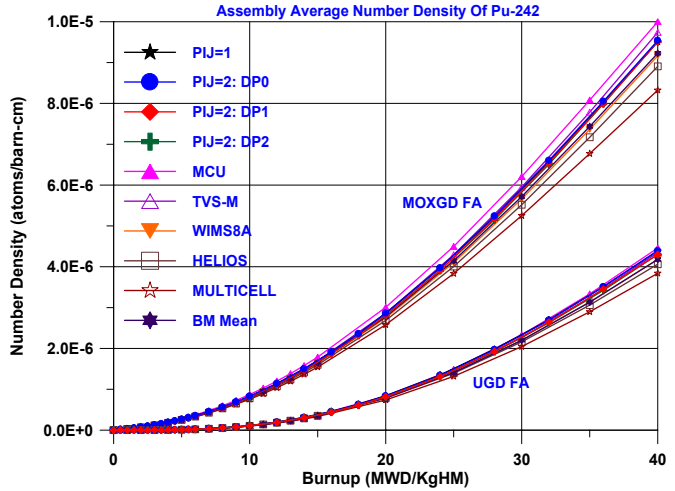

Fig 3.25 Assembly Average number density of ^{242}Pu with burnup

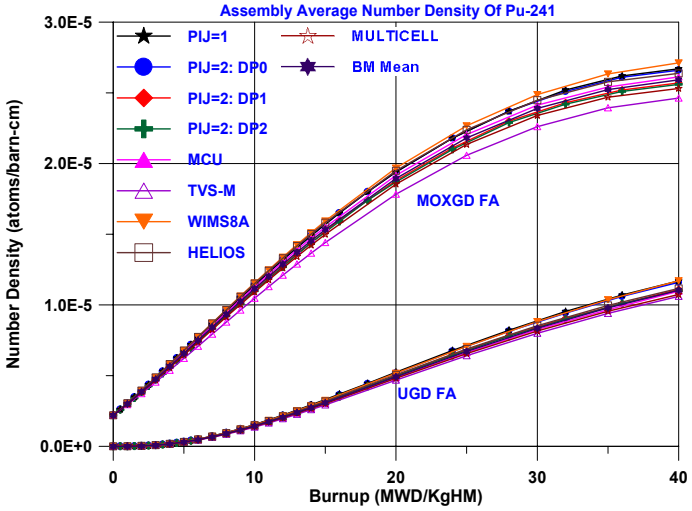

Fig 3.24 Assembly Average number density of ^{241}Pu with burnup

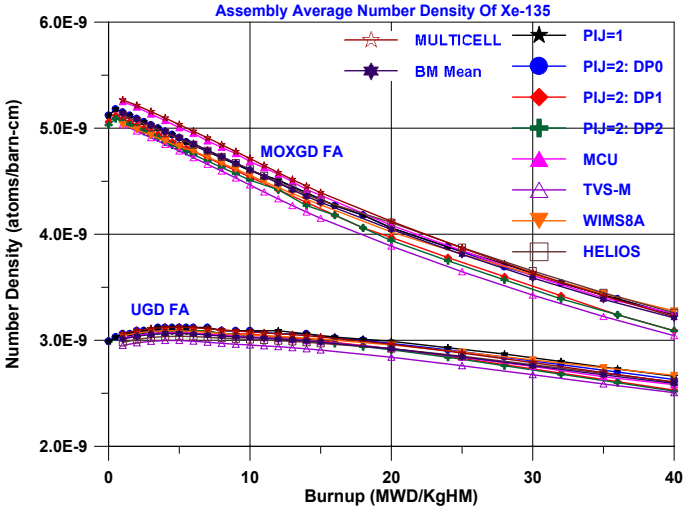

Fig 3.26 Assembly Average number density of ^{135}Xe with burnup

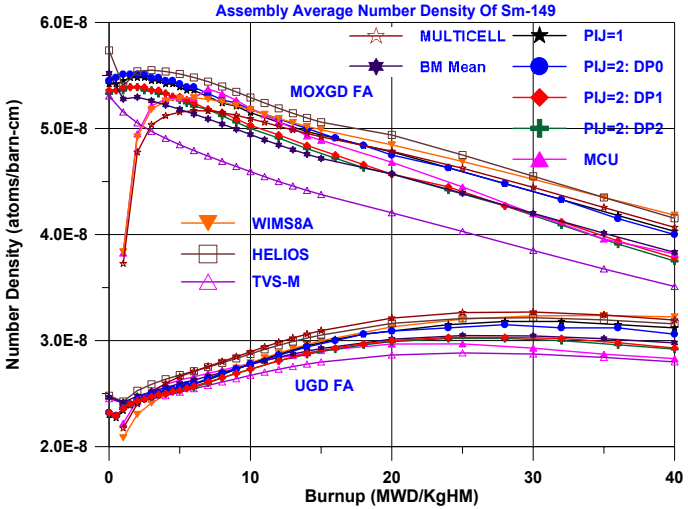

Fig 3.27 Assembly Average number density of ^{149}Sm with burnup

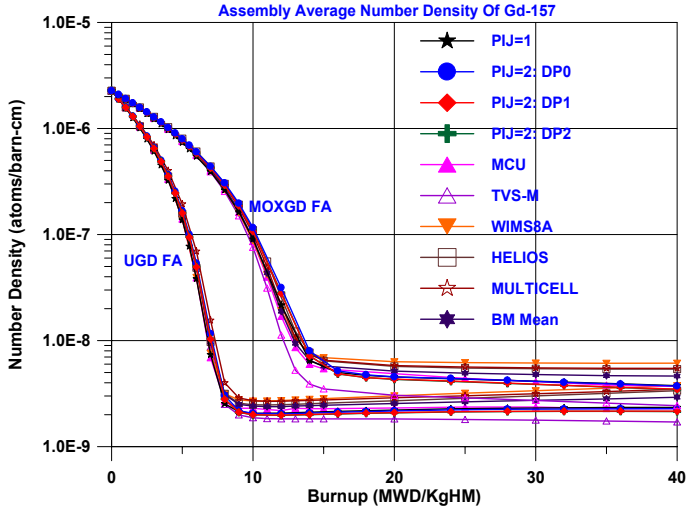

Fig 3.29 Assembly Average number density of ^{157}Gd with burnup

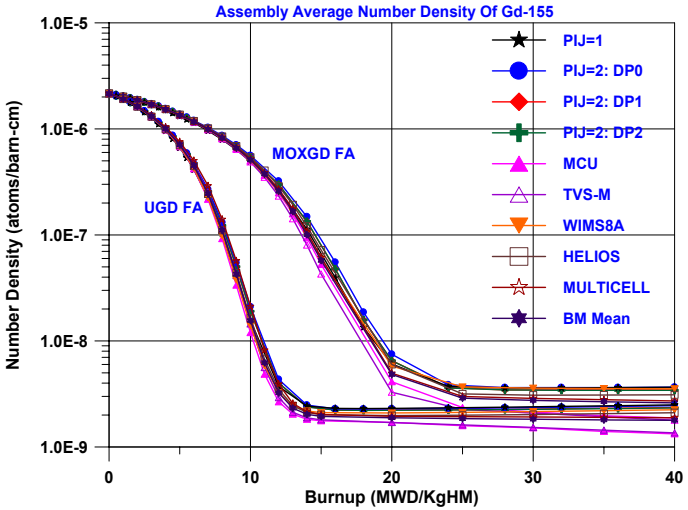

Fig 3.28 Assembly Average number density of ^{155}Gd with burnup

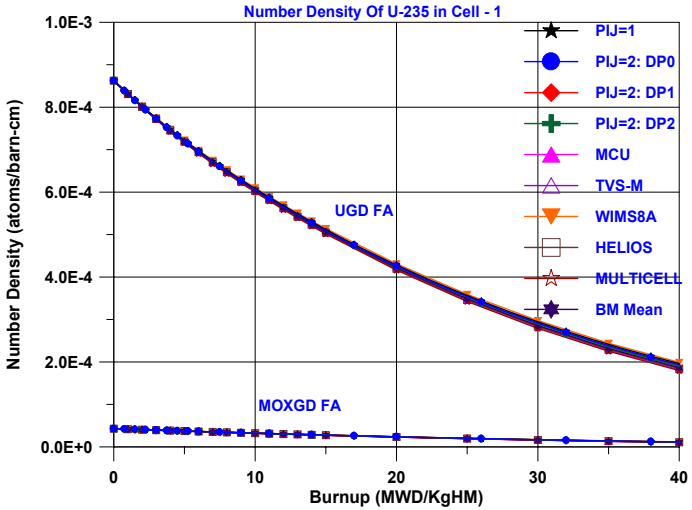

Fig 3.30 ^{235}U Number density with burnup in Cell – 1

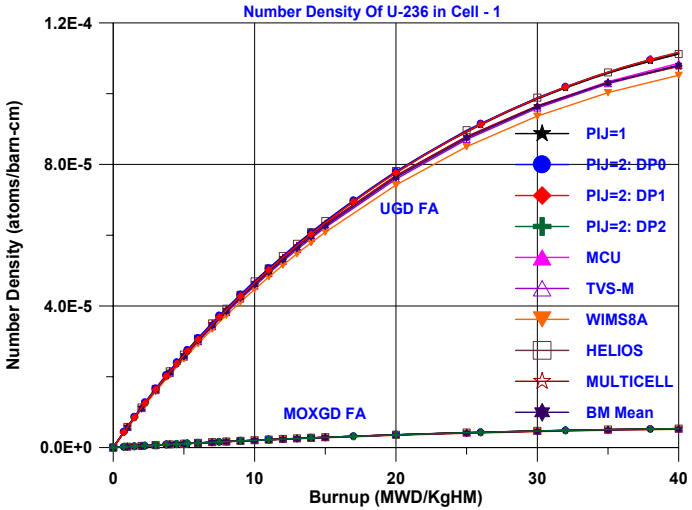

Fig 3.31 ^{236}U Number density with burnup in Cell – 1

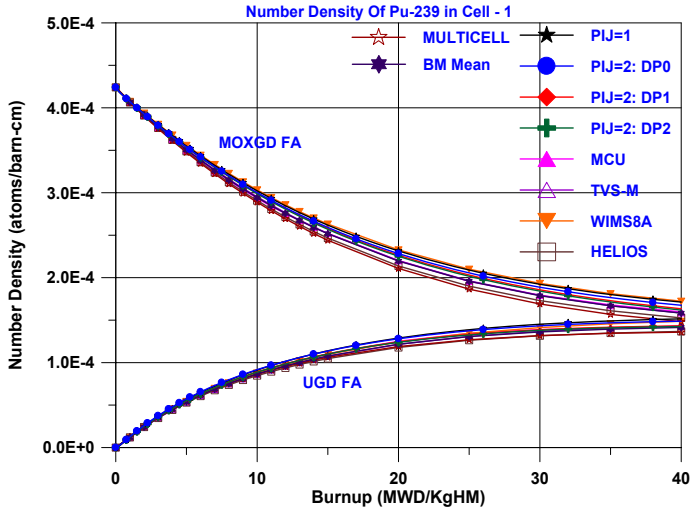

Fig 3.33 ^{239}Pu Number density with burnup in Cell – 1

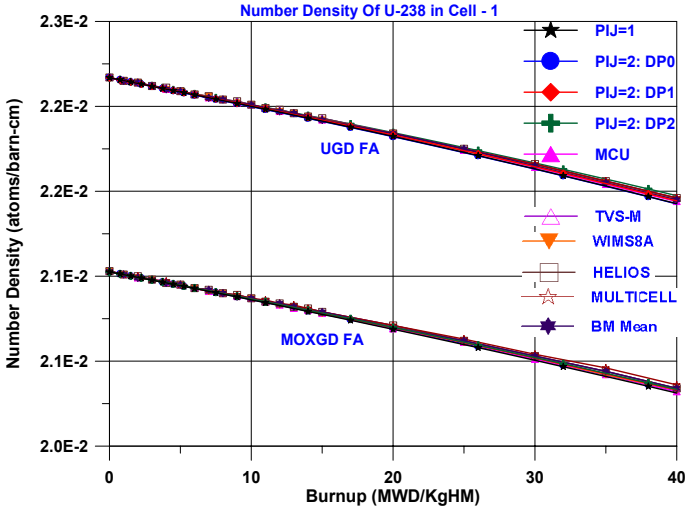

Fig 3.32 ^{238}U Number density with burnup in Cell – 1

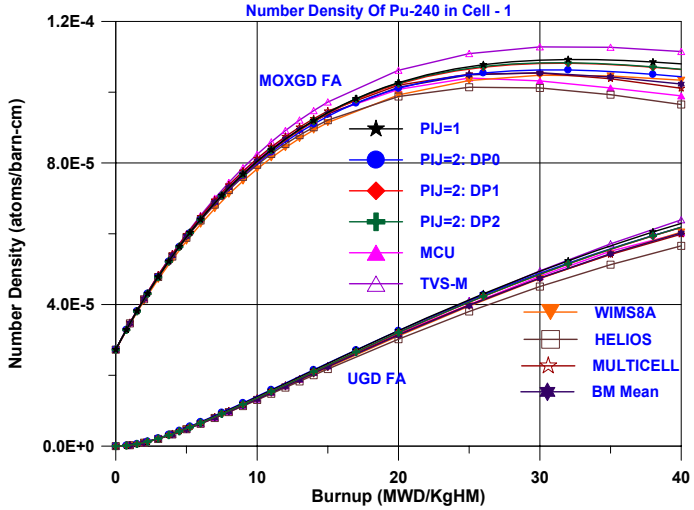

Fig 3.34 ^{240}Pu Number density with burnup in Cell – 1

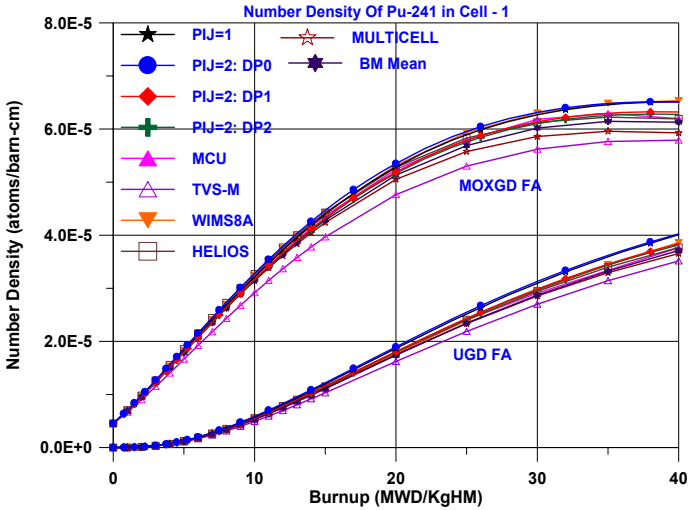

Fig 3.35 ^{241}Pu Number density with burnup in Cell – 1

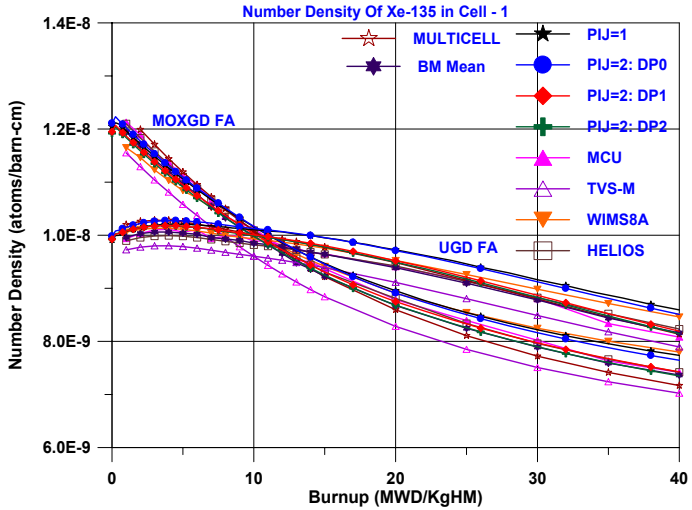

Fig 3.37 ^{135}Xe Number density with burnup in Cell – 1

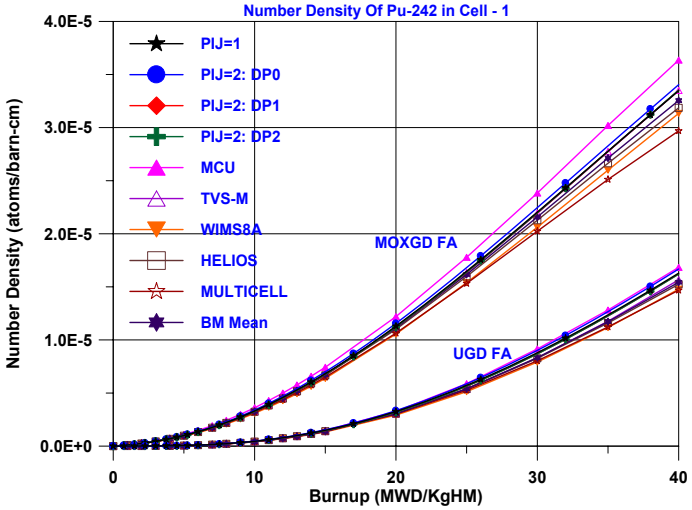

Fig 3.36 ^{242}Pu Number density with burnup in Cell – 1

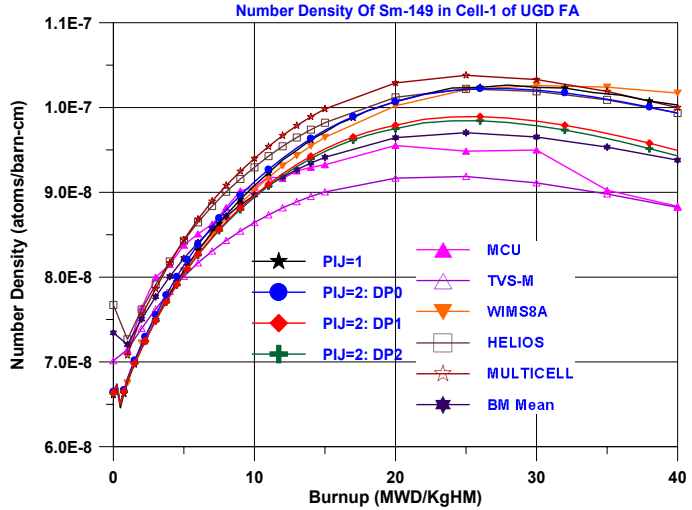

Fig 3.38a ^{149}Sm Number density with burnup in Cell – 1

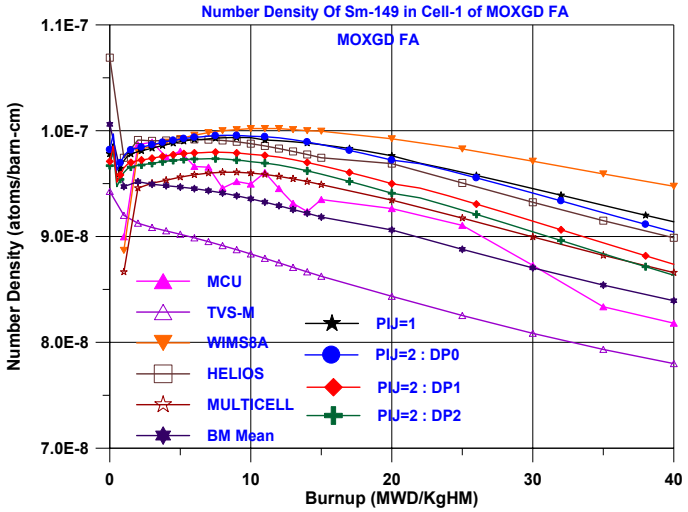

Fig 3.38b ^{149}Sm Number density with burnup in Cell – 1

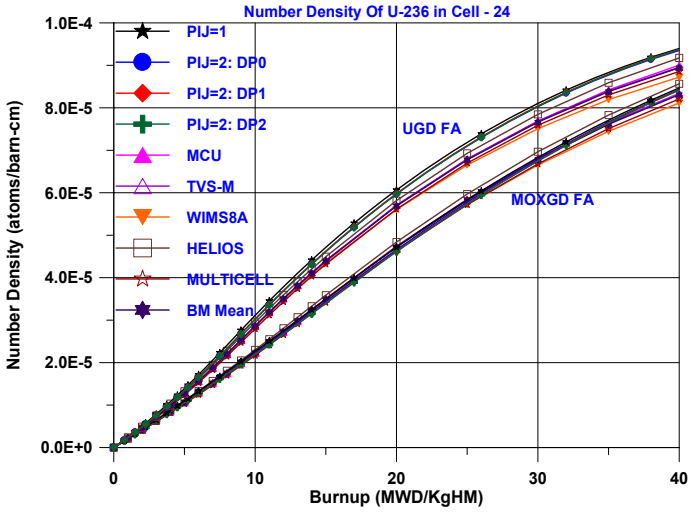

Fig 3.40 ^{236}U Number density with burnup in Cell – 24

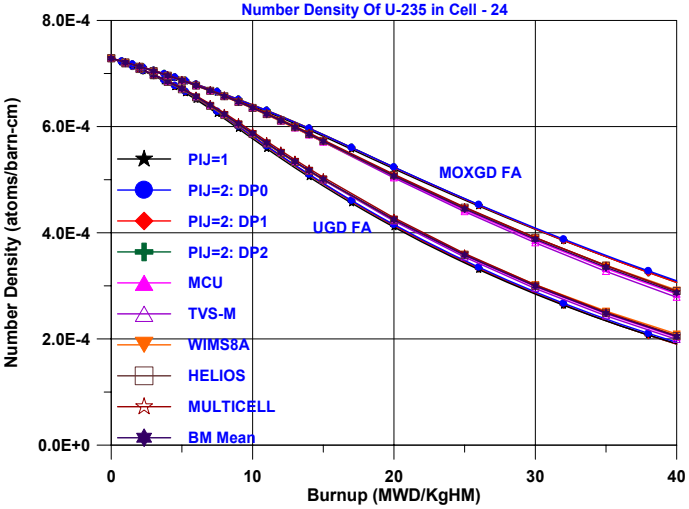

Fig 3.39 ^{235}U Number density with burnup in Cell – 24

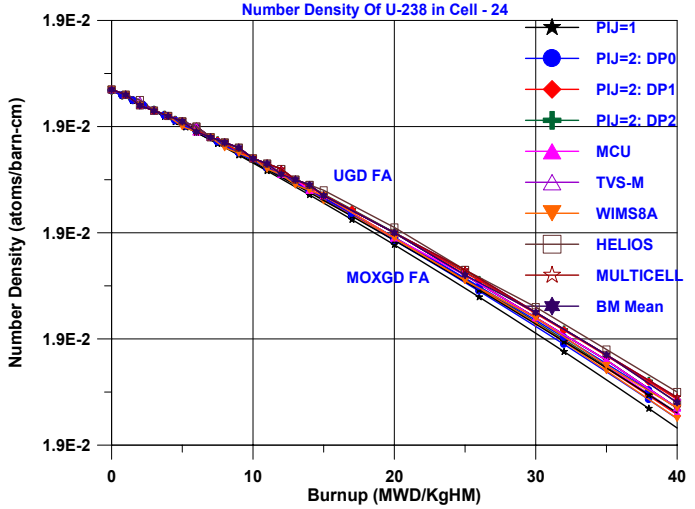

Fig 3.41 ^{238}U Number density with burnup in Cell – 24

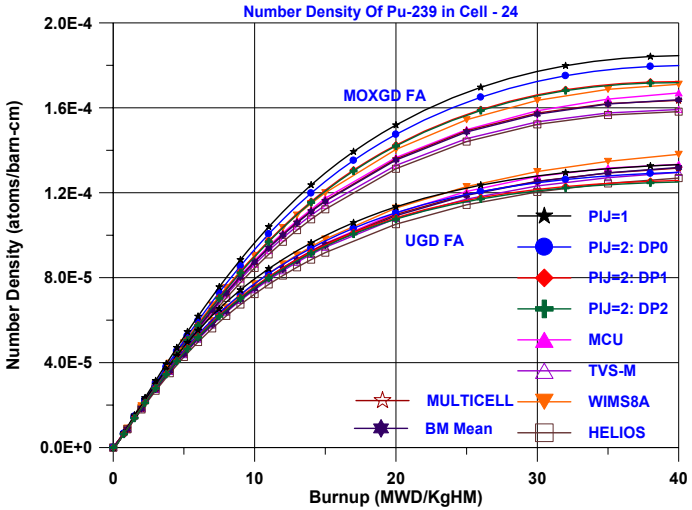

Fig 3.42 ^{239}Pu Number density with burnup in Cell – 24

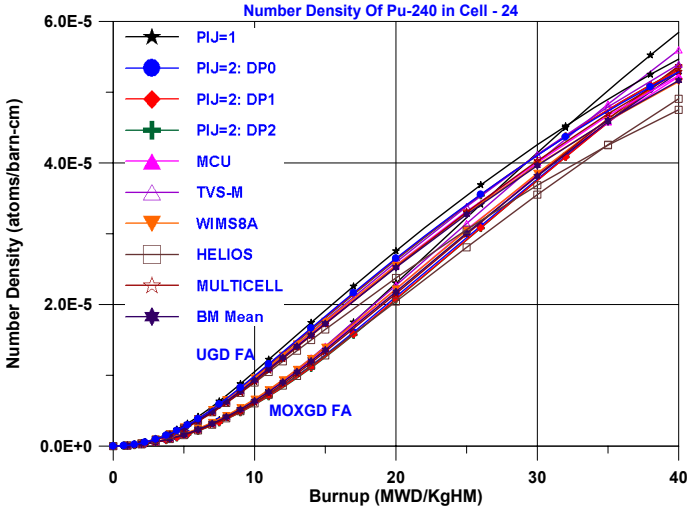

Fig 3.43 ^{240}Pu Number density with burnup in Cell – 24

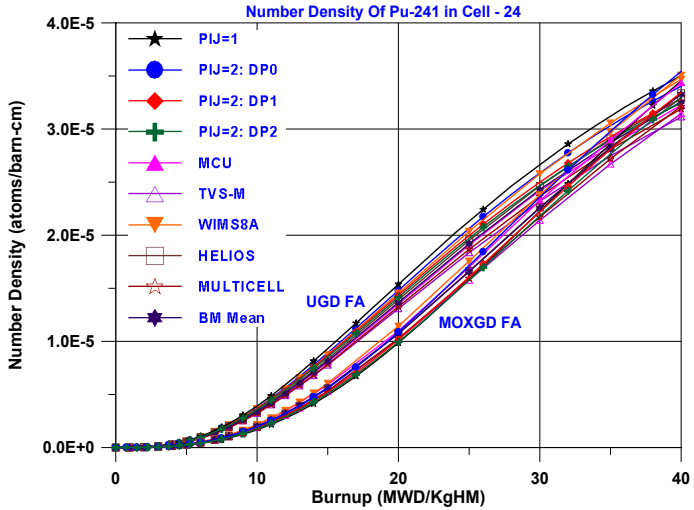

Fig 3.44 ^{241}Pu Number density with burnup in Cell – 24

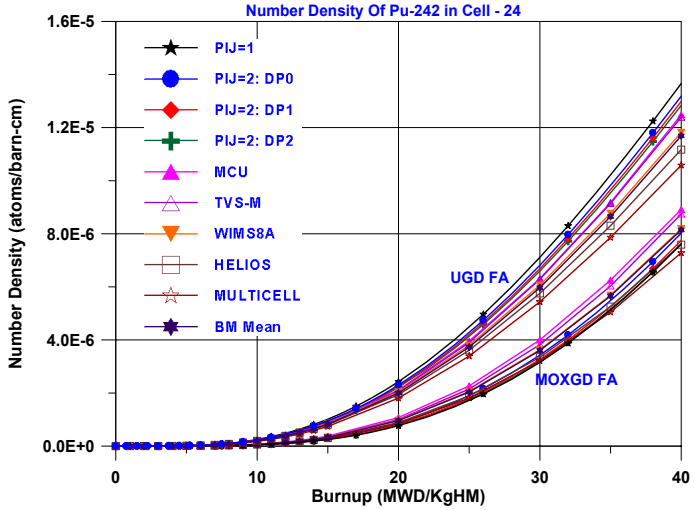

Fig 3.45 ^{242}Pu Number density with burnup in Cell – 24

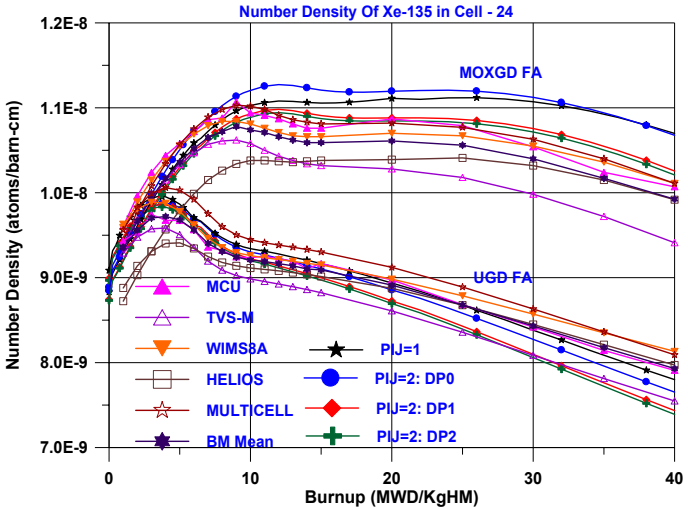

Fig 3.46 ^{135}Xe Number density with burnup in Cell – 24

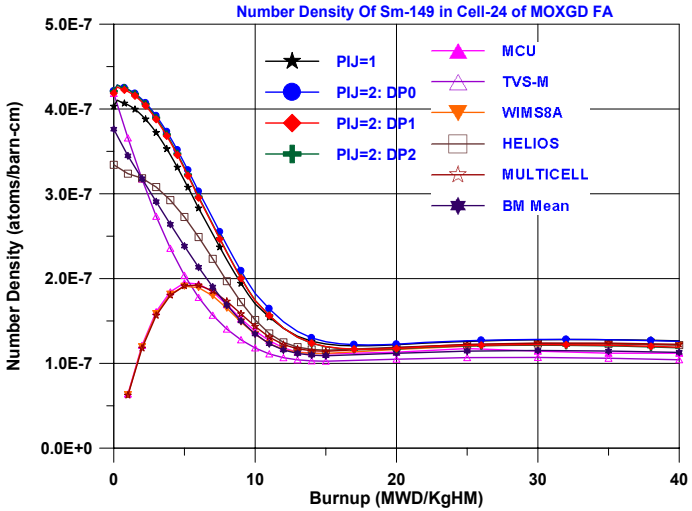

Fig 3.47b ^{149}Sm Number density with burnup in Cell – 24

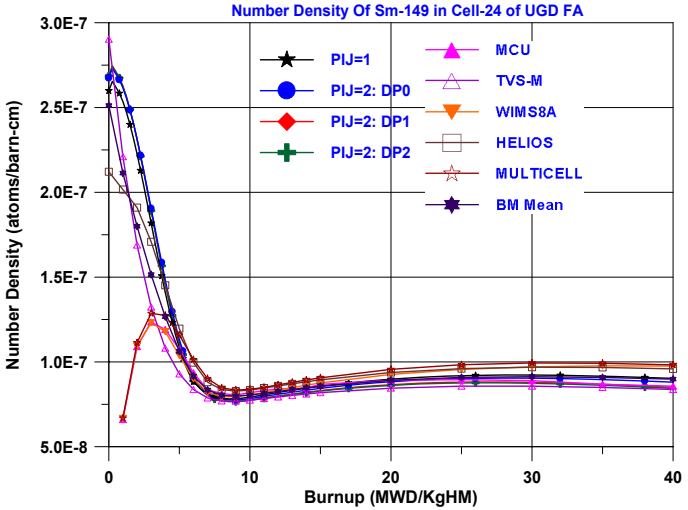

Fig 3.47a ^{149}Sm Number density with burnup in Cell – 24

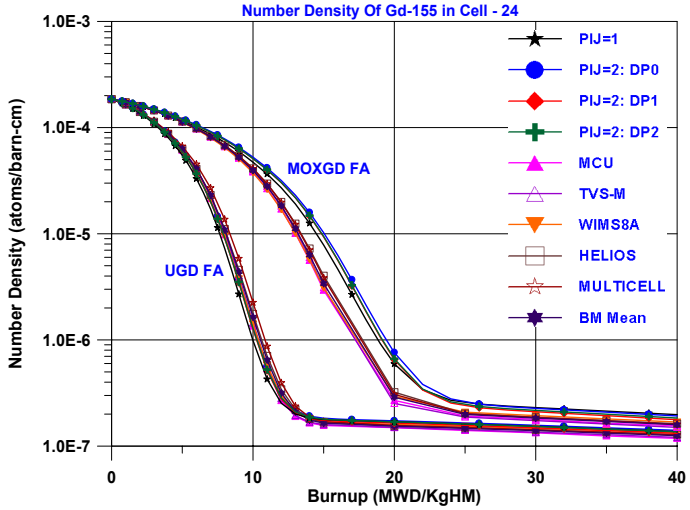

Fig 3.48 ^{155}Gd Number density with burnup in Cell – 24

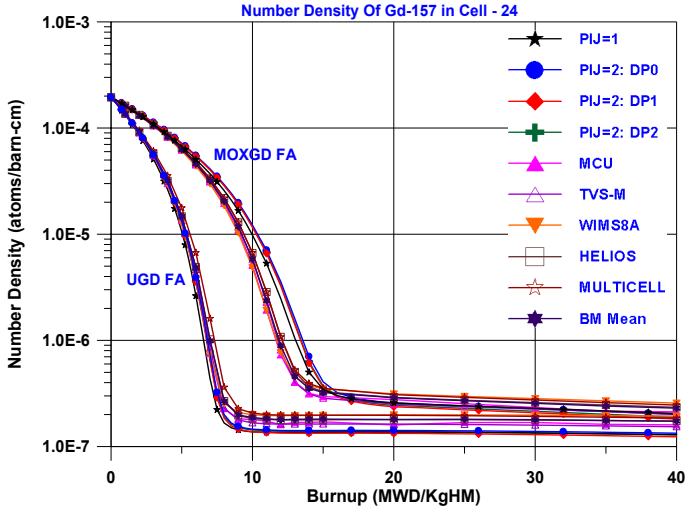

Fig 3.49 ^{157}Gd Number density with burnup in Cell – 24

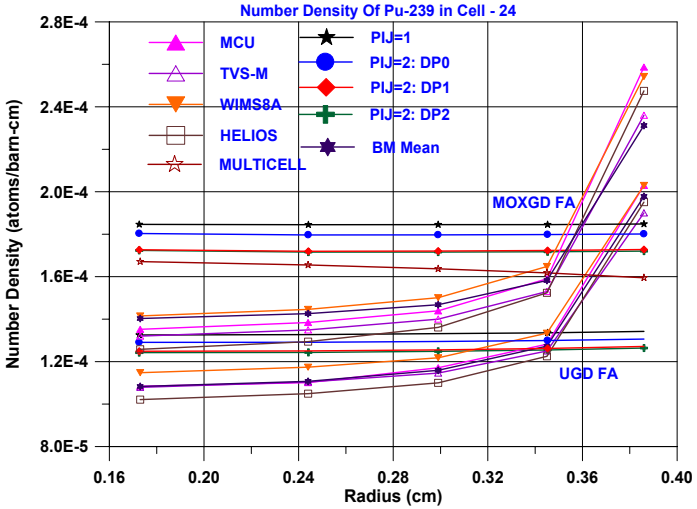

Fig 3.51 ^{239}Pu Number density with Radius in Cell – 24 at 40 MWD/KgHM

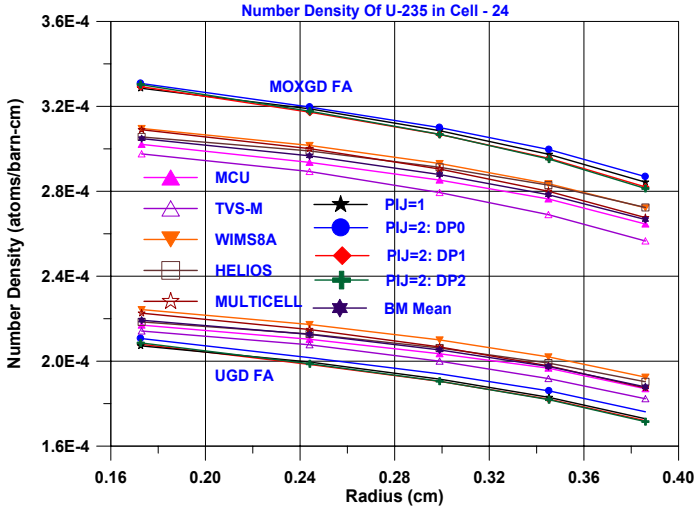

Fig 3.50 ^{235}U Number density with Radius in Cell – 24 at 40 MWD/KgHM

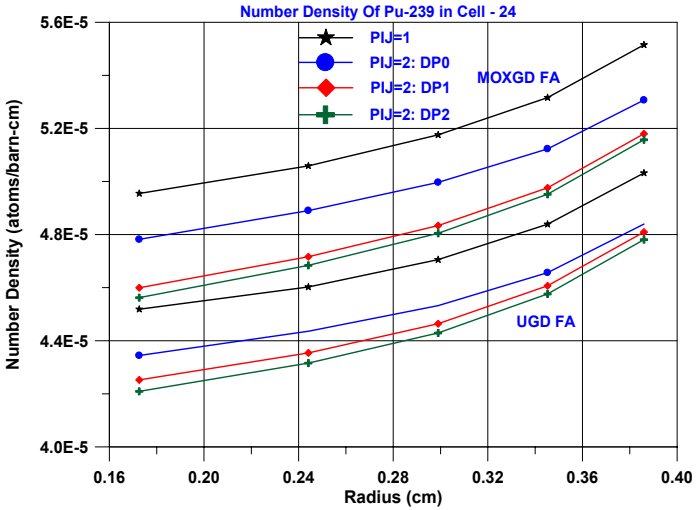

Fig 3.51a ^{239}Pu Number density with Radius in Cell – 24 at 5 MWD/KgHM

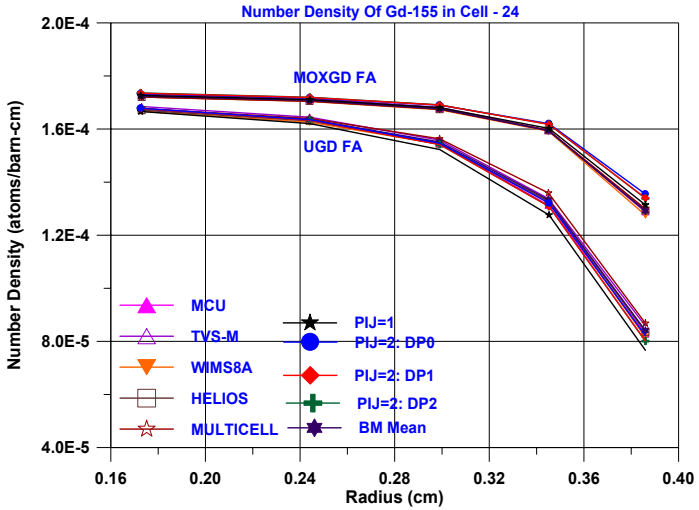

Fig 3.52 ^{155}Gd Number density with Radius in Cell – 24 at 2 MWD/KgHM

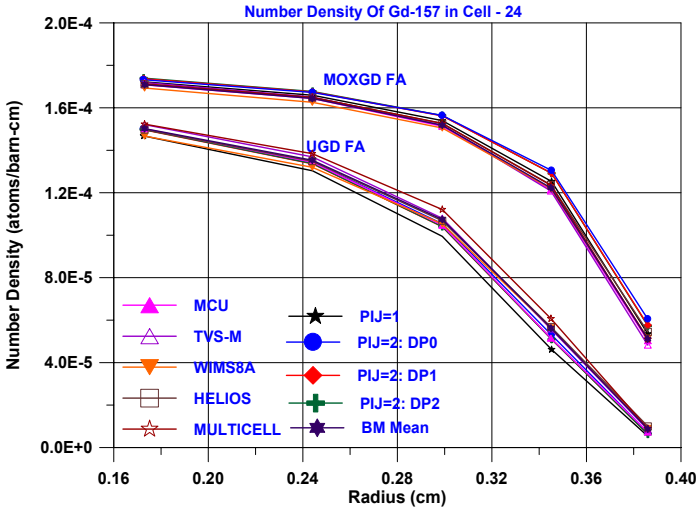

Fig 3.53 ^{157}Gd Number density with Radius in Cell – 24 at 2 MWD/KgHM

3.6.6 Fission Density Distribution

The fission density distribution for S1 state with burnup is given in Tables 3.16 & 3.18 for UGD and MOXGD FAs respectively. Tables 3.17 & 3.19 give the fission density distribution with burn up for states S2 to S5 for the two FA variants. In the benchmark, the pin with maximum r.m.s. deviation was selected and the fission density in this pin was compared at each burnup. We have taken the same pin location for comparison. In these tables, the values obtained using VISWAM–DP2 model alone are compared with different evaluations and BM values. As seen from Tables 3.16 & 3.18, the comparison for fission density distribution is very good. The maximum deviation w.r.t. BM values for UGD FA is 2.03% (at 2 MWD/KgHM) and –2.71% (at 12 MWD/KgHM) for MOXGD FA in S1 state. For UGD FA at the beginning of burnup, the pin with maximum deviation is Gd pin and is located at pin location 24 (Fig. 3.14). At the end of burnup, pin with maximum deviation is uranium pin number 1 at the corner of the FA. For MOXGD FA at the beginning of burnup, pin with maximum deviation is pin number 1 at the corner of the assembly and at the end of burnup pin with maximum deviation is Gd pin number 35. For states S2 to S5, the comparison of fission density distribution with BM and other evaluations is very good. For UGD FA, the maximum deviation of 1.85% w.r.t. BM is observed in S2 state at zero burnup. The maximum deviation for MOXGD FA is –2.62% for S5 state at zero burnup.

The detailed pin by pin fission density distribution in $1/6^{th}$ fuel assembly, for S2 to S5 states at zero burnup, is compared with BM values. The BM values are obtained using standard arithmatic mean definition and includes MCNP evaluations also. The pin wise location map of $1/6^{th}$ fuel assembly used for fission density comparison is as shown in Fig. 3.14. The deviations in fission density calculated using four methods of VISWAM w.r.t. the BM values are given in

Figs. 3.54 & 3.55 for S2 state at zero burnup for UGD and MOXGD FAs respectively. It is observed that the maximum deviation from BM values is the least for the results obtained using DP2 model. Therefore only DP2 results are chosen for further comparison. Figs. 3.56 to 3.59 give the comparison of VISWAM fission density distribution (obtained using DP2 model) with BM for states S2 to S5 at zero burnup for UGD FA. A maximum relative deviation of 1.2% is seen for states S2 to S3. For S4 state, the maximum relative deviation of 2.07% is observed. Figs. 3.60 to 3.63 give the comparison of VISWAM fission density distribution (obtained using DP2 model) with BM for states S2 to S5 at zero burnup for MOXGD FA. The maximum relative deviation of –3.09% is seen for S5 state. This deviation is seen in pin 56 in S5 state. For states S2 to S4, the maximum relative deviation is seen of the order of 2.50%. The relatively larger deviation pins are seen on the periphery of the MOXGD FA. The fission density distribution shows a satisfactory comparison, both for UGD & MOXGD FAs, in states S2 to S5.

Table 3.16 –Fission rate Distribution in S1 state with Burnup for UGD Fuel Assembly

		Burnup (MWD/KgHM)										
		0	2	4	6	8	10	12	14	15	20	40
Mean Value	Maximal R.M.S.	1.91	2.23	2.04	1.95	1.35	0.91	0.91	1.00	0.87	0.85	1.26
	Pin N	63	35	24	24	24	1	1	1	1	19	6
	Fission Rate	0.987	0.443	0.560	0.697	0.822	1.052	1.049	1.048	1.046	0.978	0.980
VISWAM	Fission Rate	0.985	0.452	0.570	0.707	0.825	1.054	1.051	1.050	1.050	0.980	0.981
	Deviation from Mean Value	–0.20	2.03	1.79	1.43	0.36	0.19	0.19	0.19	0.38	0.20	0.10
MCU	Fission Rate	1.005	0.441	0.555	0.691	0.819	1.055	1.054	1.058	1.05	0.965	0.959
	Deviation from Mean Value	1.85	–0.38	–0.82	–0.88	–0.41	0.31	0.48	0.94	0.41	–1.29	–2.13
TVS–M	Fission Rate	0.993	0.436	0.552	0.696	0.831	1.046	1.043	1.041	1.04	0.983	0.987
	Deviation from Mean Value	0.63	–1.51	–1.36	–0.16	1.05	–0.54	–0.57	–0.68	–0.55	0.55	0.73
WIMS8A	Fission Rate	0.998	0.457	0.579	0.720	0.837	1.038	1.035	1.033	1.033	0.987	0.990
	Deviation from Mean Value	1.14	3.33	3.52	3.32	1.75	–1.31	–1.33	–1.41	–1.26	0.92	1.01
HELIOS	Fission Rate	0.981	0.447	0.559	0.694	0.815	1.059	1.056	1.054	1.053	0.975	0.979
	Deviation from Mean Value	–0.61	0.93	–0.07	–0.51	–0.91	0.73	0.70	0.58	0.71	–0.28	–0.08
MULTICELL	Fission Rate	0.957	0.432	0.553	0.685	0.810	1.060	1.056	1.054	1.053	0.979	0.985
	Deviation from Mean Value	–3.01	–2.37	–1.27	–1.77	–1.48	0.82	0.71	0.57	0.69	0.11	0.47

Table 3.17 –Fission rate Distribution in S2 to S5 state with Burnup for UGD Fuel Assembly

		Burnup (MWD/KgHM)											
		S2 State			S3 State			S4 State			S5 State		
		0	20	40	0	20	40	0	20	40	0	20	40
Mean Value	Maximal R.M.S.	2.55	0.88	1.17	2.25	1.13	1.39	2.37	0.96	1.36	2.48	1.37	1.8
	Pin N	35	1	6	35	64	6	35	58	6	35	1	6
	Fission Rate	0.324	1.04	0.982	0.323	1.041	0.981	0.312	0.967	0.98	0.22	1.068	0.97
VISWAM	Fission Rate	0.330	1.045	0.982	0.323	1.036	0.980	0.313	0.966	0.989	0.224	1.059	0.976
	Deviation from Mean Value	1.85	0.48	0.00	0.00	–0.48	–0.10	0.32	–0.10	0.92	1.82	–0.84	0.62
MCU	Fission Rate	0.318	1.048	0.963	0.32	1.062	0.958	0.308	0.953	0.957	0.218	1.084	0.943
	Deviation from Mean Value	–1.75	0.77	–1.95	–0.86	2.00	–2.37	–1.38	–1.47	–2.32	–0.96	1.54	–2.82
TVS–M	Fission Rate	0.319	1.032	0.989	0.318	1.037	0.989	0.308	0.972	0.987	0.217	1.07	0.971
	Deviation from Mean Value	–1.44	–0.77	0.70	–1.48	–0.40	0.79	–1.38	0.50	0.75	–1.41	0.23	0.07
WIMS8A	Fission Rate	0.336	1.028	0.992	0.333	1.032	0.992	0.323	0.978	0.991	0.229	1.05	0.985
	Deviation from Mean Value	3.76	–1.13	0.98	3.32	–0.84	1.09	3.52	1.13	1.14	3.82	–1.67	1.53
HELIOS	Fission Rate	0.329	1.047	0.981	0.327	1.038	0.981	0.317	0.966	0.979	0.222	1.078	0.967
	Deviation from Mean Value	1.52	0.63	–0.14	1.21	–0.30	–0.03	1.34	–0.11	–0.04	1.00	1.02	–0.36
MULTICELL	Fission Rate	0.317	1.045	0.986	0.316	1.037	0.986	0.306	0.967	0.984	0.215	1.056	0.986
	Deviation from Mean Value	–2.09	0.50	0.40	–2.19	–0.45	0.52	–2.11	–0.05	0.47	–2.46	–1.13	1.58

Table 3.18 –Fission rate Distribution in S1 state with Burnup for MOXGD Fuel Assembly

		Burnup (MWD/KgHM)										
		0	2	4	6	8	10	12	14	15	20	40
Mean Value	Maximal R.M.S.	1.82	1.65	1.49	1.51	1.86	2.41	2.93	2.97	2.89	2.19	1.59
	Pin N	1	36	36	45	35	35	35	35	35	35	35
	Fission Rate	0.991	1.093	1.100	1.119	0.521	0.590	0.664	0.730	0.756	0.828	0.954
VISWAM	Fission Rate	0.982	1.106	1.110	1.124	0.513	0.579	0.646	0.712	0.740	0.825	0.962
	Deviation from Mean Value	–0.91	1.19	0.91	0.45	–1.54	–1.86	–2.71	–2.47	–2.12	–0.36	0.84
MCU	Fission Rate	1.002	1.068	1.080	1.101	0.517	0.588	0.660	0.726	0.750	0.826	0.945
	Deviation from Mean Value	1.13	–2.29	–1.81	–1.58	–0.72	–0.42	–0.58	–0.54	–0.76	–0.28	–0.91
TVS–M	Fission Rate	0.982	1.100	1.104	1.121	0.531	0.608	0.690	0.759	0.785	0.848	0.964
	Deviation from Mean Value	–0.89	0.64	0.37	0.20	1.97	2.97	3.93	3.98	3.87	2.37	1.09
WIMS8A	Fission Rate	0.963	1.082	1.089	1.108	0.522	0.589	0.659	0.722	0.747	0.819	0.946
	Deviation from Mean Value	–2.78	–0.97	–1.04	–0.97	0.29	–0.22	–0.66	–1.07	–1.12	–1.18	–0.83
HELIOS	Fission Rate	1.000	1.100	1.105	1.119	0.506	0.570	0.637	0.701	0.728	0.805	0.939
	Deviation from Mean Value	0.92	0.64	0.45	0.00	–2.80	–3.55	–4.03	–3.94	–3.70	–2.87	–1.58
MULTICELL	Fission Rate	1.007	1.115	1.122	1.145	0.527	0.598	0.673	0.742	0.769	0.845	0.975
	Deviation from Mean Value	1.62	1.98	2.03	2.36	1.26	1.22	1.34	1.58	1.71	1.95	2.23

Table 3.19 –Fission rate Distribution in S2 to S5 state with Burnup for MOXGD Fuel Assembly

		Burnup (MWD/KgHM)											
		S2 State			S3 State			S4 State			S5 State		
		0	20	40	0	20	40	0	20	40	0	20	40
Mean Value	Maximal R.M.S.	1.79	2.19	1.60	1.87	2.07	1.47	1.83	2.09	1.57	2.21	3.20	2.99
	Pin N	1	35	35	45	35	35	1	35	56	1	56	56
	Fission Rate	0.990	0.827	0.954	1.109	0.827	0.955	0.999	0.823	0.909	1.031	0.902	0.918
VISWAM	Fission Rate	0.982	0.824	0.964	1.122	0.830	0.969	0.988	0.827	0.911	1.004	0.887	0.914
	Deviation from Mean Value	–0.81	–0.36	1.05	1.17	0.36	1.47	–1.10	0.49	0.22	–2.62	–1.66	–0.44
MCU	Fission Rate	0.997	0.822	0.944	1.077	0.824	0.946	1.004	0.816	0.931	1.053	0.928	0.940
	Deviation from Mean Value	0.70	–0.60	–1.09	–2.90	–0.39	–0.91	0.55	–0.80	2.43	2.10	2.87	2.36
TVS–M	Fission Rate	0.982	0.847	0.964	1.119	0.846	0.963	0.991	0.843	0.902	1.042	0.917	0.935
	Deviation from Mean Value	–0.82	2.43	1.01	0.88	2.27	0.87	–0.75	2.48	–0.76	1.03	1.65	1.82
WIMS8A	Fission Rate	0.963	0.819	0.948	1.103	0.819	0.949	0.971	0.816	0.907	0.998	0.894	0.913
	Deviation from Mean Value	–2.71	–0.99	–0.62	–0.55	–0.94	–0.58	–2.77	–0.76	–0.22	–3.24	–0.91	–0.62
HELIOS	Fission Rate	1.000	0.804	0.939	1.115	0.804	0.940	1.009	0.801	0.912	1.046	0.916	0.931
	Deviation from Mean Value	0.99	–2.83	–1.57	0.51	–2.76	–1.50	1.07	–2.66	0.34	1.38	1.57	1.39
MULTICELL	Fission Rate	1.008	0.843	0.976	1.132	0.842	0.975	1.018	0.837	0.893	1.018	0.856	0.873
	Deviation from Mean Value	1.84	1.99	2.27	2.06	1.81	2.12	1.90	1.73	–1.80	–1.26	–5.17	–4.95

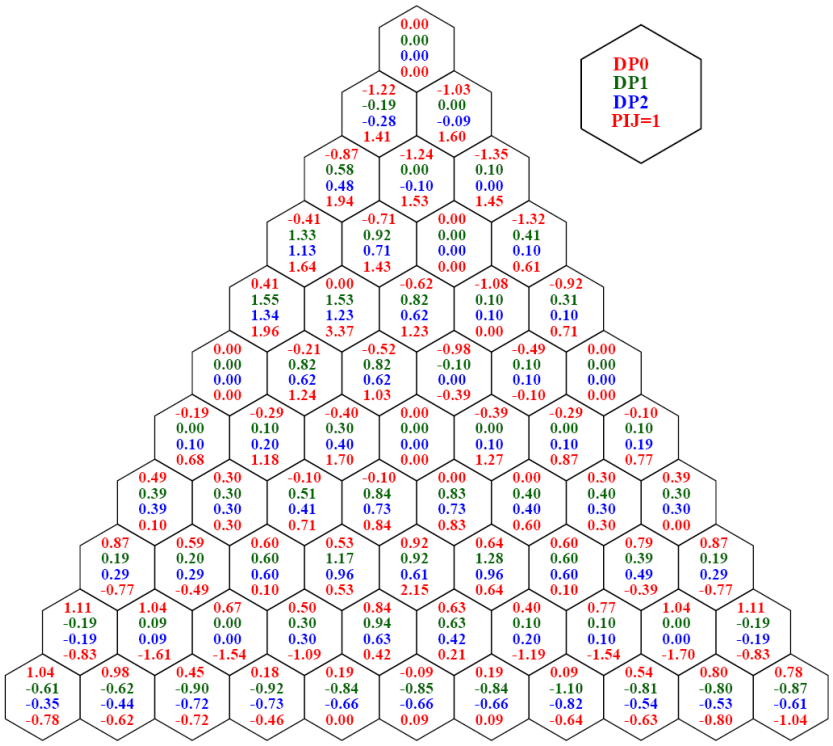

Fig. 3.54 Deviation in Fission Density Distribution w.r.t. BM Mean for S2 state of UGD FA at zero Burnup using four calculation methods

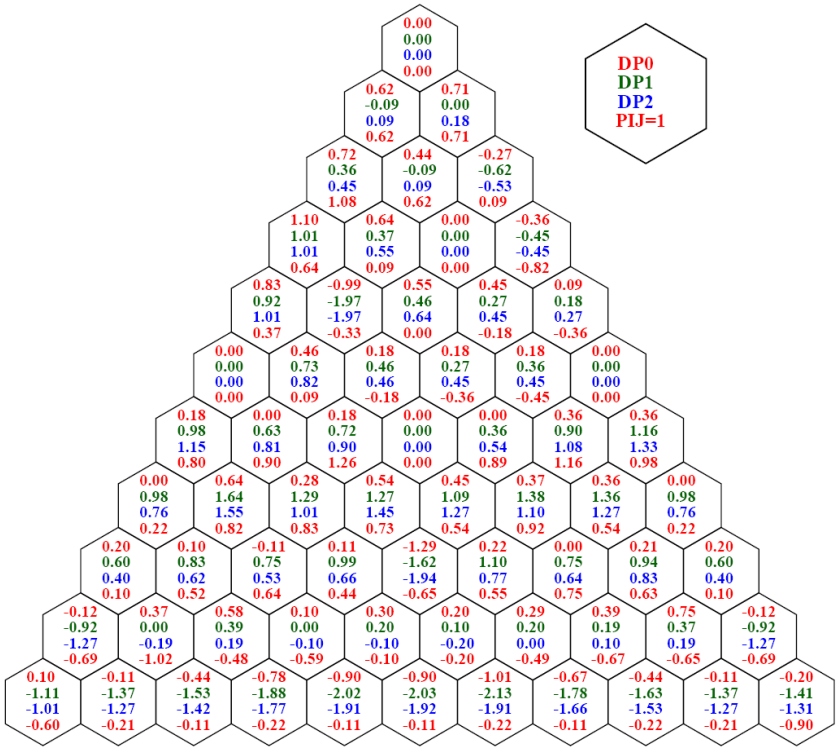

Fig. 3.55 Deviation in Fission Density Distribution w.r.t. BM Mean for S2 state of MOXGD FA at zero Burnup using four calculation methods

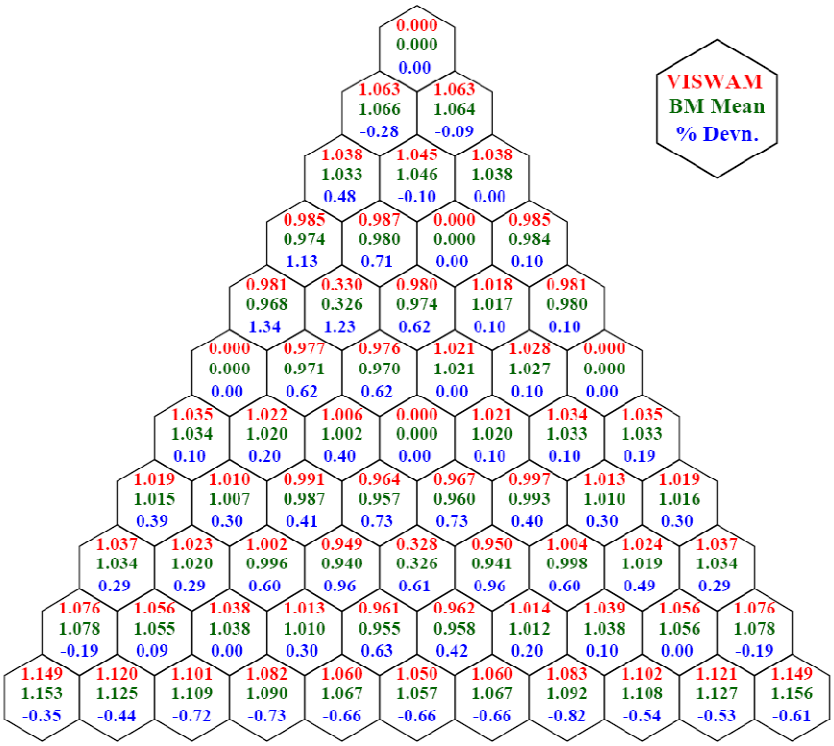

Fig. 3.56 Fission Density Distribution for S2 state of UGD FA at Burnup = 0 MWD/KgHM

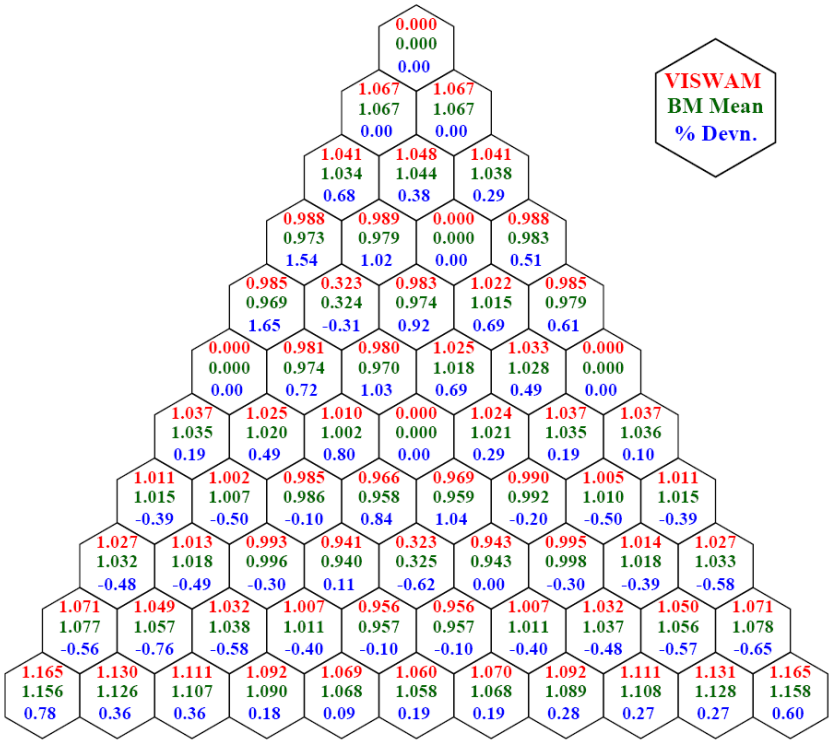

Fig. 3.57 Fission Density Distribution for S3 state of UGD FA at Burnup = 0 MWD/KgHM

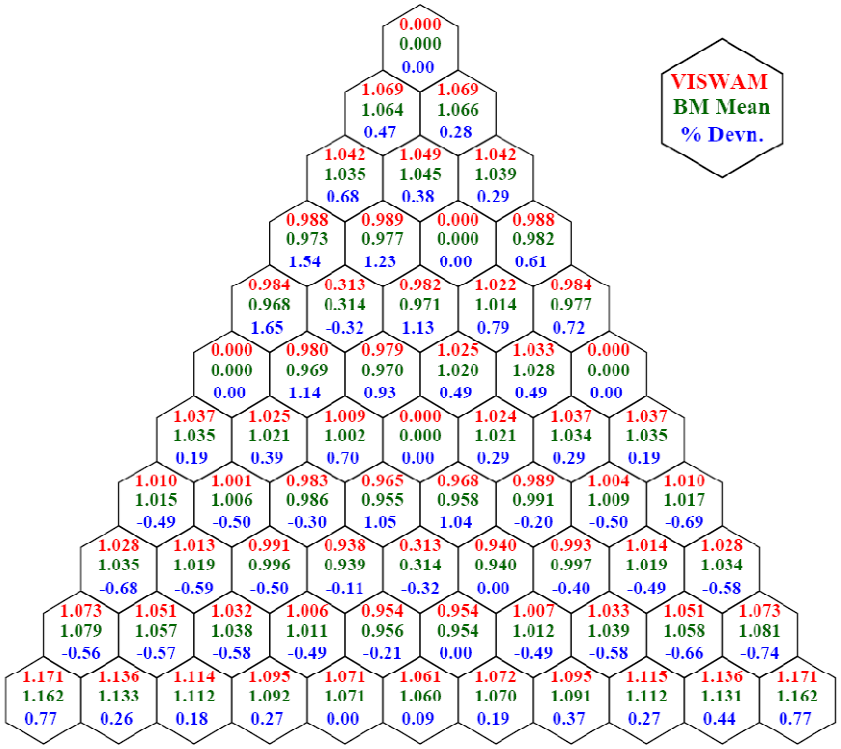

Fig. 3.58 Fission Density Distribution for S4 state of UGD FA at Burnup = 0 MWD/KgHM

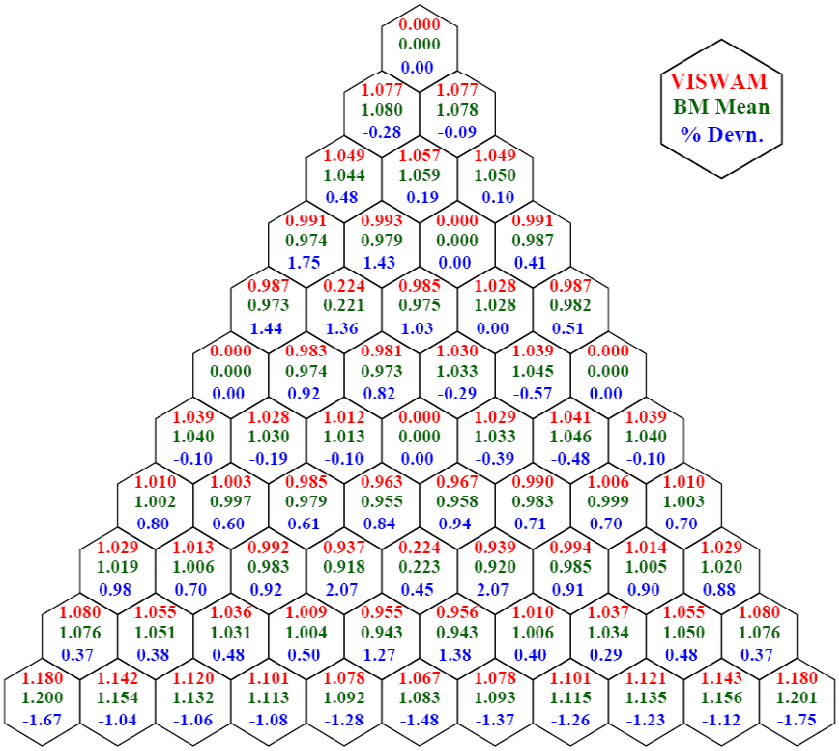

Fig. 3.59 Fission Density Distribution for S5 state of UGD FA at Burnup = 0 MWD/KgHM

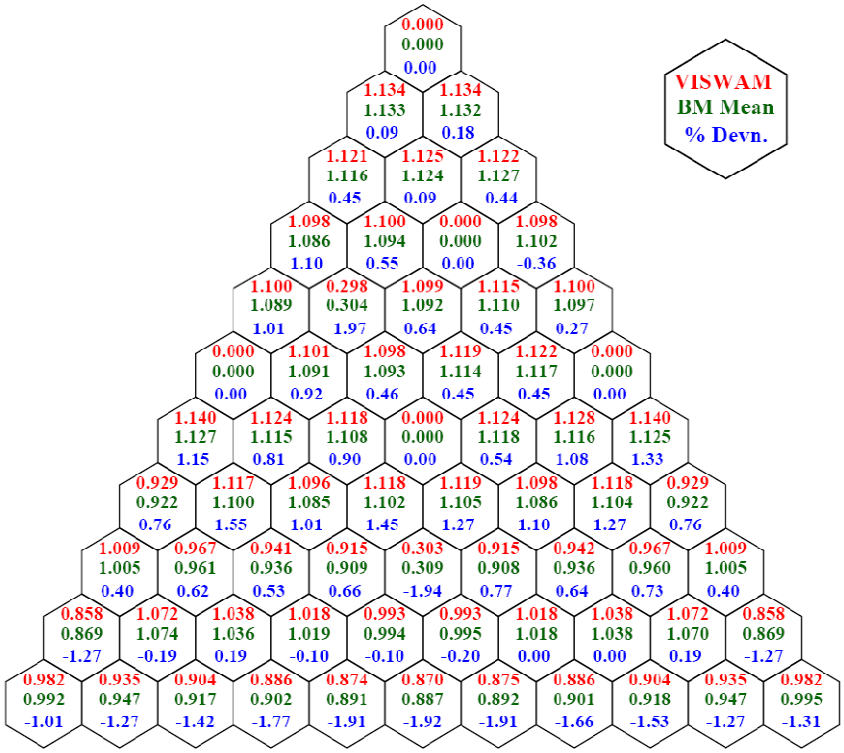

Fig. 3.60 Fission Density Distribution for S2 state of MOXGD FA at Burnup = 0 MWD/KgHM

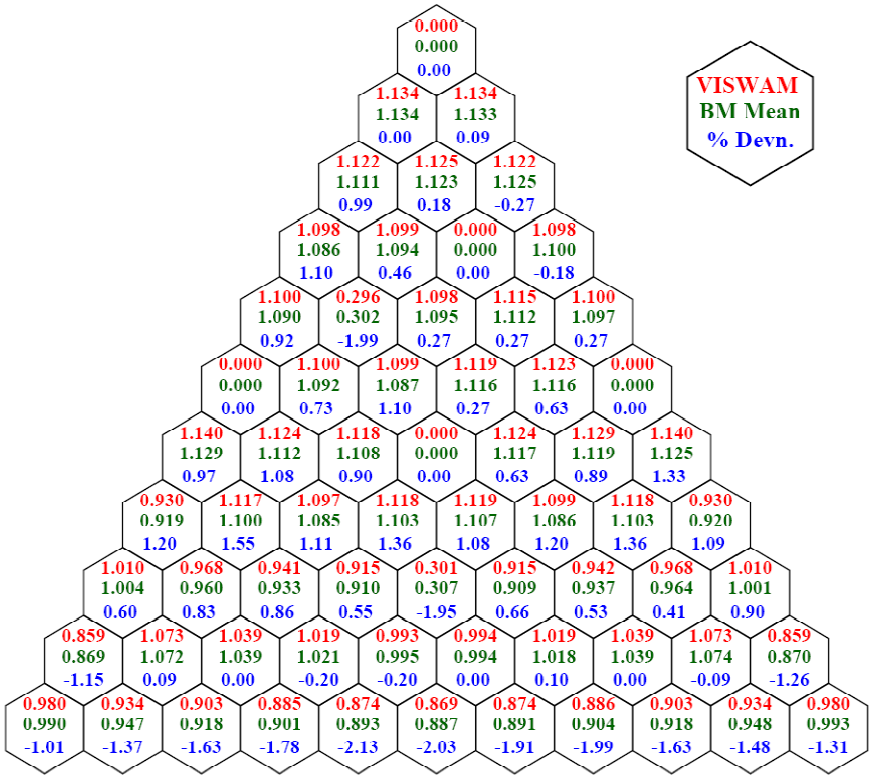

Fig. 3.61 Fission Density Distribution for S3 state of MOXGD FA at Burnup = 0 MWD/KgHM

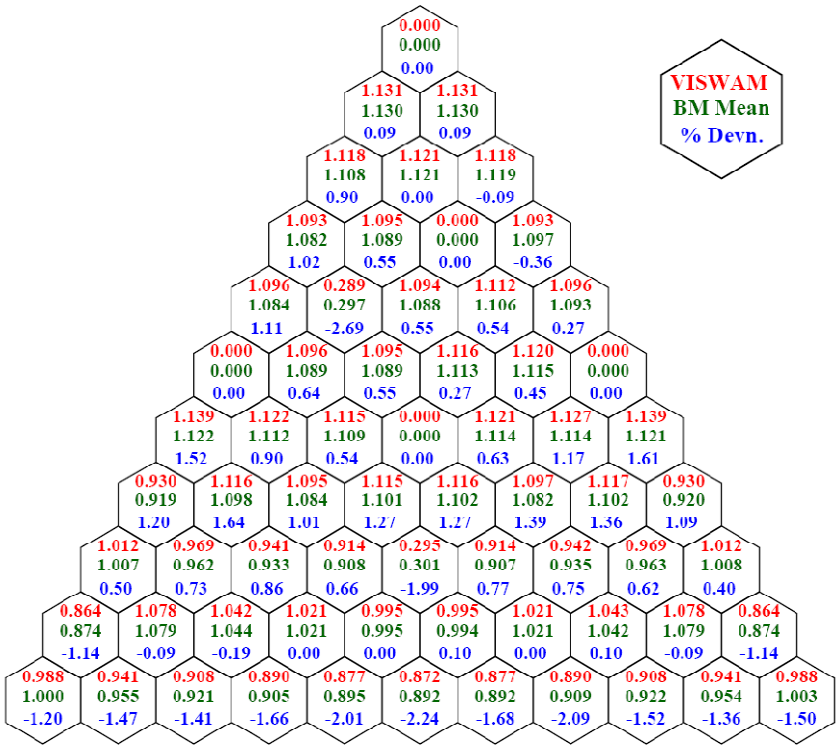

Fig. 3.62 Fission Density Distribution for S4 state of MOXGD FA at Burnup = 0 MWD/KgHM

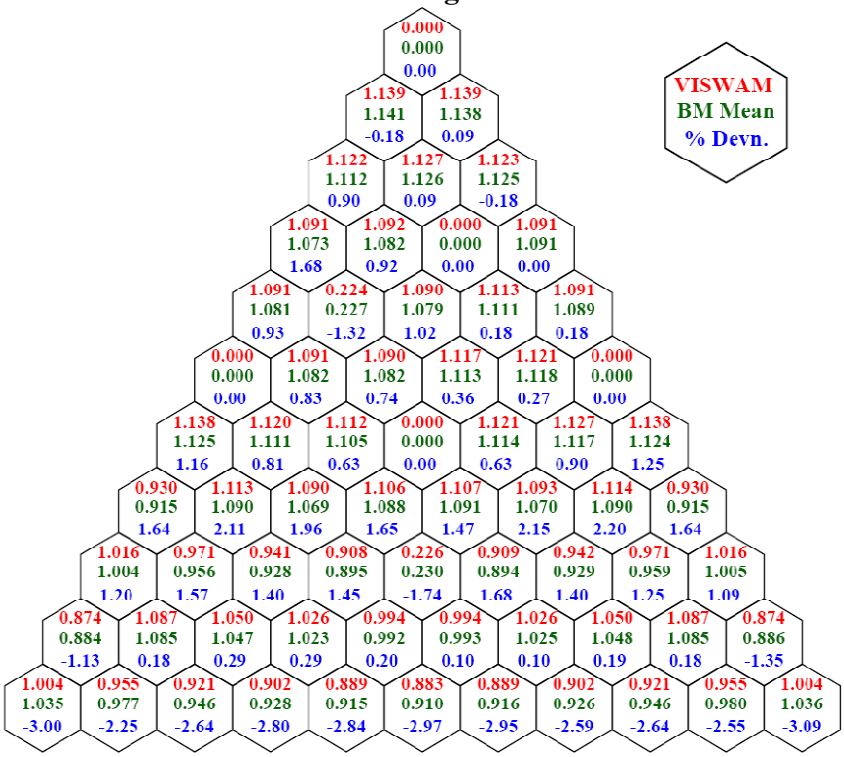

Fig. 3.63 Fission Density Distribution for S5 state of MOXGD FA at Burnup = 0 MWD/KgHM

3.7 Summary

The interface current method using double P2 (DP2) expansion of angular flux at lattice cell surfaces has been implemented in the lattice analysis code VISWAM. The VISWAM code was used to analyse heterogeneous HTTR benchmark and VVER–1000 OECD LEU and MOX Computational Benchmark problems. The results are compared for a single fuel pin and fuel assembly cell calculations. The results show a good agreement in k_∞ for pincell and assembly calculation (within 0.01% and 0.18%) for HTTR benchmark. The maximum difference in fission density distribution is 0.78% for the lowest enrichment. The RMS error in the power distribution is seen as 0.13%. For VVER–1000 OECD benchmark, the k_∞ comparison shows improved agreement with reference MCNP values by using higher order expansion functions. The results using P1 anisotropy show an improvement of around 4 mk in k_∞ as compared to P0 values and 0.5 mk using P2 anisotropy w.r.t. P1 values. The %RMS deviation in fission densities for P0, P1 & P2 cases is seen to be 1.03%, 0.549% & 0.462%. A sensitivity study of k_∞ with discretization parameters *vis–a–vis* angular expansion of flux for fuel assembly was performed for both the benchmarks. It was seen that the flux anisotropy affects the results more strongly after an optimum set of discretization parameters.

The burnup characteristics of DP2 model were studied using VVER–1000 OECD LEU and MOX Computational Benchmark. The calculation was carried out using all the methods available in VISWAM. While using the interface current method, the calculation was performed by using P0, P1 and P2 expansions of angular flux at the lattice cell boundary. The calculated results were compared with BM values and other evaluations given in benchmark report. The comparison of k_∞ shows a smooth variation with burnup. The least deviation from BM is obtained using P2 expansion. The reactivity effects of (Xe, Sm) and isothermal temperature are

predicted better by DP1/DP2 models. Doppler load shows more deviation. It is felt that the resonance treatment in multiple fuel rings should be suitably modeled to take care of the rim effect which will improve the prediction of Doppler load. The boron load comparison is seen satisfactory. The assembly average and individual cell isotopic composition of fuel nuclides and selected fission products like ^{135}Xe and ^{149}Sm show a good comparison with BM values. The fission density distribution was compared for primary and branching calculation with burn up. The comparison shows good agreement with BM values. The maximum deviation is seen to be 2.03% for UGD FA and –2.71% for MOXGD FA. The detailed pin by pin fission density distribution for 1/6th FA at zero burnup for branching calculations showed a good agreement with BM values. The results obtained using P2 expansion of angular flux showed, in general, least deviation from BM values.

The burnup approach used in VISWAM for DP2 model has performed satisfactorily for the prediction of variation of k_∞ with burnup, prediction of various reactivity effects, variation of isotopic densities with burn up and pin wise fission density distributions in the assembly. So this model can be adopted for performing 2D/3D whole core calculation using DP2 model of interface current method.

CHAPTER – 4

SCHEME AND METHODOLOGY OF WHOLE CORE PIN–BY–PIN CALCULATION

The two step calculation method to perform whole core calculation and its limitations has been discussed in Chapter – 1. Due to advances in computing processing power, pin–by–pin fine mesh core calculation methods are being considered as high potential algorithm for next–generation core analysis tools. The basic approach in the whole core transport theory methods is not to homogenize the lattice cells. Each lattice cell location in the fuel assembly (FA) is subdivided into finer regions. The interface current method based on 2D collision probability has been used for performing whole core calculation. A transport theory code TRANPIN has been developed to perform a whole core pin–by–pin calculation in 2D hexagonal geometry. The subdivided regions inside the lattice cell are connected using the 2D collision probabilities. The coupling of individual lattice cells within the assembly and assembly to assembly coupling in the core is achieved using interface currents. The interface currents are obtained by expanding the angular flux leaving or entering the lattice cell surface into double orthonormal P_N polynomials. The theoretical details of the interface current method incorporated in TRANPIN has been described in detail in Chapter – 2. This Chapter describes the spatial discretisation of whole core using fine meshes, the numbering scheme of the meshes, connectivity of the meshes and iteration scheme adopted for the solution method. When there is an inherent symmetry one can solve for the symmetric portion of the core, thereby saving both memory and computational time. Rotational symmetry boundary condition in the whole core is normally considered [11]. Application of this boundary condition gets very complicated when the whole core is modeled by

a pin–by–pin approach. This Chapter also describes the methodology to apply the rotational symmetry boundary condition as implemented in TRANPIN, in the whole core problem discretized with complex microstructures of various heterogeneous cells of the problem.

4.1 Conventions Considered in TRANPIN

To perform the core calculation in a deterministic numerical code, the geometry needs to be discretized. In TRANPIN, the meshes appearing in the whole core discretized geometry are numbered in two stages. First, the fuel assembly locations including reflector in the solution domain of core are numbered from core centre to boundary hexagonal layer in a spiral manner. This is illustrated in Fig. 4.1 for a representative 60° symmetric core problem. The numbering scheme is shown for $1/6^{th}$ of core problem. Afterwards, the lattice cells inside each fuel assembly are also numbered from fuel assembly centre to outermost layer in a spiral manner as shown in Fig. 4.2 for a representative assembly discussed in Fig. 3.12/3.13 of Chapter–3. The spiral numbering of meshes helps in starting the iterative solution process from the most important region of the solution domain i.e. the core centre.

The surfaces of the hexagonal fuel assembly are numbered cyclically from bottom left side in anti clockwise direction as shown in Fig. 4.3. As seen in Figs. 3.1, 3.12 or 3.13 of Chapter–3, there is a regular hexagon structure within the fuel assembly. Beyond this regular structure, there is a thin layer of moderator. In this layer, two distinct geometric shapes are encountered which are designated as side meshes (Fig.3.3a) and corner meshes (Fig.3.4a). The surface numbering convention in these meshes is shown in Fig.4.4. The surface numbering convention for (4.4b) & (4.4c) is fixed i.e., the numbering is also rotated along with the shape so that the surface number doesn't change on rotation of these meshes.

4.2 Mesh Connectivity in TRANPIN

In the interface current method, as seen from Eq. (2.28) of Chapter–2, the meshes are linked through interface currents as follows:

$$J_{in} = J_{out\ of\ neighbour}$$

i.e. the incoming current into the mesh is obtained from the outgoing current from the neighbouring mesh through the common surface. The meshes within an assembly location are connected to their neighbours through one of the common surfaces shown in Fig. 4.4. At the outermost layer of FA, only mesh shapes shown in Fig. 4.4b & 4.4c appear. The inter assembly coupling is achieved through these meshes only. This is illustrated in Fig. 4.5. Due to the numbering convention described above, the side meshes are connected only through common surface 1 and the corner meshes are connected through surfaces 1 & 2 to the corresponding meshes in neighbouring FAs.

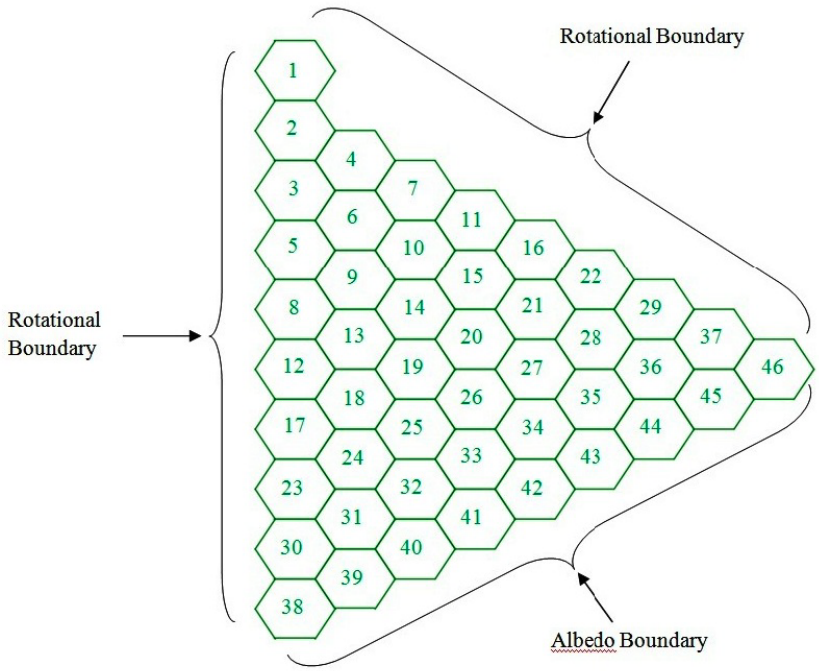

Fig. 4.1 – FA numbering in Core

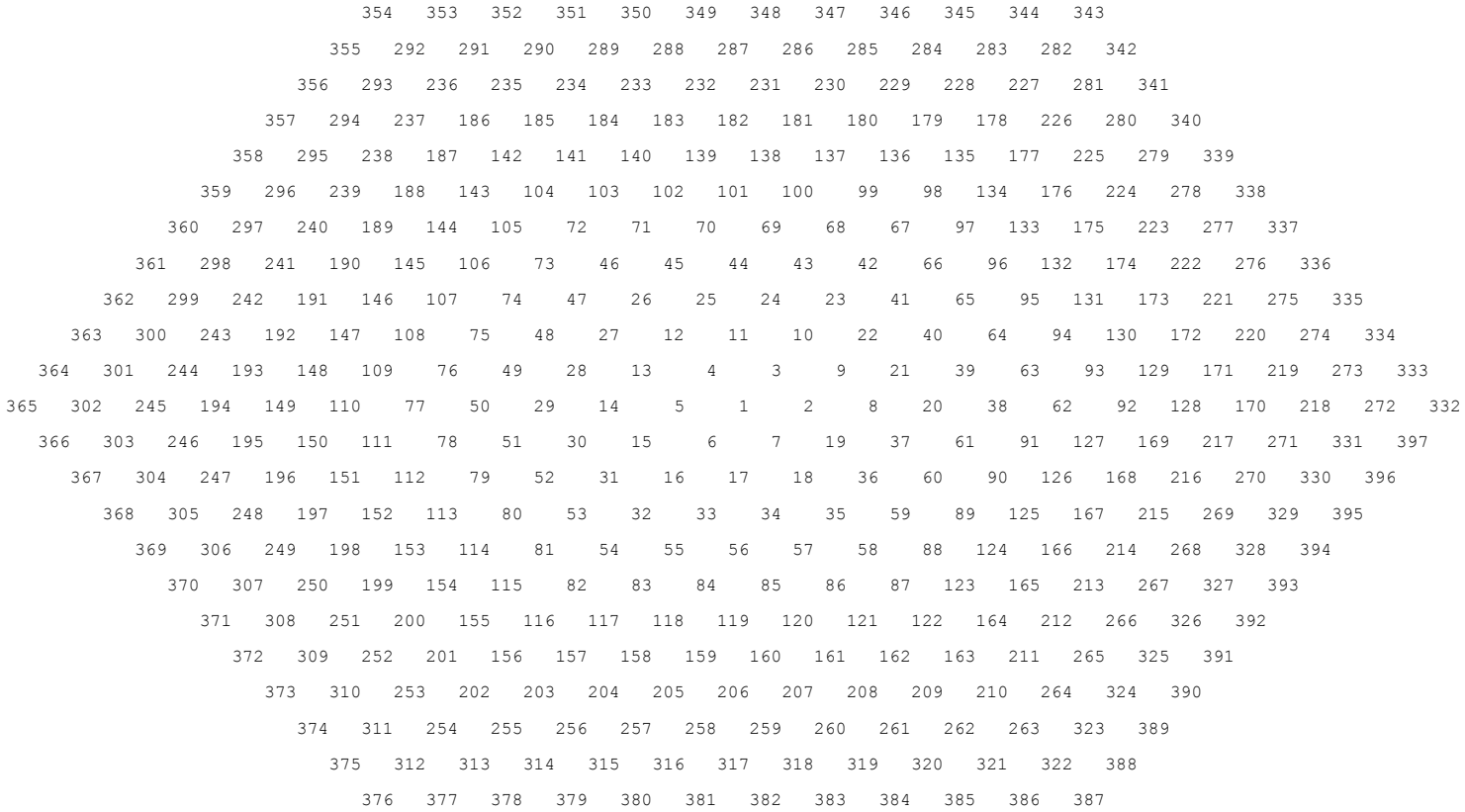

Fig. 4.2 – Spiral Numbering of Meshes in a Representative Assembly Location

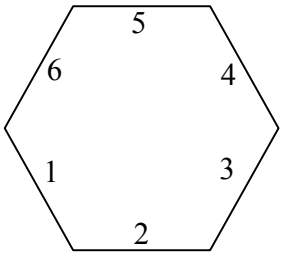

Fig. 4.3 – Surface Numbering for Hexagonal Fuel Assembly Location

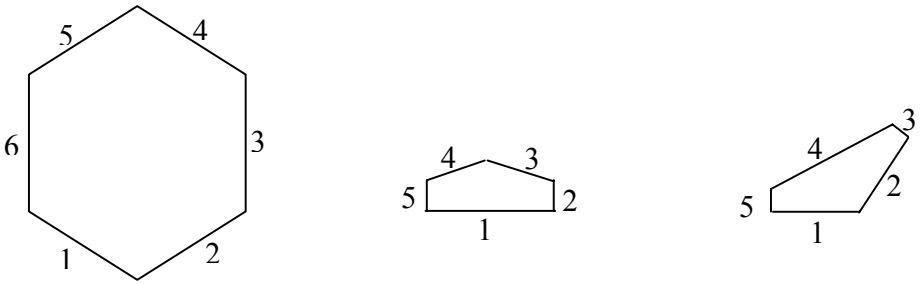

(a) **(b)** **(c)**

Fig. 4.4 – Surface numbers in (a) – hexagonal, (b) – side and (c) – corner meshes within an Assembly Location

While numbering the assembly locations in the core, their six neighbors are also found and stored. The convention shown in Fig. 4.3 is followed to determine the assembly neighbors in order. The lattice cell numbering in each individual assembly location is identical as shown in Fig.4.2. For achieving the proper current coupling on the boundary surfaces of an assembly, it is necessary to identify the boundary lattice cells on each surface of a reference FA and the corresponding lattice cells of the neighbouring FA in the same order. For this purpose, a full sweep of the core solution domain is performed in order to find the neighbors of the peripheral meshes of every assembly location. Table–4.1 gives the neighbouring meshes (boundary lattice cells) for a representative non boundary assembly no. 14 shown in core map in Fig. 4.1 on each of the six sides of the FA. It may be pointed out that the corner lattice cell (single numbers in alternate shaded rows of the Table – 4.1) is linked to the two corner cells of two neighbouring FAs through common surface 1 or 2, and side lattice cells appearing as a row of lattice cells in

alternate unshaded rows of Table – 4.1, are linked to the corresponding row of cells of neighboring FA through the common surface 1. As seen in Fig. 4.1, there are three boundaries of the solution domain in 1/6th core. Two of them are rotational symmetry boundaries and third is vacuum boundary. Table – 4.1 holds true for all the FAs not present on the two rotational boundaries shown in Fig. 4.1.

For simulating rotational boundary condition, the assemblies present on the left boundary have to be linked to those on the right boundary and vice versa. For the left boundary assemblies, the boundary surfaces are 1 & 6 (see Fig. 4.3 & Fig. 4.1) whereas boundary surfaces for right boundary assemblies are 4 and/or 5. The meshes on these surfaces cannot be linked directly by mere translation because the surfaces tend to change and get rotated on account of 60° rotation.

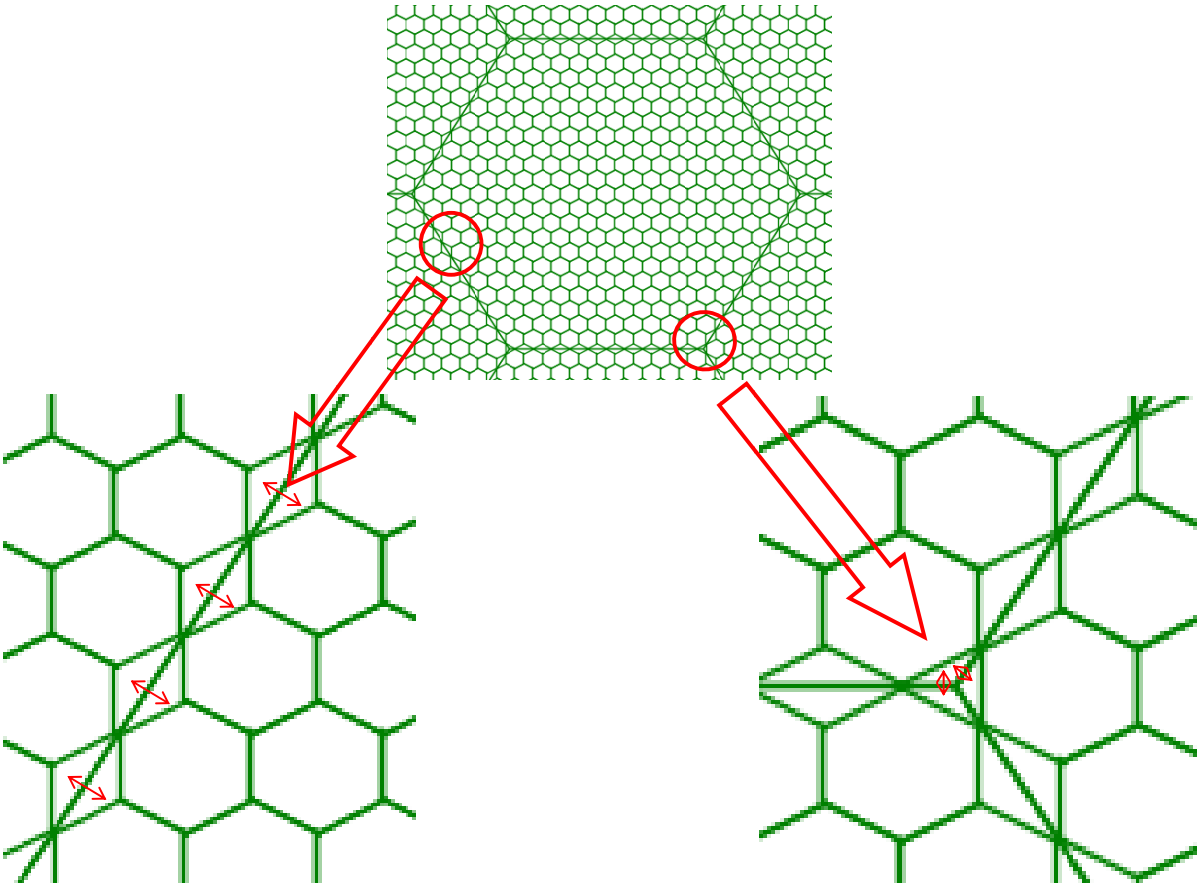

Fig. 4.5 – Mesh Connectivity between neighbouring Fuel Assemblies

Table 4.1 – Neighbors of Peripheral meshes of FA No. 14

Surface No. of FA 14	Lattice cells of FA 14	Lattice cells in the Neighbouring FAs (Numbers in bracket are FA numbers)
1	365	387 (9) &343 (13)
	366 to 375	342 to 333 (13) in order
2	376	332 (13) & 354 (19)
	377 to 386	353 to 344 (19) in order
3	387	343 (19) & 365 (20)
	388 to 397	364 to 355 (20) in order
4	332	354 (20) & 376 (15)
	333 to 342	375 to 366 (15) in order
5	343	365 (15) & 387 (10)
	344 to 353	386 to 377 (10) in order
6	354	376 (10) & 332 (9)
	355 to 364	397 to 389 (9) in order

The surfaces on the left boundary will undergo –60° rotation whereas on the right boundary will undergo +60° rotation. Table–4.2 gives the surface number after rotation by ±60° for each of the surfaces. As seen from Table–4.2, the surfaces 1 & 6 of FAs on left rotational boundary will be linked to surfaces 5 & 4 of FAs on the right boundary respectively. Similarly, the surfaces 4 & 5 of FAs appearing on the right rotational boundary will be linked to surfaces 6 & 1 of FAs on left rotational boundary respectively. Table–4.3 gives the modified linking of peripheral meshes of a representative FA no. 12 appearing on left boundary with the meshes of FAs on right rotational boundary. This modified coupling of meshes is obtained after considering the rotation of surfaces given in Table–4.2. Similarly, Table–4.4 gives the modified coupling of meshes of representative FA no. 29 appearing on right rotational boundary with the meshes on left boundary. The meshes appearing on non boundary FA surfaces of rotational symmetry lines will follow the linking provided in Table–4.1. It is noted from Table–4.3 & 4.4 that only one surface of the two corner meshes appearing on the start and end of the boundary surfaces need to undergo modification of neighbors. The unmodified surfaces of these corner meshes are marked with asterisk in Tables–4.3 & 4.4. They are interior meshes with no exterior boundary surface.

This determination of neighbors and neighboring surfaces is performed in geometry processing routine and stored at the start of calculation.

Table 4.2 – Effect of Rotation on the surfaces of FA

-60° Rotation (Anticlockwise)		+60° Rotation (Clockwise)	
Surface No.	**Surface after Rotation**	**Surface No.**	**Surface after Rotation**
1	2	1	6
2	3	2	1
3	4	3	2
4	5	4	3
5	6	5	4
6	1	6	5

Table 4.3 – Neighbors of Peripheral meshes of FA No. 12 on left boundary

Surface No. of FA 12	Lattice cells of FA 12	Lattice cells in the Neighbouring FAs (Numbers in bracket are FA numbers)
1	365	332 (16) &354 (22)
	366 to 375	353 to 344 (22) in order
2	376	343(22) & 354* (17)
6	354	376* (8) & 343 (16)
	355 to 364	342 to 333 (16) in order

Table 4.4 – Neighbors of Peripheral meshes of FA No. 29 on right boundary

Surface No. of FA 14	Lattice cells of FA 14	Lattice cells in the Neighbouring FAs (Numbers in bracket are FA numbers)
4	332	354* (37) & 365 (23)
	333 to 342	364 to 355 (23) in order
5	343	354 (23) & 376 (17)
	344 to 353	375 to 366 (17) in order
6	354	365 (17) & 332* (22)

** Interior Meshes connected without rotational symmetry*

4.3 Iteration Scheme in TRANPIN

The purpose of solution scheme is to find the reaction rates or scalar flux in all the discretized regions in the whole core. The scalar flux in TRANPIN is obtained using the multigroup iteration scheme based on power or source iteration method. The power iteration

method makes use of the inner–outer iteration method. For the inner iteration for a group, the total source is computed in all the regions. The total source in region *i* is defined as follows

$$q_i = \Sigma_i^S \phi_i V_i + S_i V_i. \tag{4.1}$$

The group source S_i is defined as

$$S_i = \left(\sum_{\substack{g'=1 \\ g' \neq g}}^{G} \Sigma_{si}^{g' \to g} \phi_i^{g'} + \frac{\chi_g}{k_{eff}} \sum_{g'=1}^{G} \nu \Sigma_{fi}^{g'} \phi_i^{g'} \right). \tag{4.2}$$

To start the iteration procedure, an initial source guess is calculated using 1/E flux guess from the energy boundaries of the multigroup structure. After computing the total source, the solution domain of the whole core is swept to calculate the scalar flux and outgoing current components defined by Eqs. (2.23) and (2.26). A self scattering reduction scheme is adopted for Eq. (2.23) *i.e.* all the information of self scattering of a group is transferred to left side as shown in Eq. (2.72). This completes one inner iteration. The scattering source component in Eq. (4.2) is updated in the next inner iteration for second group. The process is repeated till the completion of group loop.

In the outer iteration loop, the eigenvalue equation is solved. The general form of the eigenvalue value problem in TRANPIN can be written in operator notation as [53]:

$$\boldsymbol{T}\, \vec{\phi} = \frac{1}{k_{eff}} \boldsymbol{F}\, \vec{\phi}. \tag{4.3}$$

where **F** represents the fission and **T** represents the streaming, absorption, and scattering of neutrons. Using the power iteration method to solve Eq. (4.3) results in the following

$$\vec{\phi}^{(n+1)} = T^{-1} \frac{1}{k_{eff}^{(n)}} \boldsymbol{F}\, \vec{\phi}^{(n)}. \tag{4.4}$$

$$k_{eff}^{(n+1)} = \frac{\left\| \boldsymbol{F}\, \vec{\phi}^{(n+1)} \right\|}{\frac{1}{k_{eff}^{(n)}} \left\| \boldsymbol{F}\, \vec{\phi}^{(n)} \right\|}. \tag{4.5}$$

Where n is the outer iteration index. The fission source in Eq. (4.2) is updated after every outer iteration. This inner-outer iteration loop is repeated till the desired convergence in eigenvalue and scalar flux is reached. The eigenvalue is also estimated using neutron balance.

4.4 Salient Features of TRANPIN

TRANPIN performs the whole core calculation without any geometric distortion of the problem. The geometry is modeled exactly up to single lattice cell. The geometric discretization at lattice cell level is very flexible *i.e.* the discretization of different regions such as fuel, clad and associated coolant in the lattice cell can be performed externally. The solution method permits flexibility in choosing the quality of the calculation by both increasing the number of regions modeled within the lattice cell and choosing the order of incoming and outgoing angular flux expansion at the lattice cell surface.

The methodology incorporated in TRANPIN uses advanced numerical methods which make use of the inherent configuration symmetries to reduce the amount of calculations and computational time. This is illustrated in the calculation of collision probabilities. First the materially and geometrically distinct fuel assemblies are sorted in the whole core. The collision probabilities are only calculated for geometrically and materially distinct lattice cells identified within these distinct fuel assemblies. Also symmetry, reciprocity relations and transformation laws are used to further reduce these collision probability computations.

TRANPIN has the capability to model variable pitch within the fuel assembly i.e. the lattice cells with non uniform pitch can be linked using interface currents. This will be described in detail in Chapter 5.

TRANPIN has been written in FORTRAN 90 and uses advanced modular structure of the language. All the routines in the TRANPIN make extensive use of features such as dynamic

memory allocation, modular attributes, array operations, user defined data structures and derived types. The code is now compact and modular. It is amenable for augmenting different calculation algorithms as may be identified through validation exercise of a variety of benchmark problems.

TRANPIN can model large problems with many cells/regions in the whole core. The discretization of energy domain is fully flexible *i.e.* it can consider any group structure for multigroup modeling of the problem.

4.5 Summary

A whole core transport theory code TRANPIN in 2D hexagonal geometry has been developed. The code performs the full core calculation, without homogenizing the various lattice cells present in the FAs, in multi group formalism. The code TRANPIN uses the interface current method based on 2D collision probability to solve the transport equation for the whole core problem. The individual cells in the FA are subdivided into finer regions. The coupling of cells within an assembly and inter assembly coupling is achieved using interface currents. The incoming/outgoing angular flux at the lattice cells interface is expanded in P_N functions. The expansion is limited to P2. Albedo boundary condition is applied at the outermost surfaces of the cells. The huge memory requirement for whole core transport calculation can be reduced by using the intrinsic symmetry of the problem. The 60° rotational symmetry has been implemented in TRANPIN code.

CHAPTER – 5

NUMERICAL RESULTS OF WHOLE CORE PIN–BY–PIN CALCULATION

The whole core pin–by–pin calculation code TRANPIN solves the transport equation for the full core using the interface current method based on 2D collision probability (CP) method. TRANPIN has been used to analyze two heterogeneous full core benchmark problems in 2D geometry *viz*. a simplified HTTR benchmark problem [54] and the OECD VVER–1000 MOX Core Computational Benchmark [55]. This chapter presents in detail the numerical results of the application of TRANPIN to the above two problems. The description of the benchmark problems is presented in Section 5.1. Section 5.2 gives the results of the analysis. Section 5.3 presents the brief summary of this Chapter.

5.1 Description of Benchmark Problems

Two heterogeneous benchmark problems are studied using TRANPIN code system for benchmarking and validating the methodology incorporated in TRANPIN. The detailed specification of these benchmarks is described below.

5.1.1 HTTR Benchmark

Zhang et al [54] has proposed a heterogeneous 2D benchmark problem that is typical of a high temperature reactor in hexagonal geometry, to test the accuracy of modern transport methods for neutronics analysis. This problem was derived from the High Temperature Engineering Test Reactor (HTTR) start–up experiment, which was built by JAERI, Tokyo, Japan in the late 1990's. The present problem is a simplified benchmark problem which is obtained by removing the detailed design specific material and structural details of HTTR while retaining the

heterogeneity and major physics properties from the neutronics viewpoint. The detailed physics simplifications adopted to arrive the present benchmark configuration are described in detail in [54].

The benchmark problem is a whole core heterogeneous 2D configuration in hexagonal geometry as shown in Fig. 5.1 (a). The reactor core is modeled as a regular hexagon with a flat–to–flat distance of 436.4768 cm and is completely filled by a hexagonal lattice cells of fuel, control and reflector blocks. These hexagonal blocks are all of uniform size with a block pitch of 36 cm, except at the periphery in which case there are half blocks along the core edges and 1/3rd blocks at the corners. The block lattice configuration, divided into eight regions, is shown in Fig. 5.1(b). Regions 1 to 4 shown in Fig. 5.1(b) are fuel blocks of increasing enrichment. Regions 5 and 6 are filled or empty control rod blocks depending on the core configurations considered in [54]. In the All Rods IN Configuration studied with TRANPIN and presented in this Chapter, both regions 5 and 6 are filled control blocks. Regions 7 and 8 are replaceable and permanent reflector blocks, respectively. There are 30 fuel blocks, 19 control blocks, 12 replaceable reflector blocks and 108 permanent reflector blocks in the whole core. Vacuum boundary conditions are prescribed on the external boundaries of the core. The three fundamental block geometries appearing in the core *viz.* fuel blocks, reflector blocks, and control rod blocks are shown in Fig. 5.2. Each fuel block consists of 33 identical fuel pin cells, 3 burnable poison (BP) cells and one central graphite pin. The fuel pin pitch in the block is 5.15cm and fuel pin diameter is 4.1cm. The BP rod has a diameter of 1.5 cm. The fuel enrichment is uniform within any single block but varies from block to block in the core. Each control rod block has a single removable control rod of 12.3 cm diameter at its center.

The benchmark provides the 6–group, transport corrected macroscopic cross section library for four fuel cross sections (corresponding to the four enrichment levels defined in the core), four graphite cross sections (corresponding to graphite in fuel blocks, in control rod blocks, and in permanent and replaceable reflector blocks), and cross sections for burnable poison pins and control rods. The macroscopic cross section library had been obtained by a detailed lattice calculations using HELIOS code system [56]. The six group energy group structure is shown in Table 5.1. The details of cross section library generation using HELIOS and the values thereof can be found in [54].

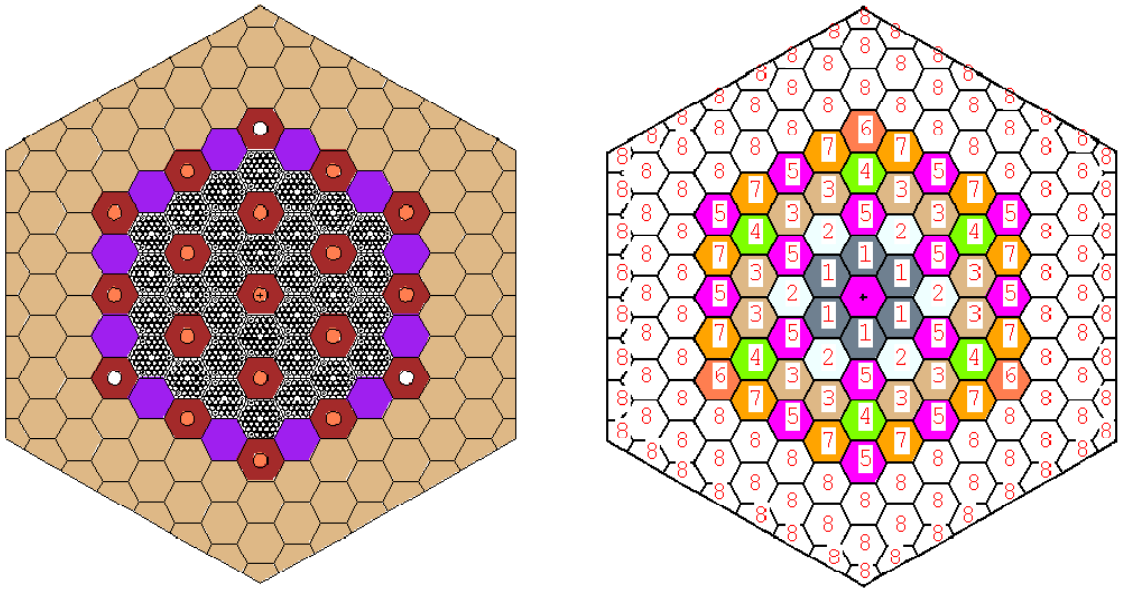

(a) (b)

Fig. 5.1 – The whole core structure and configuration of the simplified HTTR benchmark. (a) Full core structure, (b) Region indexing in the full core.

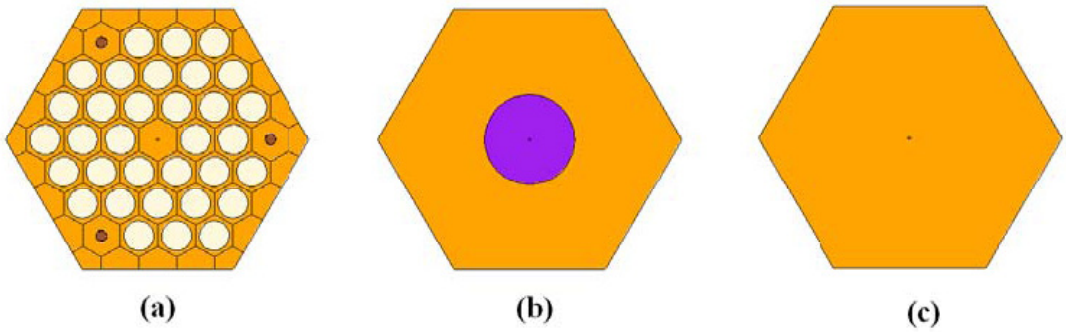

Fig. 5.2 – Block structures: (a) fuel blocks, (b) control rod blocks, (c) reflector blocks.

Table 5.1 – Energy Structure of Group Constants

Group	Upper energy (eV)
1	1.00×10^{7}
2	1.83×10^{5}
3	9.61×10^{2}
4	2.38
5	0.65
6	0.105

5.1.2 OECD VVER–1000 MOX Core Computational Benchmark

The expert group at NEA has proposed a computational benchmark to investigate the physics of a whole VVER–1000 reactor core using two–thirds low–enriched uranium (LEU) and one–third MOX fuel [55]. This benchmark was proposed for certification of calculation codes for future MOX fuel utilization in VVER–1000 reactor cores. This is required due to marked differences in physics behavior of MOX and standard LEU fuels. The benchmark model consists of a full-size 2–D VVER–1000 core with heterogeneous 30% MOX–fuel loading. There are a total of 28 FAs (1 central + 27) in the $1/6^{th}$ symmetric part of the core. The assembly pitch is 23.6 cm. The system has an infinite axial dimension and vacuum boundary condition is applied on the exterior side surface. The core map is shown in Fig. 5.3. The core consists of fresh and

burned fuel assemblies (FA) of two types – graded UOX FA with U–Gd burnable absorber (BA) rods and profiled MOX FA with U–Gd BA rods. The UOX and MOX FA configurations are as shown in Figs. 5.4 and 5.5. Each FA consists of 331 hexagonal lattice cell locations with 312 fuel pins, 18 guide tube cells with or without control absorber and one central guide tube cell with water. The pin pitch within the FA is 1.275 cm. In the UOX FA, the inner 240 fuel pins have 4.2 wt% ^{235}U enrichment while outer 66 pins have ^{235}U enrichment of 3.7 wt%. The 6 U/Gd pins have a ^{235}U enrichment of 3.3 wt% and a Gd_2O_3 content of 5.0 wt%. The MOX FA has three types of Pu enrichment. The inner 234 pins have MOX fuel with 3.6 wt% Pu, 54 edge pins have 2.7 wt% whereas and six corner pins have 2.4 wt%. The 18 Gd pins in MOX FA have a ^{235}U enrichment of 3.6 wt% and a Gd_2O_3 content of 4.0 wt%.

The core is surrounded by a reflector. The reflector is a very complicated structure consisting of a thin film of water, steel baffle with inner zigzag boundaries annexing the core and outer circular boundary and with water holes to insert surveillance thimbles, steel barrel, down comer water acting as thermal shield and steel pressure vessel. The water gap of 3 mm thickness is located between fuel assemblies and steel baffle. The VVER–1000 equilibrium core burnup distribution has been simplified by considering only two types of fuel assemblies with a fixed set of burn–ups. UOX FAs have average fuel assembly burn–ups of 0, 15, 32 and 40 MWd/kg, and MOX FAs have average fuel burn–ups of 0, 17 and 33 MWd/kg. The isotopic composition should be different in each fuel pin depending on the burnup accumulated in that pin. For simplicity, it is assumed that fuel pins of the same type have the same nuclide composition being a function only of average FA fuel burnup. The benchmark provides the isotopic composition of the all the fuel materials and various structural materials like fuel clad, guide tube, borated coolant, steel baffle, steel barrel and steel vessel required in the problem.

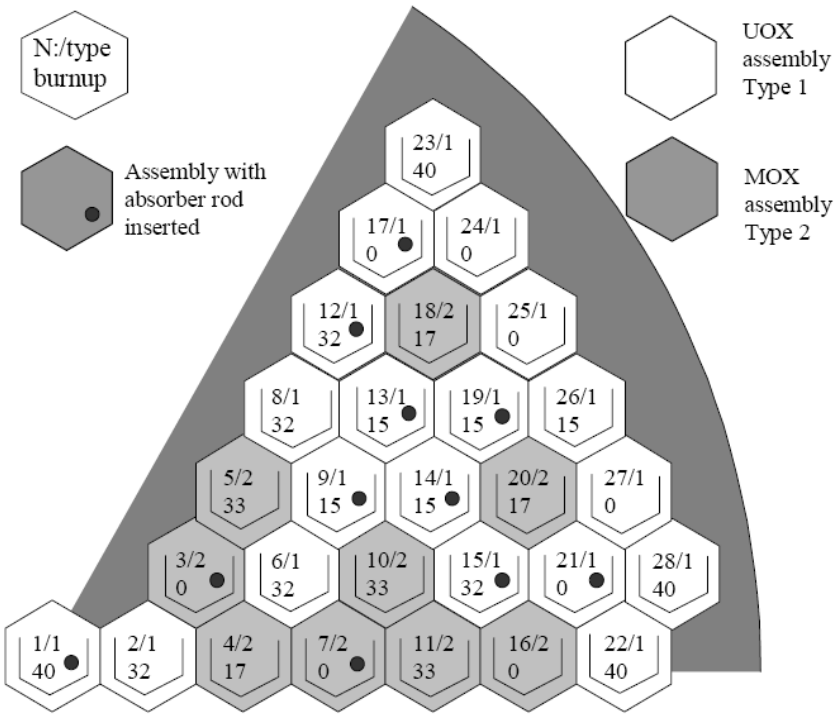

Fig. 5.3 – Core Map of the Benchmark Problem with 30% MOX Loading

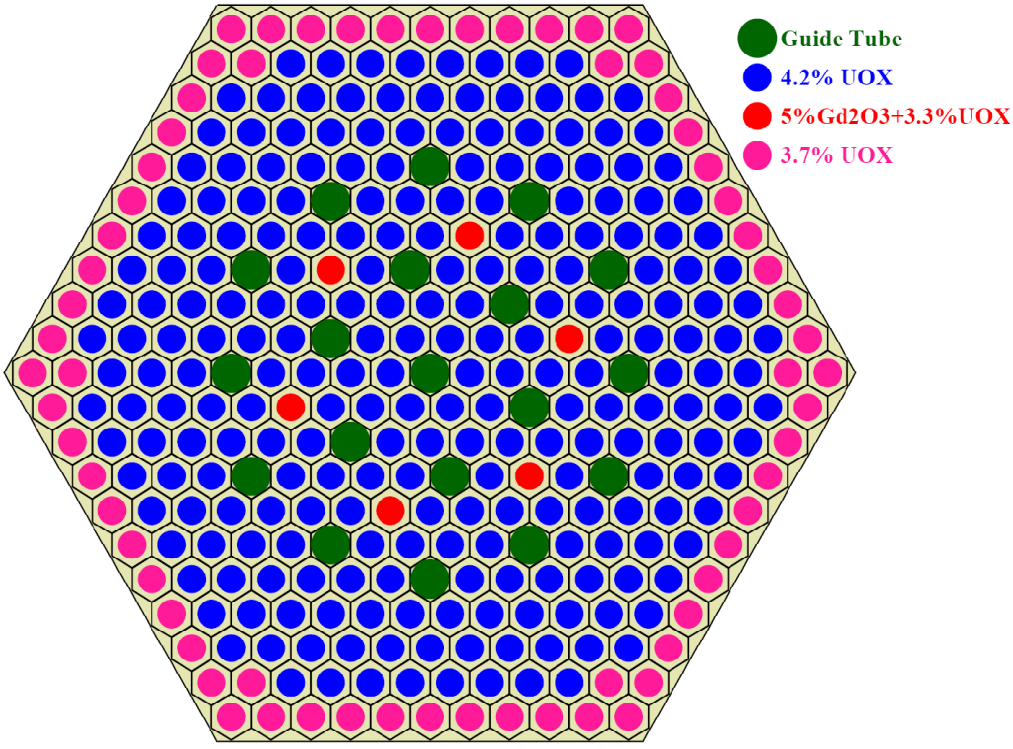

Fig. 5.4 – Graded UOX Fuel Assembly

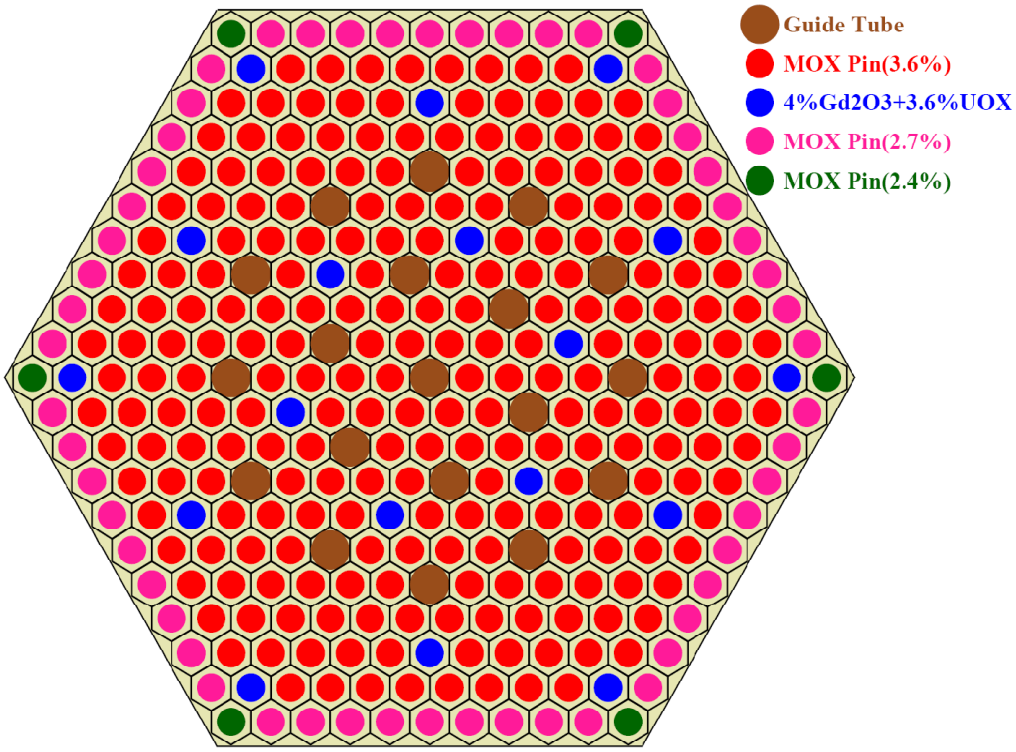

Fig. 5.5 – Graded MOX Fuel Assembly

5.2 Results and Discussion

5.2.1 HTTR Benchmark Results

The TRANPIN results for the HTTR benchmark in all rods in (ARI) condition are compared with benchmark results which are obtained using MCNP. The results reported here are obtained using a convergence criterion of 10^{-7} for multiplication factor and 10^{-5} for flux. The results are obtained using 32 azimuthal angles and a ray separation of 0.0396 cm. Gauss–Legendre quadrature is used for angular integration of collision probability integrals. The hexagonal lattice cells in each FA are divided into concentric circles. The resulting mesh structure for the lattice cell is shown in Fig. 5.6. The fuel region was divided into three regions of equal volume and outside graphite region was divided into eight regions of equal thickness. Beyond the regular hexagonal structure in the fuel blocks, the graphite structure is divided into

side and corner meshes. The geometrical details of these side and corner meshes is similar to that discussed in Section 3.2 of Chapter – 3, though in the present problem the outer cells are slightly larger than half / 1/3rd size cells.

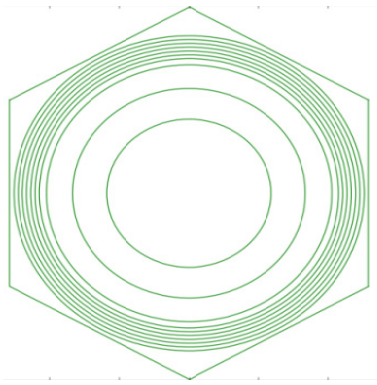

Fig. 5.6 – Mesh Division inside Single Hexagonal Lattice Cell

The modeling of control block in the present problem required special consideration due to the presence of 12.3 cm thick control rod present in the centre of control block as shown in Fig. 5.2 (b). For the purpose of mesh generation in the control block, first a regular hexagon grid is mapped on the control block as shown in Fig. 5.7 (a). It is seen that the control rod is spanning the seven central hexagonal cells. A new central hexagonal mesh boundary enclosing the central control block is therefore created. This is illustrated in Fig. 5.7 (b). The flat–to–flat width of the central hexagon mesh is three times the regular lattice pitch of fuel block in Fig. 5.2(a). The central control rod surrounded by graphite material in the central hexagon in the control block is divided into twelve concentric rings as shown in Fig. 5.7 (c). The graphite region in the central hexagon outside the control rod is radially divided into 18 zones as shown in Fig. 5.7 (c). The six surfaces of the central hexagon are split into eighteen surfaces for the purpose of one to one current coupling with the neighbouring cells which are alternately integral hexagons and 2/3rd hexagonal shapes as seen in Fig. 5.7(b). The new 2/3rd hexagonal shape is seen to be adjoining

the six corners of central hexagon. A typical mesh adjoining the left lower corner of central hexagon is shown in Fig. 5.8. This mesh has six surfaces and the graphite in this 2/3rd hexagonal mesh is divided into 16 fine triangular meshes. Similar 2/3rd hexagonal mesh shapes at other five corners of central hexagon are obtained by successive 60°rotation of Fig. 5.8. The discretization of graphite in control block beyond the regular hexagonal structure is similar to that of any fuel block. With this kind of development it is seen that TRANPIN code is capable to handle more than one regular hexagonal pitch/shape that may be present in the single assembly block.

The mesh structure in the removable and permanent reflector blocks is similar to the methodology discussed for fuel block.

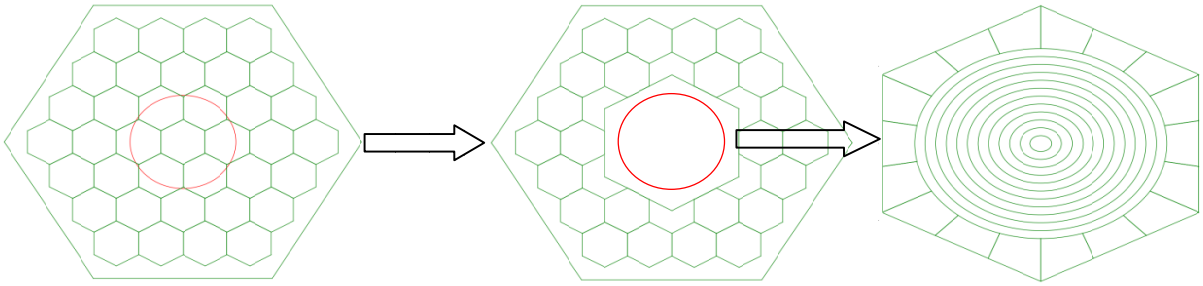

(a) (b) (c)

Fig. 5.7 – Modeling of Control FA

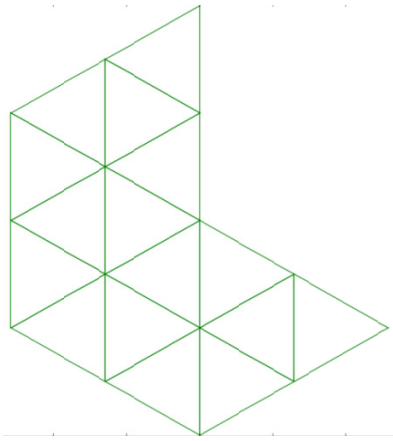

Fig. 5.8 – Mesh structure in the left lower neighbor of central hexagon

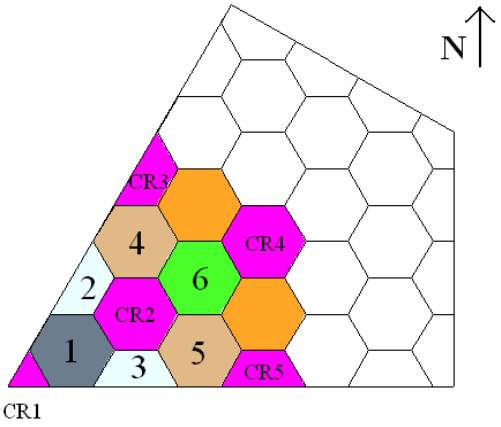

Fig. 5.9 – Numbering Scheme of Blocks in 1/6th Core

Table 5.2 gives the comparison of core eigenvalue obtained using TRANPIN with benchmark value. TRANPIN results are obtained by gradually increasing the order of angular flux expansion at the surfaces of distinct cells. The three results correspond to the DP0, DP1 and DP2 expansion as described in Section 2.4 of Chapter – 2. It is seen that the results obtained using DP2 expansion show the least deviation with benchmark result. The result with DP2 shows an absolute deviation of 0.91% w.r.t. the benchmark value. Table – 5.3 gives the block average fission density distribution for the 1/6th core obtained using the three angular flux expansions. The numbering scheme of blocks in the core and pins inside the blocks, as described in benchmark, is shown in Fig. 5.9. The block average fission density obtained using DP1 expansion shows closest matching with benchmark values. A maximum relative deviation of 0.93% is seen for block 5. The maximum values for DP0/DP2 expansion are seen to be 1.26% for block 6 and 1.02% for block 5 respectively. The %RMS deviation for DP0, DP1 and DP2 expansion is seen to be 0.775%, 0.419% and 0.463% respectively. The comparison of pin wise fission density distribution with benchmark values and the % relative deviation thereof for blocks 1 to 6 is given in Figs. 5.10 to 5.15 respectively. These fission densities are normalized to

the total number of fuel pins in the whole core (i.e. the total sum of fission densities is 990) as specified in benchmark [54]. For blocks 2 & 3, the benchmark provides fission density values for only half blocks due to the symmetry of the problem. These blocks shown in Figs. 5.11 & 5.12 have been completed using reflective symmetry. The relative standard deviations in benchmark fission densities for all blocks are between 0.0002 & 0.0003. The pin wise fission densities show satisfactory comparison with the benchmark results. The maximum relative deviation for all the blocks is less than 4%. The absolute maximum and minimum % relative deviations in the pin wise fission densities for the six blocks are 1.78%/0.1%, 2.45%/0.05%, 2.97%/0.02%, 3.1%/0.08, 3.9%/0.01%, 3.4%/0.05% respectively. It is observed that fission density for interior pins in the block, in general, shows a closer matching with benchmark results. The minimum %RMS deviation of 0.98% is seen for block 2 and maximum %RMS deviation of 2.39% is seen for block 6. The %RMS deviation for blocks 1, 3, 4 & 5 are seen to be 1.25, 1.24, 1.59 & 2.09% respectively.

Table 5.4 gives the comparison of maximum and minimum pin fission densities occurring in the core obtained using TRANPIN with benchmark values. The maximum fission density is seen at pin number 37 (if hexagonal locations are numbered from left to right and top to bottom in Fig. 5.2(a)) in block 2 in Fig. 5.11 whereas the minimum fission density occurs at pin number 14 in block 6 in Fig. 5.15. The % relative deviation in maximum and minimum fission density is seen as 2.45% and –2.53% respectively.

Table 5.2 – Comparison of k_{eff}

Core Configuration	Benchmark value	TRANPIN value			Δk		
		DP0	DP1	DP2	DP0	DP1	DP2
All Rods In	0.89623 ±0.00003	0.915417	0.910487	0.905359	0.019187	0.014257	0.009129

Table 5.3 – Block Averaged Fission Density Distribution in ARI

Block Number	Fuel Type	Benchmark	TRANPIN			% Deviation		
			DP0	DP1	DP2	DP0	DP1	DP2
1	1	1.023	1.036	1.030	1.030	-1.25	-0.68	-0.68
2	2	1.057	1.061	1.051	1.052	-0.38	0.57	0.47
3	2	1.058	1.062	1.051	1.051	-0.38	0.67	0.66
4	3	0.978	0.971	0.972	0.971	0.72	0.62	0.72
5	3	0.981	0.973	0.972	0.971	0.82	0.93	1.02
6	4	0.962	0.950	0.960	0.959	1.26	0.21	0.31
					% RMS Deviation	0.775	0.419	0.463%

Table 5.4 – Comparison of Maximum and Minimum Pin Fission Density

Core Configuration	Maximum pin fission density			Minimum pin fission density		
	Benchmark	TRANPIN	% Rel. Dev.	Benchmark	TRANPIN	% Rel. Dev.
All Rods In	1.181±0.02%	1.152	2.45	0.859±0.02%	0.881	–2.53

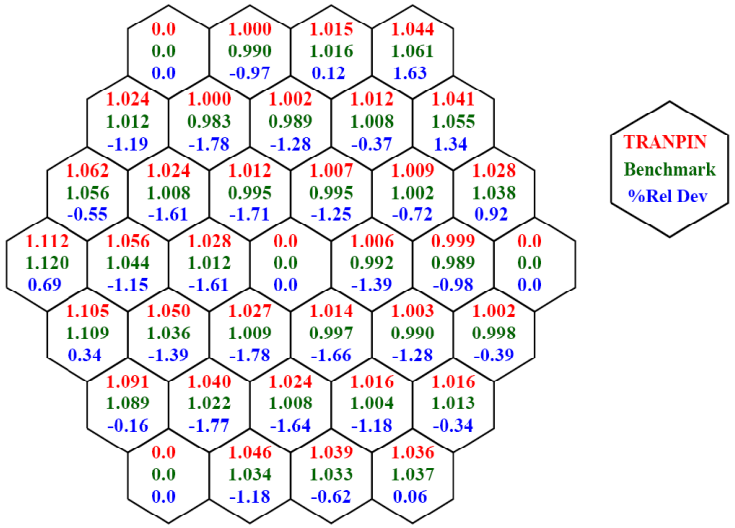

Fig. 5.10 – Fission Density Distribution in Block 1

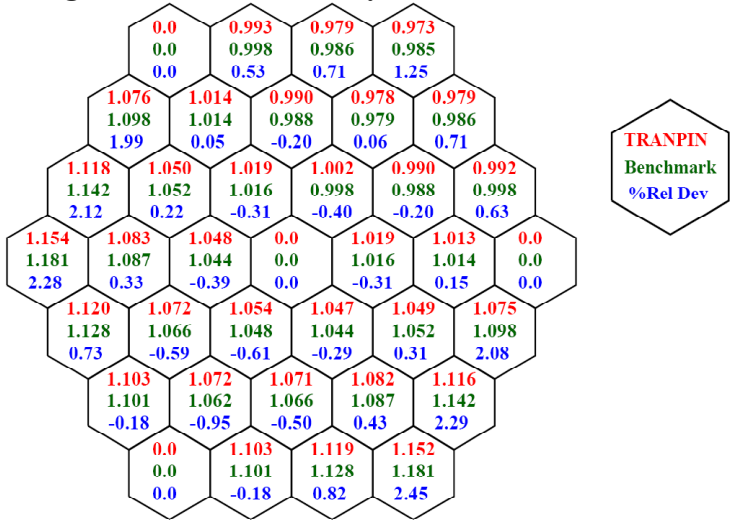

Fig. 5.11 – Fission Density Distribution in Block 2

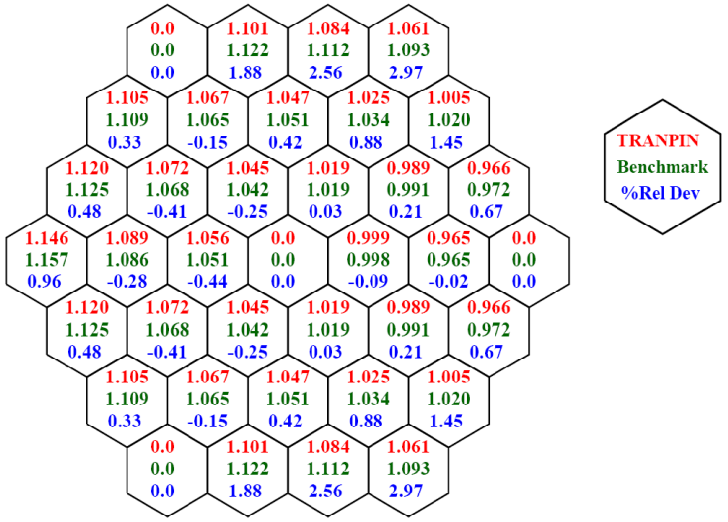

Fig. 5.12 – Fission Density Distribution in Block 3

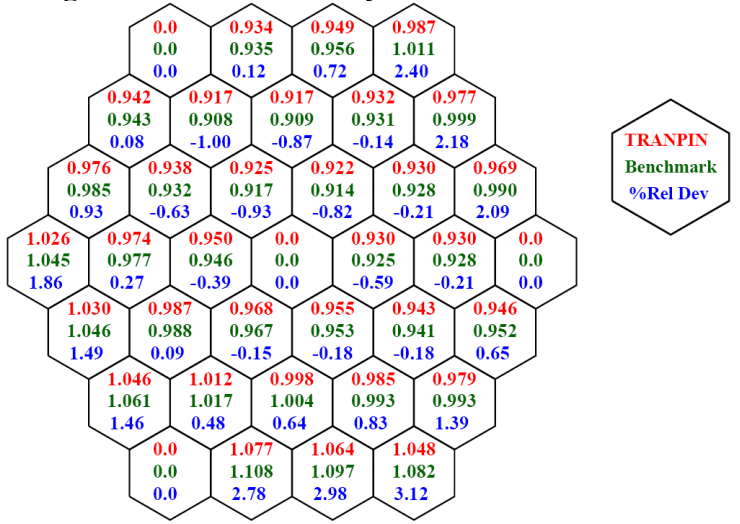

Fig. 5.13 – Fission Density Distribution in Block 4

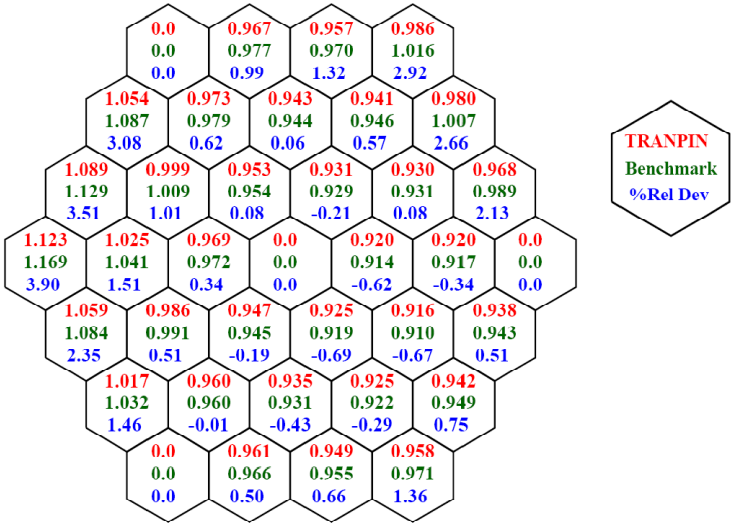

Fig. 5.14 – Fission Density Distribution in Block 5

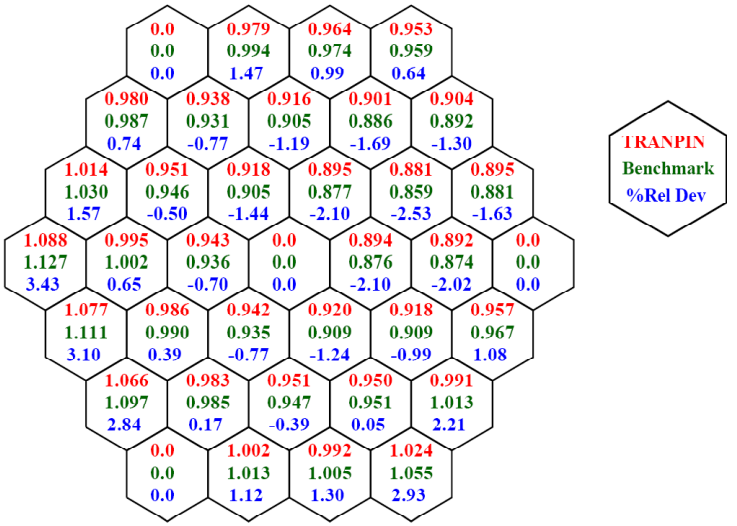

Fig. 5.15 – Fission Density Distribution in Block 6

5.2.2 OECD Benchmark

The benchmark problem lists a set of 6 operating states. The results presented here correspond to the working state S1 in all rods OUT condition. In this state the fuel and coolant temperatures are 1,027 K & 575 K respectively. The coolant has a boron content of 1,300 ppm.

5.2.2.1 Nuclear Data Used and Cross Section Preparation

Since the present problem specifies only the material composition of the required materials, the required macroscopic cross sections must be computed. The present calculation was done using a high temperature, ultra fine energy group library 'HTEMPLIB' based on JEFF-3.1 nuclear data library [31]. This library has cross section data for 185 nuclides in 172 energy groups in WIMS/D format as described in Section 3.5 of Chapter – 3. This library is traditionally used to perform lattice calculations such as the production runs of VVER lattice computations of Kudankulam NPP in Tamilnadu, India and other applications. The usage of this library to perform core calculations is new and not reported in literature to the best of our knowledge.

In order to compute the macroscopic cross sections, TRANPIN uses Stammler's model [51] to calculate self shielded cross sections. Equivalence relations are used for obtaining resonance self–shielded cross sections. In the WIMS libraries, the cross section in 47 resonance energy groups is tabulated in the form of resonance integral tables (RITs) for a set of background cross sections and temperatures. The background cross section for the problem under consideration is computed using the following formula

$$\sigma_i^b = \sum_{j \neq i} \frac{N_j \lambda_j \sigma_{pj}}{N_i} + \frac{\Sigma_e}{N_i}$$

where N_i is the isotopic density of the nuclide under consideration, λ_i is the Goldstein-Cohen parameter, σ_{pi} is the microscopic potential scattering cross section of that nuclide and Σ_e is the effective potential scattering cross section obtained using equivalence principles for treating the heterogeneous lattice as an equivalent homogeneous problem. Using this background cross section, the resonance cross sections (absorption and fission) are obtained by a linear interpolation of the RITs w.r.t. background cross section and $\sqrt{T}$ where T is fuel temperature in Kelvin. Mutual shielding for a mixture of resonance nuclides is treated in accordance with the procedures described by Stammler and Abbate [51]. For the burnable poison nuclide Gd, only five isotopes viz. ^{154}Gd, ^{155}Gd, ^{156}Gd, ^{157}Gd, ^{158}Gd are available in the HTEMPLIB library. The isotopes ^{152}Gd &^{160}Gd are not available. Since their absorption cross sections are negligible compared to those of ^{155}Gd or ^{157}Gd, the concentration of ^{152}Gd & ^{160}Gd given in benchmark specification were added to those of ^{154}Gd &^{158}Gd respectively. It is believed that this approximation would have negligible influence on the quality of results of the analysis.

5.2.2.2 Results of Analysis

The TRANPIN results for the OECD benchmark in S1 state are compared with benchmark results. Two Monte Carlo based evaluations obtained using MCNP and MCU provided in benchmark report [55] are selected for comparison. MCU uses a library named MCUDAT-2.1 whereas MCNP uses point data generated mainly from JEFF–2.2. Both of these libraries are in continuous energy format. The results reported here are obtained using a convergence criterion of 10^{-7} for multiplication factor and 10^{-4} for flux respectively. The results are obtained using 32 azimuthal angles and a ray separation of 0.01 cm. Gauss–Legendre quadrature is used for angular integration of collision probability integrals. The mesh discretization of this problem is a daunting task due to the large size of the problem. Fig. 5.16

describes the discretization of the problem. The solution domain considered 46 FAs (28 FAs in core + 18 FA locations in reflector) as shown in Fig. 5.16 (a). The mesh structure in each FA of Fig. 5.16 (a) is shown in Fig. 5.16 (b). The regular hexagonal, side and corner lattice cell discretization in each FA of Fig. 5.16 (b) is shown in Figs. 5.16 (c, d and e) respectively. Each hexagonal fuel pin in Fig. 5.16 (c) is subdivided into three fuel, one clad and seven coolant regions. Tables 5.5 and 5.6 give the comparison of k_{eff} obtained by TRANPIN with the benchmark results. TRANPIN results are obtained by using DP0 (Table 5.5) and DP1 (Table 5.6) expansion of angular flux on the surfaces of distinct lattice cells. It was not possible to run the present problem with DP2 expansion due to huge memory requirements discussed in the end of this section. It is seen that the DP0 result show a deviation of 4.44 mk from MCNP and 8.44 mk from MCU. The results show a good comparison with DP1 expansion. The results show a deviation of 1.53 mk from the MCNP and 5.53 mk from the MCU results where the deviation in mk is calculated using the following expression

$$\Delta\rho\ (in\ mk) = \left(\frac{1}{k_{Ref}} - \frac{1}{k_{TRANPIN}}\right) \times 1000.$$

It should be noted that the present benchmark is very challenging and tests the applicability of the codes to the problems of practical interest. In the present problem, the strong flux gradients are prevailing between LEU and MOX assemblies and strong heterogeneities are present within the fuel assemblies. Due to this, the usage of DP0 expansion is inadequate to predict the core characteristics. This will become clearer in the comparison of fission density distribution. To evaluate the assembly and pin wise fission density distribution, it is very important to model the reflector properly in the core. In the present calculation, two additional layers of each one assembly pitch in the reflector region were considered beyond the active core.

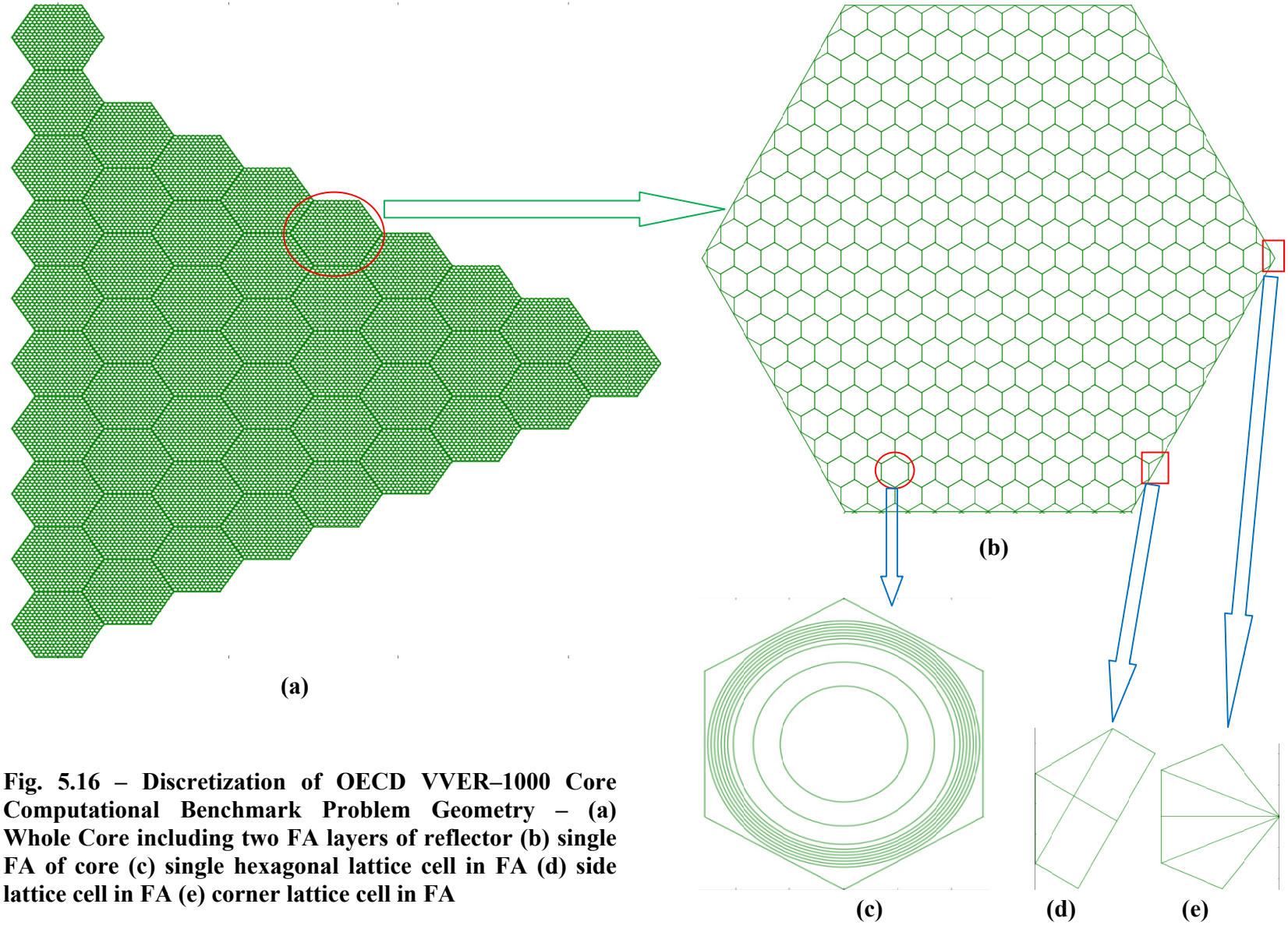

Fig. 5.16 – Discretization of OECD VVER–1000 Core Computational Benchmark Problem Geometry – (a) Whole Core including two FA layers of reflector (b) single FA of core (c) single hexagonal lattice cell in FA (d) side lattice cell in FA (e) corner lattice cell in FA

The reflector structure given in the benchmark was mapped on the detailed lattice structure of these two hexagonal layers. The lattice cells having 100% water, 100% steel or a combination of steel and water in these FA layers were identified. Figs. 5.17 and 5.18 give the comparison of assembly average fission rate distribution obtained using DP0 and DP1 expansion with MCU & MCNP results respectively. The assembly average fission reaction rates should be averaged over the hexagon with a pitch of 23.6 cm [55]. The following normalization rule is applied to the assembly average fission rate distribution [55]. The fission rate values R(I), I=1,28 satisfy

$$R(1) + 6 * \sum_{I=2}^{28} R(I) = 163$$

where 163 is the number of fuel assemblies in the reactor core and 6 is the number of 60° angles of symmetry. The assembly average fission reaction rates obtained using DP0 expansion show a very large deviation when compared with the reported Monte Carlo evaluations. This is due to the deep flux depression at the core centre when DP0 expansion is used. The assembly averaged flux distribution obtained using DP0 and DP1 expansion is shown in Fig. 5.19. As seen in Fig. 5.19, the flux values obtained using DP0 are higher in the outer FAs of the core as compared to DP1 values but lower in the internal FAs. The detailed cell averaged 172nd group flux in central assembly obtained using DP0 and DP1 is shown in Fig. 5.20. In the central assembly, both the assembly averaged and cell averaged pin–by–pin 172nd group flux values obtained using DP0 expansion are about 1/10th to the values obtained using DP1 expansion. Since most of the heterogeneous MOX assemblies are present in the interior of the core (Fig. 5.3), the isotropic flux (DP0) model is not able to predict the prevailing flux gradients and the flux peaking shifts to outer peripheral LEU assemblies. The prediction of flux gradients in core is improved only when DP1 expansion is used. The fission density distribution obtained using DP1

expansion, therefore, show a satisfactory comparison. The results using DP1 expansion show a maximum relative deviation of 2.8% w.r.t. MCNP & 2.6% w.r.t. MCU for FA N08. The %RMS error is seen to be 2.6% with MCNP and 2.2% with MCU values.

The benchmark provides detailed pin–by–pin fission density distribution for three assemblies N03, N21 & N27 shown in Fig. 5.3. Two of these assemblies are LEU (N21 & N27) and one is MOX (N03). All the chosen assemblies are fresh. The pin wise fission densities are normalized to total number of locations in the fuel assembly i.e. 331 [55]. Figs. 5.19 to 5.21 give the comparison of fission density distribution for these assemblies. The estimated relative statistical uncertainty in benchmark values obtained by MCNP and MCU is 1%. The pin–by–pin fission density comparison is seen to be satisfactory. It is seen that the TRANPIN values show a closer matching with MCU for assemblies N03 & N27 whereas for N21, results are closer to MCNP. The %RMS error in MCU results is 1.7%, 2.8% & 1.9% for assemblies N03, N21 & N27 respectively. These values for comparison with MCNP results are 2.3%, 1.8% and 2.7% respectively.

Table 5.7 compares the pin fission densities with maximum % relative deviation w.r.t MCU and MCNP for the three fuel assemblies. It is seen that the maximum deviation pins are different both for MCU and MCNP in the three assemblies. This is because there is a considerable difference in the two Monte Carlo evaluations of MCU and MCNP provided in the benchmark report. It is seen that the maximum absolute relative deviation in MCNP values w.r.t. MCU is 3.5%, 3.8% and 4.1% for assemblies N03, N21 and N27 respectively [55]. In TRANPIN calculation, for assembly N03, the maximum relative deviation pin occurs at location 26 (if hexagonal locations are numbered from left to right and top to bottom in Figs. 5.4/5.5) with relative deviation of –5.02% for MCU. This location shifts to pin number 175 with 4.62%

relative deviation in MCNP comparison. Similarly for assembly N21, the maximum deviation pin occurs at location 314 for MCU and 311 for MCNP with relative deviations of –3.73% and –3.05% respectively. For assembly N27, the maximum deviation pins are seen at locations 196 and 35 for MCU and MCNP respectively. It is seen that all these locations are either at the periphery of the assembly or one to two layers away from periphery of fuel assembly.

The present benchmark is huge in size. Since TRANPIN considers the mesh discretization to single lattice cell level, the code has huge memory requirements. The present problem has been simulated with 46 assembly locations (28 fuel assemblies in the $1/6^{th}$ core + 18 reflector assemblies). Each of this assembly has 397 lattice cells (331 regular hexagonal cells + 60 side cells + 6 corner cells). Each hexagonal cell is further divided into 11 regions as discussed in the beginning of this section. Each hexagonal cell has 6 surfaces. Each side and corner cell is divided in 4 regions. These cells have 5 surfaces. The energy domain in the present problem is divided in 172 energy groups. Therefore, the flux and current unknowns required for the present problem can be estimated as follows

number of flux unknowns = 46 * (331*11+66*4) *172 = 3,08,96,360

number of current unknowns (DP0) = 46 * (331*6+66*5) *172 *1 = 1,83,24,192

number of current unknowns (DP1) = 46 * (331*6+66*5) *172 *3 = 5,49,72,576

number of current unknowns (DP2) = 46 * (331*6+66*5) *172 *6 = 10,99,45,152

As seen from above, with increasing angular flux expansion, though the scalar flux unknowns remain constant, the memory requirement for current components, however, increases significantly. Since TRANPIN, presently, is running in serial mode, it was not possible to use DP2 expansion of angular flux for the present problem.

Table 5.5 – Comparison of Core k_{eff} with DP0 Expansion

Core Configuration	Benchmark value		TRANPIN value	Δk w.r.t.	
	MCNP	MCU		MCNP	MCU
S1 State (All Rods OUT)	1.03770 ±0.007%	1.03341 ±0.013%	1.042506	0.004806	0.009096

Table 5.6 – Comparison of Core k_{eff} with DP1 Expansion

Core Configuration	Benchmark value		TRANPIN value	Δk w.r.t.	
	MCNP	MCU		MCNP	MCU
S1 State (All Rods OUT)	1.03770 ±0.007%	1.03341 ±0.013%	1.039354	0.001654	0.005944

Table 5.7 – Comparison of Maximum Deviation Fission Density Pin

Fuel Assembly			
	N03	N21	N27
Maximum Deviation for MCU			
TRANPIN	1.046	0.891	0.747
MCU	0.996	0.858	0.787
%Rel. Dev.	-5.02	-3.73	5.08
Pin Number	26	314	196
Maximum Deviation for MCNP			
TRANPIN	0.330	0.878	1.414
MCNP	0.346	0.852	1.364
%Rel. Dev.	4.62	-3.05	-3.67
Pin Number	175	311	35

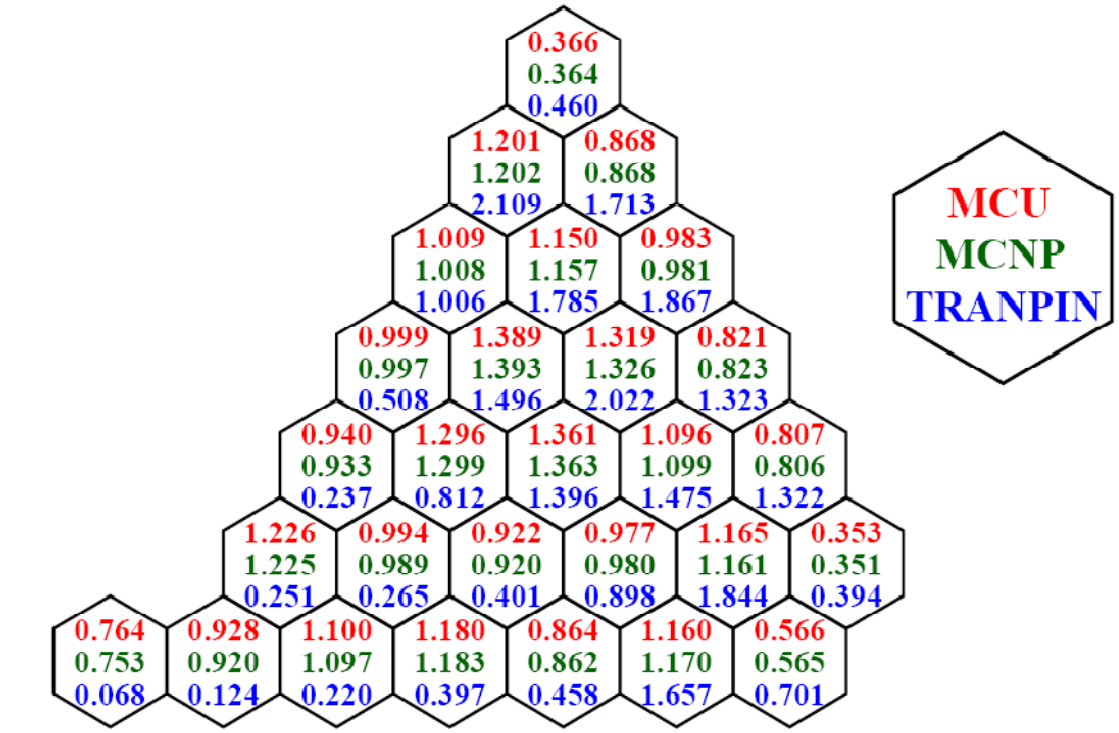

Fig. 5.17 – Assembly Average Fission Density Distribution with DP0 expansion

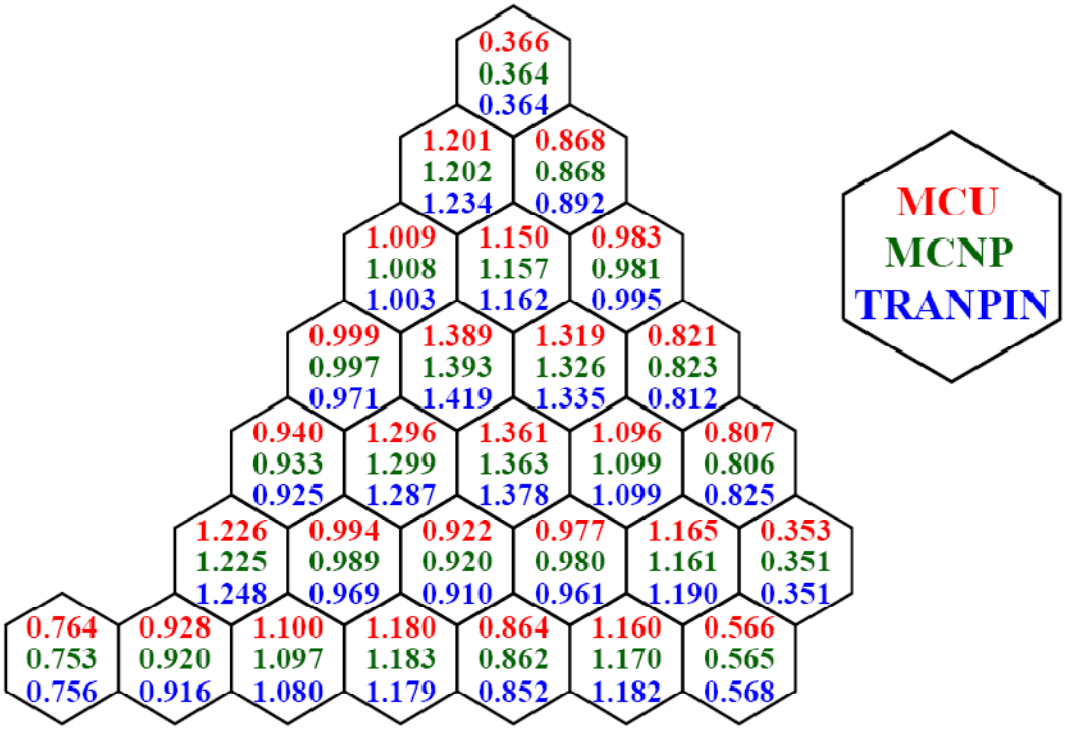

Fig. 5.18 – Assembly Average Fission Density Distribution with DP1 expansion

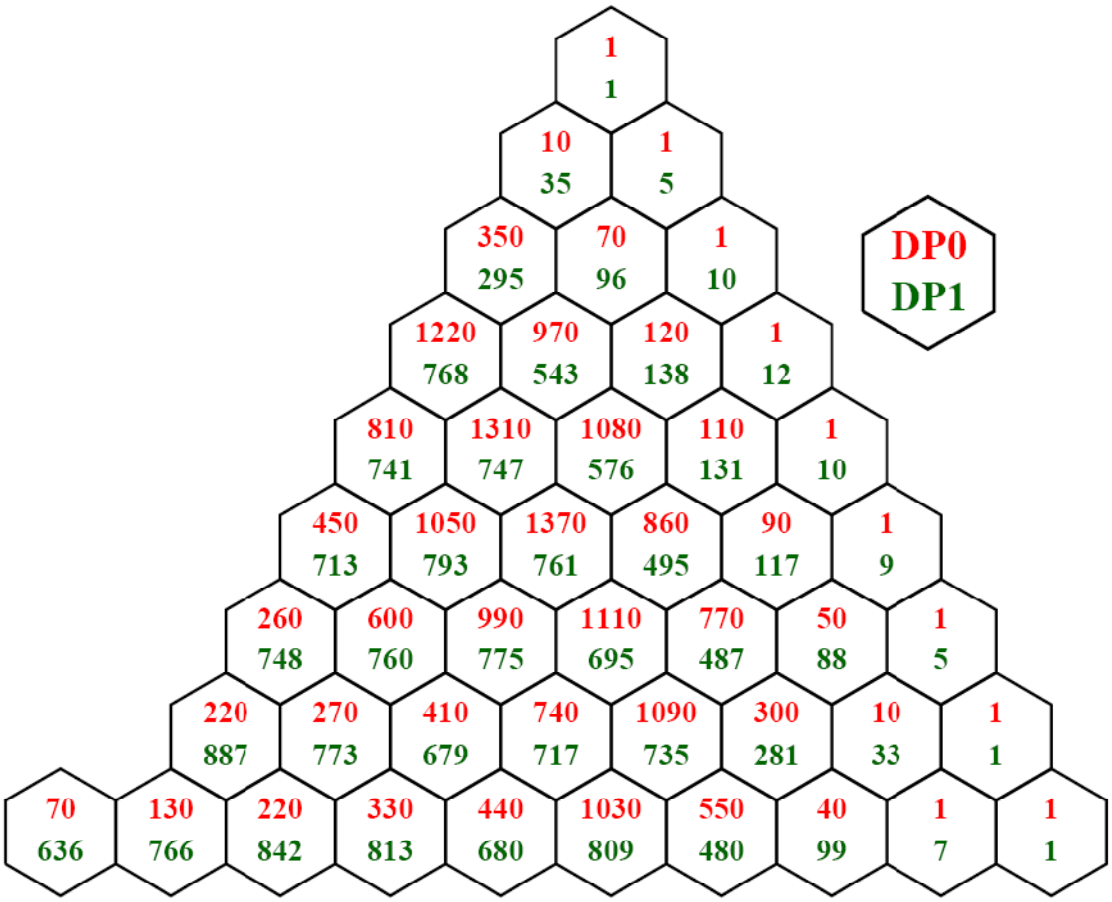

Fig. 5.19 – Assembly Average Flux Distribution in the core with DP0/DP1 expansion

(Flux Distribution Multiplied by 10^6 for printing purpose)

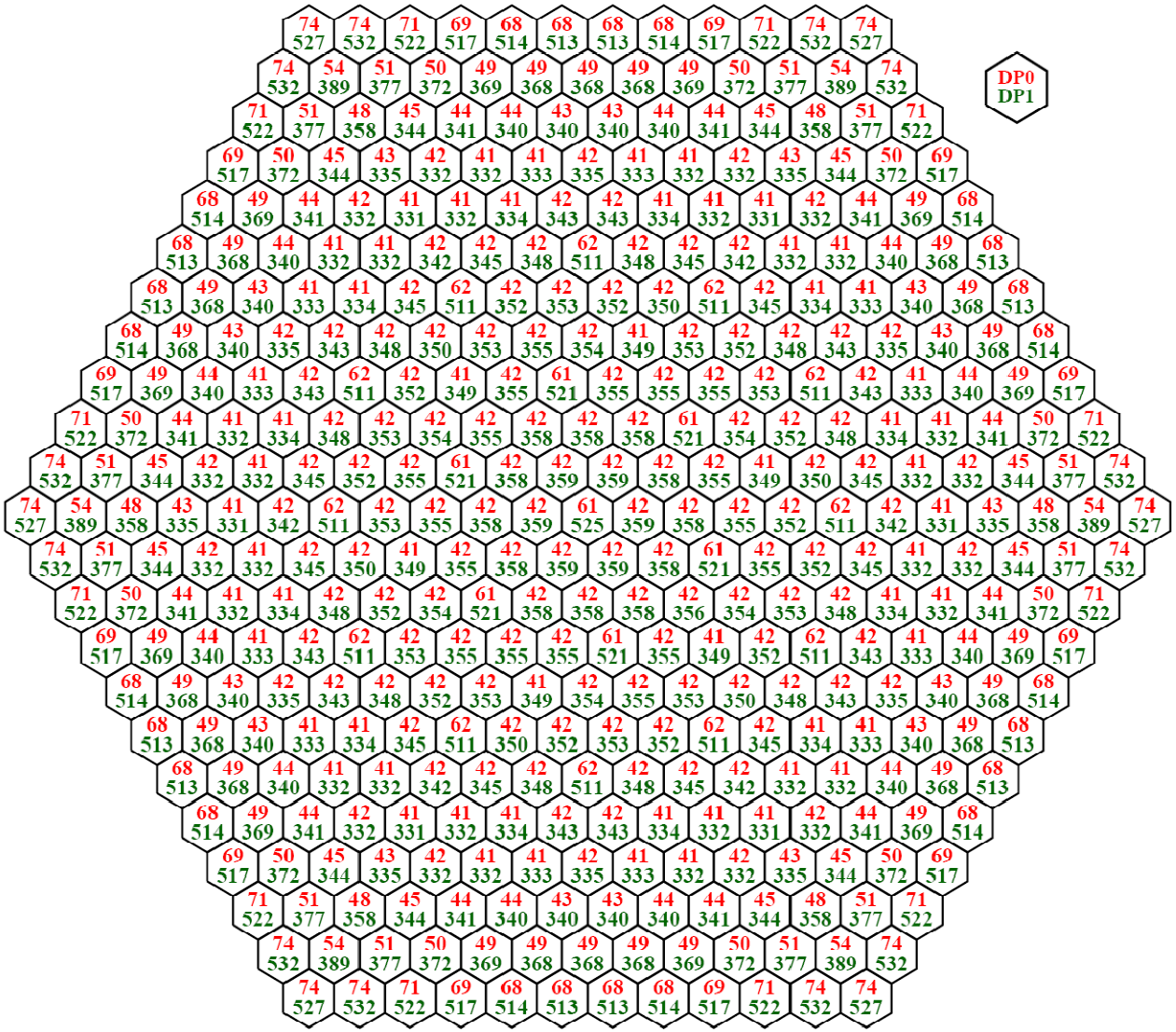

Fig. 5.20 – Cell Averaged Flux Distribution in 172nd Group in Central Assembly

(Flux Distribution Multiplied by 10^9 for printing purpose)

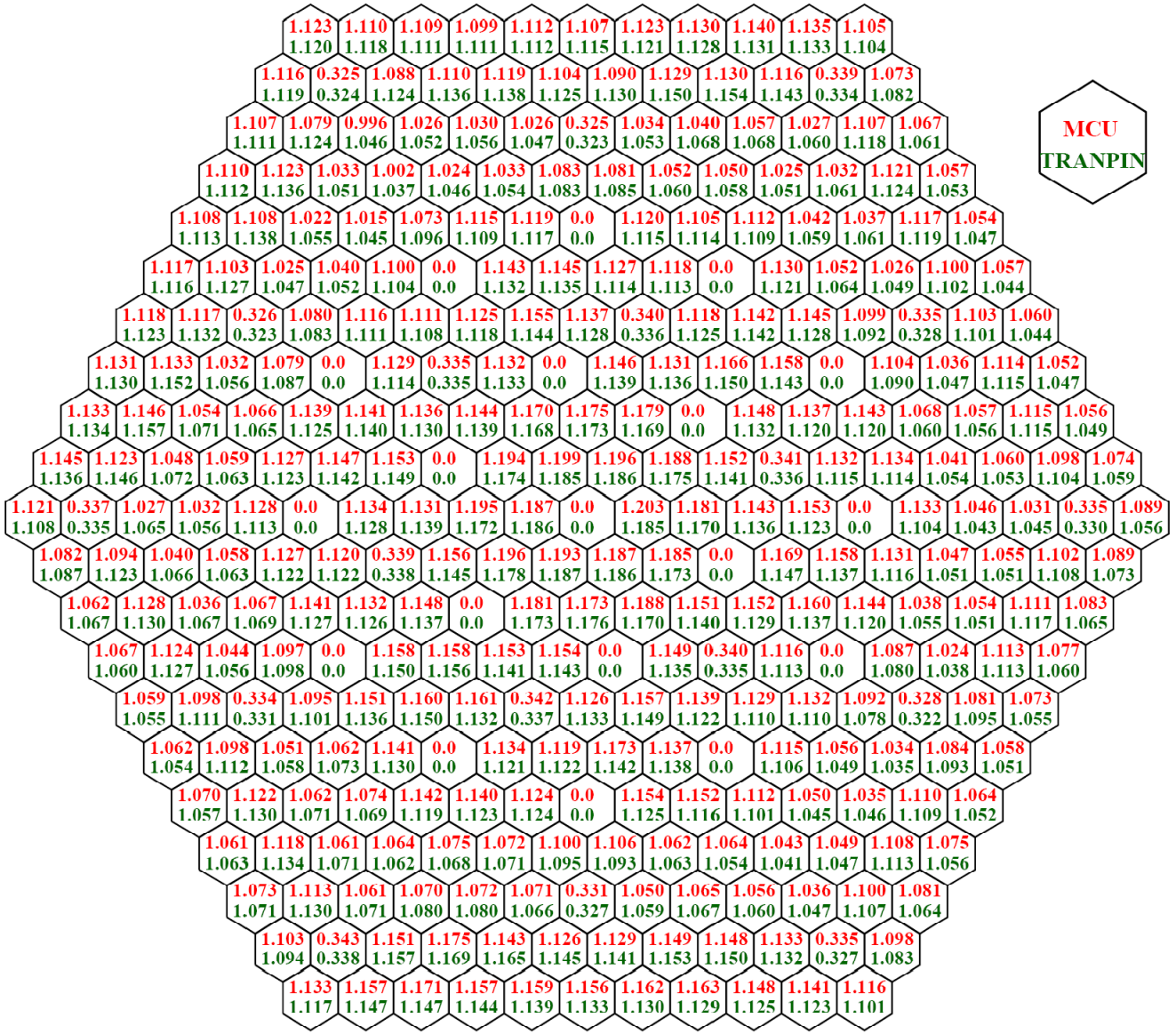

Fig. 5.21a – Comparison of Pin-by-pin Fission Density Distribution for Assembly N03 with MCU

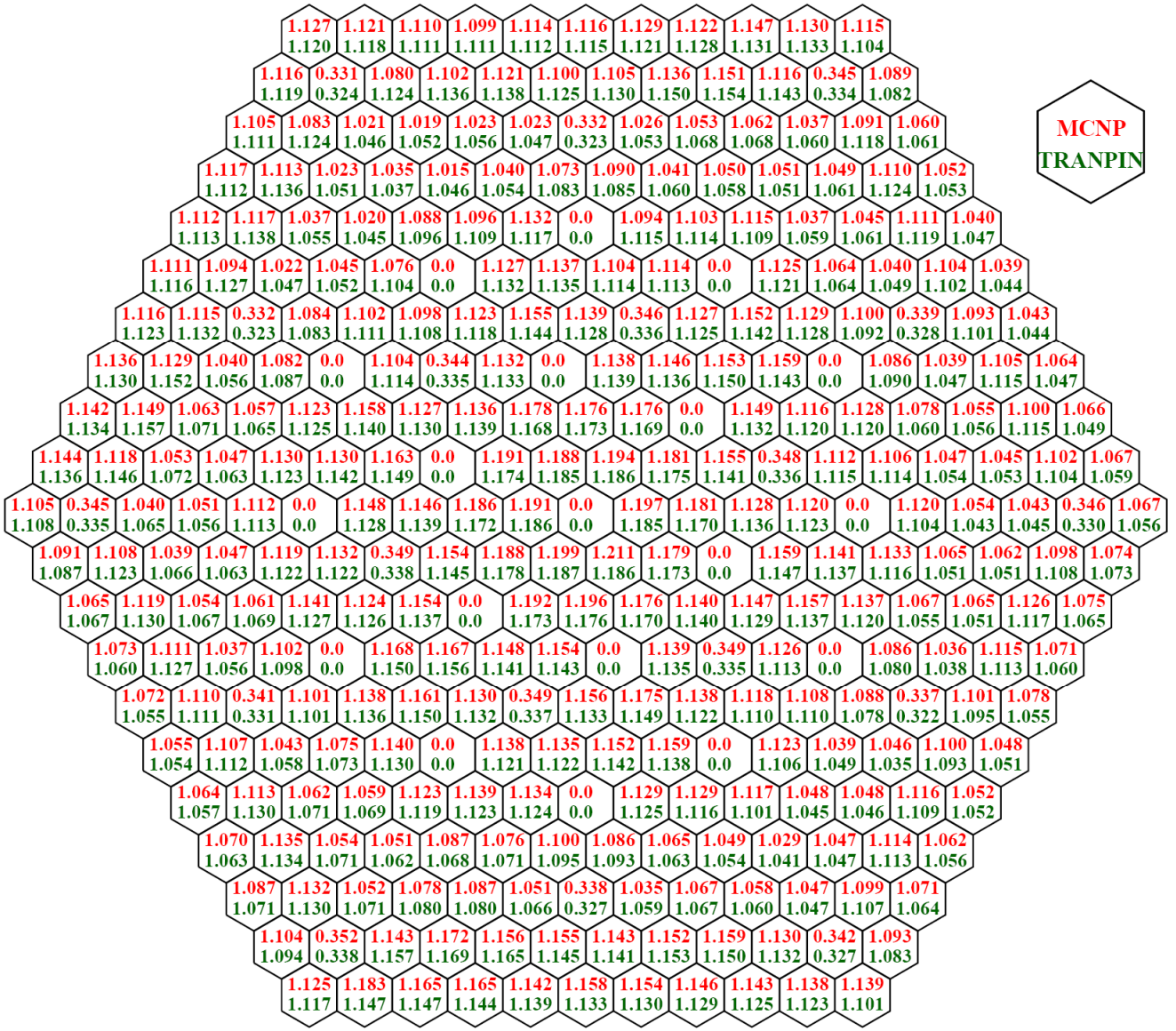

Fig. 5.21b – Comparison of Pin-by-pin Fission Density Distribution for Assembly N03 with MCNP

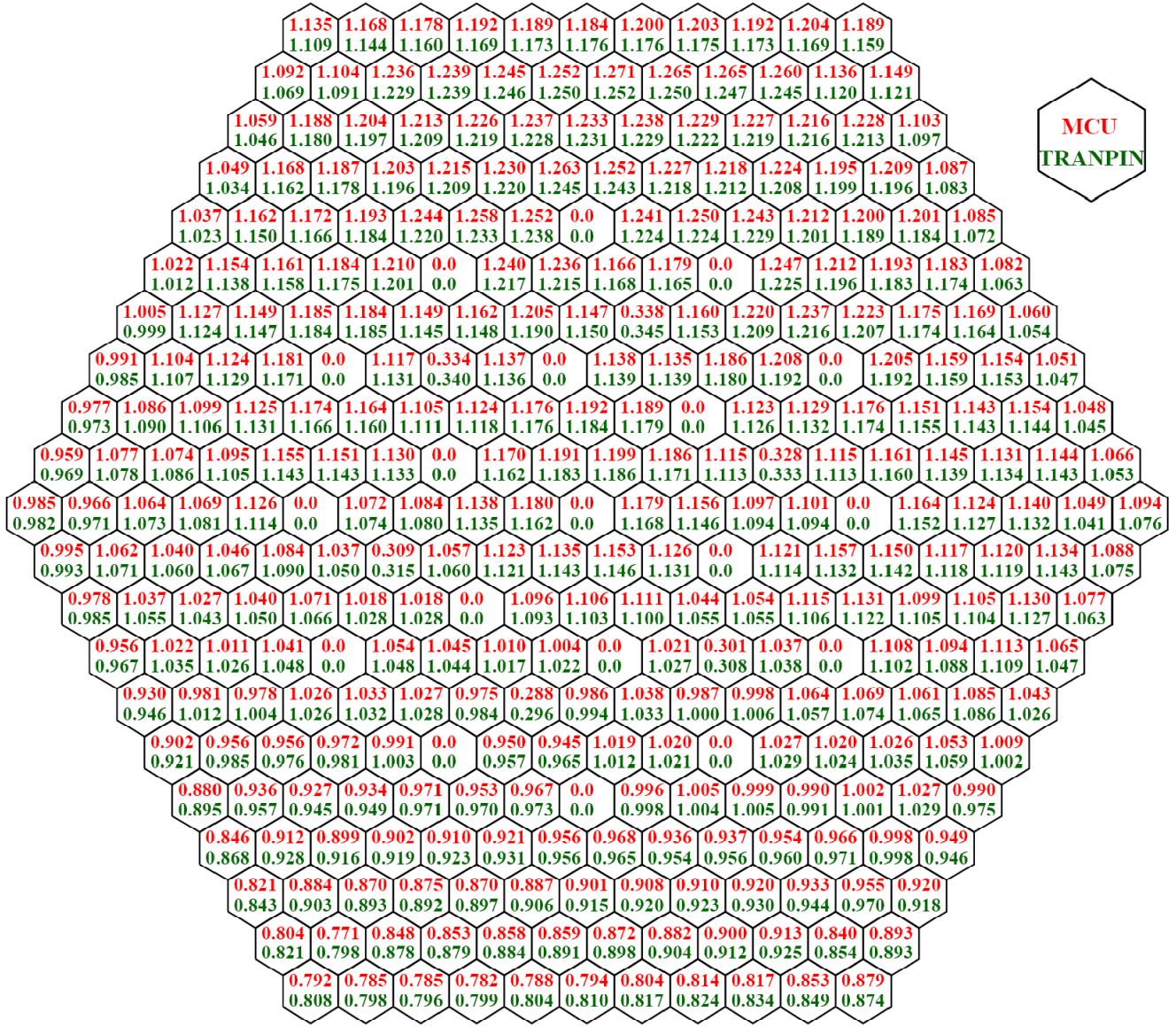

Fig. 5.22a – Comparison of Pin-by-pin Fission Density Distribution for Assembly N21 with MCU

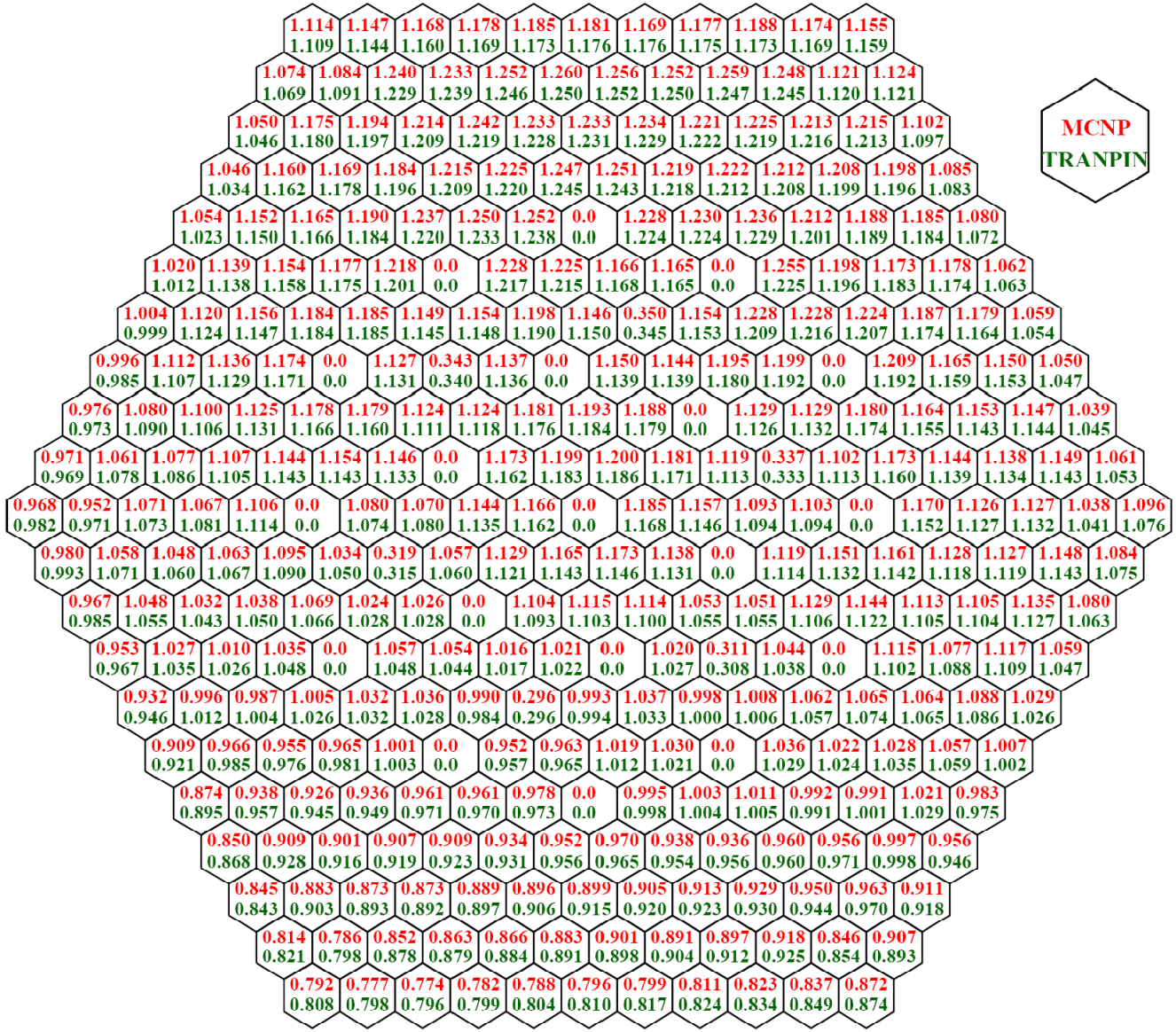

Fig. 5.22b – Comparison of Pin-by-pin Fission Density Distribution for Assembly N21 with MCNP

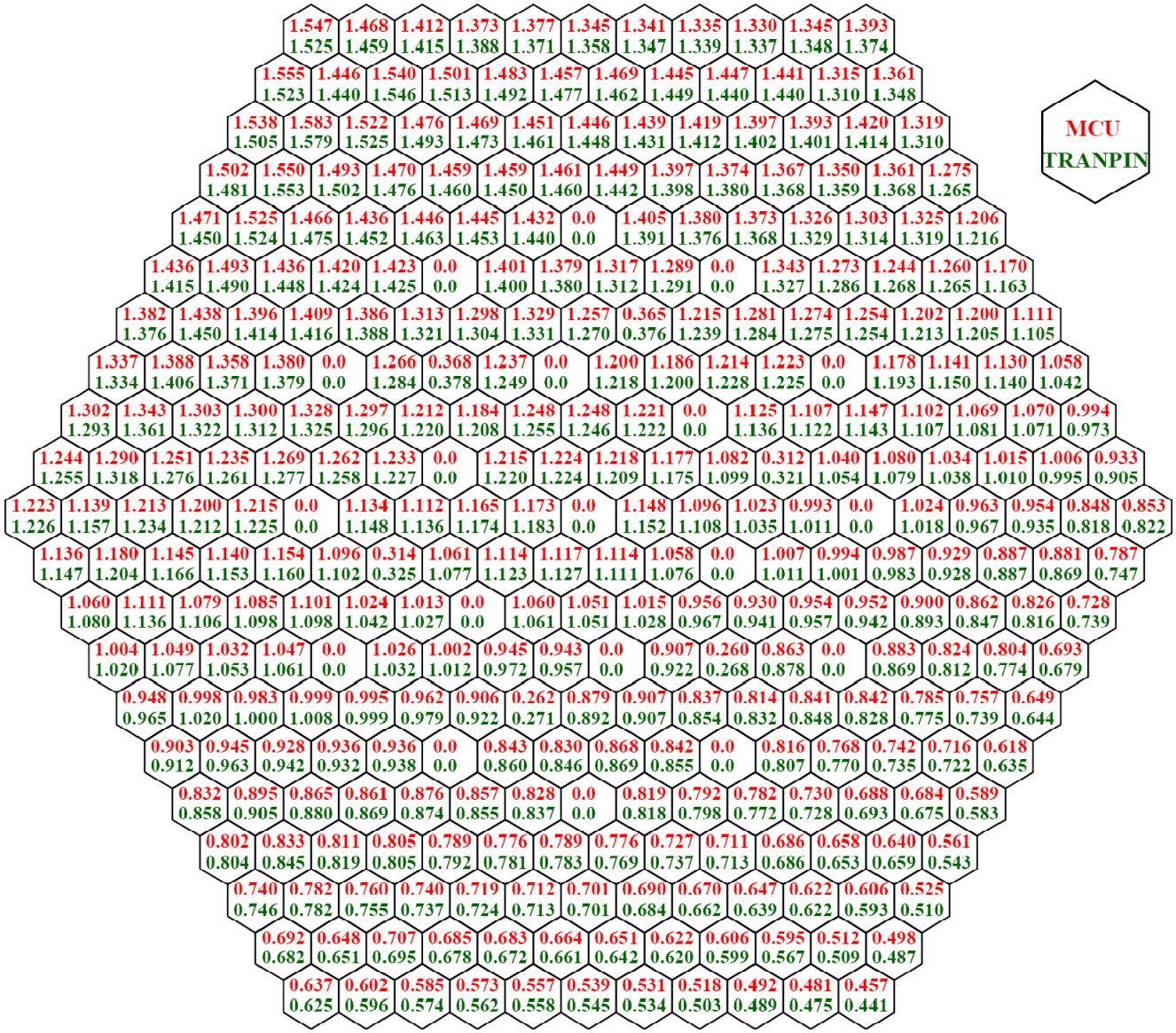

Fig. 5.23a – Comparison of Pin-by-pin Fission Density Distribution for Assembly N27 with MCU

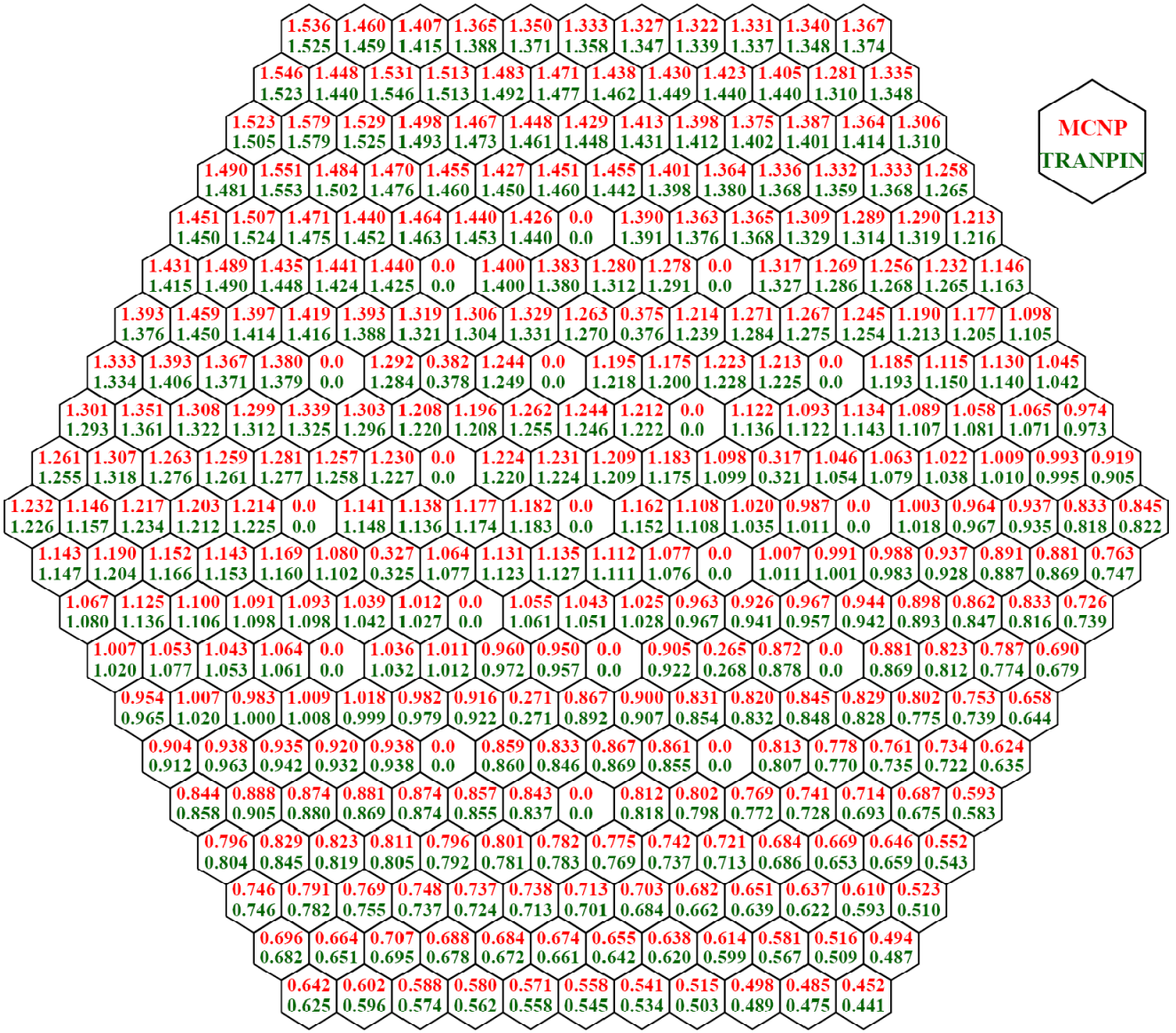

Fig. 5.23b – Comparison of Pin-by-pin Fission Density Distribution for Assembly N27 with MCNP

5.3 Summary

A whole core transport theory code TRANPIN in 2D hexagonal geometry has been developed. The code performs the full core calculation, without homogenizing the various lattice cells present in the FAs, in multi group formalism. The code TRANPIN uses the interface current method based on 2D collision probability to solve the transport equation for the whole core problem. The individual cells in the FA are subdivided into finer regions. The coupling of cells within an assembly and inter assembly coupling is achieved using interface currents. The incoming/outgoing angular flux at the lattice cells interface is expanded in P_N functions. The expansion is limited to P2. Albedo boundary condition is applied at the outermost surfaces of the cells. TRANPIN is used to study two heterogeneous benchmark problems *viz*. a simplified HTTR benchmark problem and the OECD VVER–1000 MOX Core Computational Benchmark. The eigenvalue for the core, assembly averaged and detailed pin–by–pin fission density distributions compare well with the reported Monte Carlo values for the two problems. The OECD problem is studied using ultra fine 172 energy group cross section library in WIMS format. Transport modeling by 2D CP method of the whole core without homogenizing any sub regions and with ultra fine energy groups is a highly sophisticated computational method and can be used to validate other production codes based on multistage homogenization and diffusion theory. When a parallel processing is implemented, the 2D CP method itself can assume a role of production code.

CHAPTER – 6

SUMMARY AND FUTURE WORK

1.1 Summary and Conclusion

The growing Indian nuclear power program will include the advanced Gen–III or III+ reactors. The challenging physics designs of these reactors require the development of state of the art core physics simulation methods. The availability of computational processing power has made the whole core pin–by–pin calculation as the next generation calculation methodology employing higher order transport methods. As part of this research work, a whole core pin–by–pin calculation code TRANPIN has been developed which is solely based on transport theory. TRANPIN solves the large scale whole core problem in 2D hexagonal geometry, using interface current method based on 2D collision probability in multigroup formalism, directly without prior homogenization using any lattice transport codes. The two step process explained in Chapter 1 has been reduced to a one–step simulation method and thus a greater degree of accuracy in simulating complex heterogeneities. The present code divides each lattice cell location in the fuel assembly (FA) into finer regions. Here the term 'lattice cell' refers to structured meshes of single regular hexagonal pincell in the fuel assembly (Fig. 3.2 of Chapter–3) or the unstructured meshes appearing at the periphery of fuel assembly (Figs. 3.3 and 3.4 of Chapter–3). The subdivided regions inside the lattice cell are connected using the 2D collision probabilities. The coupling of lattice cells within the assembly and assembly to assembly coupling is achieved using interface currents. The interface currents are obtained by expanding the angular flux leaving or entering the lattice cell surface into double orthonormal P2 (DP2) polynomials. The detailed mathematical foundation of interface current method incorporated in TRANPIN is described in detail in Chapter–2.

The methodology used in TRANPIN was tested for a single lattice assembly cell in hexagonal geometry. This was required as the implementation and validation of burnup characteristics with DP2 approximation for a single lattice assembly is not available in literature. The method was incorporated in lattice burnup analysis code VISWAM. Initially the TRANPIN code was benchmarked against a simplified heterogeneous HTTR benchmark problem. The pincell and assembly problems in the HTTR benchmark for seven enrichments were analyzed using six group macroscopic cross section provided in the benchmark. The results show a good agreement with a maximum error of 0.01% in k_∞ for single lattice cell for all the enrichments specified in the benchmark problem. For the FA calculation, a maximum error of (–0.182%/–0.176%/–0.168%) w.r.t. benchmark in k_∞ is obtained for first enrichment with DP0/DP1/DP2 expansion whereas the error for all other enrichments was seen within ±0.08%. The fission density showed an excellent comparison with benchmark results. The RMS error in the fission density distribution was 0.13%. The results are presented in Chapter–3.

The burnup strategy for DP2 model used in VISWAM code was validated using the theoretical Computational Benchmark of VVER–1000 OECD LEU and MOX FA. First, the effect of flux anisotropy on eigenvalue and fission density distribution of FA was studied. The k_∞ obtained by using higher order flux anisotropy showed an improved matching with reference MCNP result. The results obtained using P1 anisotropy show an improvement of around 4 mk in k_∞ as compared to P0 values and 0.5 mk using P2 anisotropy w.r.t. P1 values. The fission density distributions obtained using DP0, DP1 & DP2 expansion were compared with the quoted MCNP values. The %RMS deviation in fission densities for three cases is seen to be 1.03%, 0.549% & 0.462%. The minimum RMS deviation was seen for results with P2 expansion. The fission density distribution, in general, shows a good comparison with

MCNP results. The multiplication factor with burnup, fission density distribution and cell averaged isotopic densities were compared and are discussed in detail in Chapter–3. The results obtained using DP2 expansion show least deviation from benchmark mean values. The reactivity loads of (Xe, Sm) and isothermal temperature show an improved prediction by DP1/DP2 models.

The burnup model applied to single FA calculation using DP2 expansion showed a satisfactory performance. The various reactivity effects and isotopic densities predicted compared well with the benchmark results as a function of burn up. It is recommended to extend and use this model for performing the whole core calculation in 2D/3D geometry.

The interface current method was applied for whole core pin–by–pin calculation after gaining confidence at the lattice level. TRANPIN discretise the whole core 2D problem down to every single lattice cell level with fine subdivisions of each material region. The lattice cell division, spatial discretisation of whole core in using fine meshes, the numbering scheme of the meshes, connectivity of the meshes in the assembly and assembly to assembly coupling is given in Chapter–4. The iteration scheme adopted for the solution method is presented in Chapter–4.

The code TRANPIN has been applied to two core level 2D benchmark problems i) a heterogeneous simplified high temperature engineering test reactor (HTTR) benchmark problem and ii) OECD VVER–1000 MOX Core Computational Benchmark. The detailed results are discussed in Chapter–5. The HTTR problem is solved using the six group macroscopic cross sections provided in the benchmark. TRANPIN results were obtained using the DP0, DP1 and DP2 expansion. It is seen that the results obtained using DP2 expansion show the least deviation with benchmark result. The result with DP2 shows an absolute deviation of 0.91% w.r.t. the benchmark value. The block average fission density

compares well and shows a maximum relative deviation of 1.02% for one block. The %RMS deviation is seen to be 0.463%. The pin–by–pin fission densities show satisfactory comparison with the benchmark results. The maximum relative deviation for all the blocks is less than 4%. The maximum %RMS deviation in pin–by–pin fission densities was seen as 2.39%.

The OECD benchmark is analyzed using ultra fine energy discretization with WIMS library in 172 energy groups. Stammler's model for treating self shielded cross sections is used in TRANPIN to calculate the cross sections in resonance energy groups. The calculation was performed using DP0 and DP1 expansion and compared with two Monte Carlo calculations of MCNP and MCU. It is seen that the DP0 result show a deviation of 4.44 mk from MCNP and 8.44 mk from MCU in core k_{eff}. The results with DP1 expansion show a deviation of 1.53 mk from the MCNP and 5.53 mk from the MCU. It was seen that the DP0 model could predict the eigenvalue within the acceptable limits but it grossly fails to predict assembly average fission density distribution. The results obtained using DP1 expansion show a satisfactory comparison. The results obtained using DP1 expansion show a maximum relative deviation of 2.8% w.r.t. MCNP & 2.6% w.r.t. MCU for FA N08. The %RMS error is seen to be 2.6% with MCNP and 2.2% with MCU values. The pin–by–pin fission densities for three assemblies are compared with the two Monte Carlo values. It is seen that the TRANPIN fission density values show a closer matching with MCU for assemblies N03 & N27 whereas for N21, results are closer to MCNP. The %RMS error in fission density values w.r.t. MCU results is 1.7%, 2.8% & 1.9% for three assemblies. The %RMS error in fission density values w.r.t. MCNP results was seen as 2.3%, 1.8% and 2.7%.

Overall, the use of interface current method to perform large scale whore core calculation in 2D geometry shows a satisfactory performance. As seen from the above

results, the methodology incorporated in TRANPIN shows a promising application to the problems of practical interest.

1.2 Future Work

The work performed in this research is oriented to develop the capability to perform a full scale 3D whole core calculation. The development of high–fidelity tools for solving reactor core neutronics problems that can replace current generation tools used for the design, optimization, safety analysis, and operation of current and future–generation reactors is very challenging. Smith et al [57] has listed the challenges and important aspects of LWR simulation that must be incorporated in truly high–fidelity analysis tools. Current production tools, while low–order in nature, rely on clever mathematical and physical approximations to overcome computing limitations that existed when they were developed [57]. While modern computing eliminates the need for many of these approximations, it is critically important that high–fidelity methods be used with sufficient resolution to actually deliver higher accuracy than the methods they are intended to replace [57].

The use of interface current method in TRANPIN has shown a promising future for realistic problems in 2D geometry and fulfills the above objectives. The interface current method in TRANPIN can be used for performing 3D core calculation. This can be achieved either within the approximate framework of 2D/1D coupling scheme or by developing the interface current method for performing 3D multi assembly calculations. Although, the interface current method introduces some approximations for the angular order of the currents, the interface current method has potential for 3D whole core analysis. The application of interface current method for performing full scale 3D whole core calculation needs further research to develop innovative methods for accurately treating interface currents.

TRANPIN is currently running in serial format. The speed of calculation in TRANPIN can be greatly enhanced by making use of parallel algorithms. The acceleration schemes to accelerate the transport solution can be implemented in TRANPIN and future 3D code. This may include the conventional methods based on coarse mesh finite difference (CMFD) approach or coarse mesh rebalance (CMR) and their higher order variants.

A very important requirement for performing the reactor physics calculation in 2D/3D geometry is the accurate treatment of cross section in resonance energy region. TRANPIN, currently, uses the multigroup cross section libraries in WIMS format. Stammler's model is used for treating self shielded cross sections in resonance energy range. Customized nuclear data libraries for thermal, intermediate and fast spectrum can be developed and used for different applications to retain the accuracy in respective applications. The resonance self–shielding and mutual shielding models based on sub group approach can be developed and used for preparation of cross section in resonance energy range.

A fuel depletion module to perform the 2D/3D burnup calculation can be added to TRANPIN and its 3D variant. The future 3D code can be used to study the fuel cycle characteristics of VVER–1000 MWe reactors currently operating at Kudankulam, Tamilnadu, India and other indigenous fuel cycle study requirements.

APPENDIX A

EXPRESSIONS FOR DIFFERENT COMPONENTS OF TRANSMISSION PROBABILITY

The general formula for transmission probability from surface β to surface α, in Eq. (2.50), is written in 2D geometry as

$$P_{\alpha\beta}^{\nu\mu} = \frac{2}{\pi S_\alpha}\int_0^{2\pi} d\phi \int_0^{\frac{\pi}{2}} d\vartheta \int_{y_{min}}^{y_{max}} dy \sin^2\vartheta\, \psi^\nu\left(\overrightarrow{\Omega}, \overrightarrow{n_+}\right) \psi^\mu\left(\overrightarrow{\Omega}, \overrightarrow{n_-}\right) e^{-\frac{\tau_{\alpha\beta}}{\sin\vartheta}}. \tag{A.1}$$

The different components of transmission probability are obtained using expansion functions for incoming and outgoing angular flux in Eq. (2.32) in above equation. For different combinations of μ and ν following expressions are obtained:

$$P_{\alpha\beta}^{00} = \frac{2}{\pi S_\alpha}\int d\phi \int dy\ Ki_3(\tau). \tag{A.2}$$

$$P_{\alpha\beta}^{01} = \frac{4}{\pi S_\alpha}\int d\phi \int dy\ \sin\omega_\alpha\ Ki_4(\tau). \tag{A.3}$$

$$P_{\alpha\beta}^{10} = \frac{4}{\pi S_\alpha}\int d\phi \int dy\ \sin\omega_\beta\ Ki_4(\tau). \tag{A.4}$$

$$P_{\alpha\beta}^{11} = \frac{8}{\pi S_\alpha}\int d\phi \int dy\ \sin\omega_\alpha \sin\omega_\beta\, Ki_5(\tau). \tag{A.5}$$

$$P_{\alpha\beta}^{20} = -2\sqrt{2}\, P_{\alpha\beta}^{00} + \frac{6\sqrt{2}}{\pi S_\alpha}\int d\phi \int dy\ \cos\phi_\beta\, Ki_4(\tau). \tag{A.6}$$

$$P_{\alpha\beta}^{02} = -2\sqrt{2}\, P_{\alpha\beta}^{00} + \frac{6\sqrt{2}}{\pi S_\alpha}\int d\phi \int dy\ \cos\omega_\alpha\, Ki_4(\tau). \tag{A.7}$$

$$P_{\alpha\beta}^{21} = -2\sqrt{2}\, P_{\alpha\beta}^{01} + \frac{12\sqrt{2}}{\pi S_\alpha}\int d\phi \int dy\ \sin\omega_\alpha \cos\omega_\beta\, Ki_5(\tau). \tag{A.8}$$

$$P_{\alpha\beta}^{12} = -2\sqrt{2}\, P_{\alpha\beta}^{10} + \frac{12\sqrt{2}}{\pi S_\alpha}\int d\phi \int dy\ \sin\omega_\beta \cos\omega_\alpha\, Ki_5(\tau). \tag{A.9}$$

$$P_{\alpha\beta}^{22} = -8\, P_{\alpha\beta}^{00} - 2\sqrt{2}(P_{\alpha\beta}^{02} + P_{\alpha\beta}^{20}) + \frac{36}{\pi S_\alpha}\int d\phi \int dy\ \cos\omega_\alpha \cos\omega_\beta\, Ki_5(\tau). \tag{A.10}$$

$$P_{\alpha\beta}^{03} = \frac{1}{\sqrt{17}}\left[-15\,P_{\alpha\beta}^{00} - 2\sqrt{2}\,P_{\alpha\beta}^{02} + \frac{40}{\pi S_\alpha}\int d\phi \int dy\;\; Ki_5(\tau)\right]. \quad (A.11)$$

$$P_{\alpha\beta}^{30} = \frac{1}{\sqrt{17}}\left[-15\,P_{\alpha\beta}^{00} - 2\sqrt{2}\,P_{\alpha\beta}^{20} + \frac{40}{\pi S_\alpha}\int d\phi \int dy\;\; Ki_5(\tau)\right]. \quad (A.12)$$

$$P_{\alpha\beta}^{31} = \frac{1}{\sqrt{17}}\left[-15\,P_{\alpha\beta}^{01} - 2\sqrt{2}\,P_{\alpha\beta}^{21} + \frac{80}{\pi S_\alpha}\int d\phi \int dy \sin\omega_\alpha\;\; Ki_6(\tau)\right]. \quad (A.13)$$

$$P_{\alpha\beta}^{13} = \frac{1}{\sqrt{17}}\left[-15\,P_{\alpha\beta}^{10} - 2\sqrt{2}\,P_{\alpha\beta}^{12} + \frac{80}{\pi S_\alpha}\int d\phi \int dy \sin\omega_\beta\;\; Ki_6(\tau)\right]. \quad (A.14)$$

$$P_{\alpha\beta}^{32} = \frac{1}{\sqrt{17}}\left[-15\,P_{\alpha\beta}^{02} - 2\sqrt{2}\,P_{\alpha\beta}^{22} + \frac{40\sqrt{2}}{\pi S_\alpha}\int d\phi \int dy\,(3\cos\omega_\alpha\;\; Ki_6(\tau) - 2\,Ki_5(\tau))\right]. \quad (A.15)$$

$$P_{\alpha\beta}^{23} = \frac{1}{\sqrt{17}}\left[-15\,P_{\alpha\beta}^{20} - 2\sqrt{2}\,P_{\alpha\beta}^{22} + \frac{40\sqrt{2}}{\pi S_\alpha}\int d\phi \int dy\,(3\cos\omega_\beta\;\; Ki_6(\tau) - 2\,Ki_5(\tau))\right]. \quad (A.16)$$

$$P_{\alpha\beta}^{33} = \frac{1}{17}\Big[209\,P_{\alpha\beta}^{00} - 2\sqrt{2}\left(P_{\alpha\beta}^{02} + P_{\alpha\beta}^{20}\right) - 2\sqrt{34}\left(P_{\alpha\beta}^{23} + P_{\alpha\beta}^{32}\right) + \frac{400}{\pi S_\alpha}\int d\phi \int dy\,(2\,Ki_7(\tau) - 3\,Ki_5(\tau))\Big] \quad (A.17)$$

$$P_{\alpha\beta}^{40} = \frac{2\sqrt{306}}{51\,\pi S_\alpha}\int d\phi \int dy\left[\left(51cos^2\omega_\beta - 2\right)Ki_5(\tau) - 60\cos\omega_\beta\,Ki_4(\tau) + 16Ki_3(\tau)\right]. \quad (A.18)$$

$$P_{\alpha\beta}^{04} = \frac{2\sqrt{306}}{51\,\pi S_\alpha}\int d\phi \int dy\,[(51cos^2\omega_\alpha - 2)Ki_5(\tau) - 60\cos\omega_\alpha\,Ki_4(\tau) + 16Ki_3(\tau)]. \quad (A.19)$$

$$P_{\alpha\beta}^{41} = \frac{4\sqrt{306}}{51\,\pi S_\alpha}\int d\phi \int dy\left[\left(51cos^2\omega_\beta - 2\right)Ki_6(\tau) - 60\cos\omega_\beta\,Ki_5(\tau) + 16Ki_4(\tau)\right]\,\sin\omega_\alpha. \quad (A.20)$$

$$P_{\alpha\beta}^{14} = \frac{4\sqrt{306}}{51\,\pi S_\alpha}\int d\phi \int dy\,[(51cos^2\omega_\alpha - 2)Ki_6(\tau) - 60\cos\omega_\alpha\,Ki_5(\tau) + 16Ki_4(\tau)]\sin\omega_\beta\,. \quad (A.21)$$

$$P_{\alpha\beta}^{42} = \frac{2\sqrt{2}\sqrt{306}}{51\,\pi S_\alpha}\int d\phi \int dy \left[\left(153cos^2\omega_\beta - 6\right)\cos\omega_\alpha\, Ki_6(\tau)\right.$$

$$+ \left(4 - 102cos^2\omega_\beta - 180\cos\omega_\alpha\cos\omega_\beta\right)Ki_5(\tau)$$

$$\left. + \left(48\cos\omega_\alpha + 120\cos\omega_\beta\right)Ki_4(\tau) - 32Ki_3(\tau)\right]. \qquad \text{(A. 22)}$$

$$P_{\alpha\beta}^{24} = \frac{2\sqrt{2}\sqrt{306}}{51\,\pi S_\alpha}\int d\phi \int dy \left[(153cos^2\omega_\alpha - 6)\cos\omega_\beta\, Ki_6(\tau) + (4 - 102cos^2\omega_\alpha\right.$$

$$- 180\cos\omega_\alpha\cos\omega_\beta)Ki_5(\tau) + \left(48\cos\omega_\beta + 120\cos\omega_\alpha\right)Ki_4(\tau)$$

$$\left. - 32Ki_3(\tau)\right]. \qquad \text{(A. 23)}$$

$$P_{\alpha\beta}^{43} = \frac{2\sqrt{306}}{51\sqrt{17}\,\pi S_\alpha}\int d\phi \int dy \left[20\left(51cos^2\omega_\beta - 2\right)Ki_7(\tau) - 12\left(51cos^2\omega_\beta\cos\omega_\alpha +\right.\right.$$

$$\left.100\cos\omega_\beta - 2\cos\omega_\alpha\right)Ki_6(\tau) + (720\ \cos\omega_\alpha\cos\omega_\beta - 357cos^2\omega_\beta + 334)Ki_5(\tau) +$$

$$\left.\left(420\cos\omega_\beta - 192\cos\omega_\alpha\right)Ki_4(\tau) - 112Ki_3(\tau)\right]. \qquad \text{(A.24)}$$

$$P_{\alpha\beta}^{34} = \frac{2\sqrt{306}}{51\sqrt{17}\,\pi S_\alpha}\int d\phi \int dy \left[20(51cos^2\omega_\alpha - 2)Ki_7(\tau) - 12\left(51cos^2\omega_\alpha\cos\omega_\beta +\right.\right.$$

$$\left.100\cos\omega_\alpha - 2\cos\omega_\beta\right)Ki_6(\tau) + (720\ \cos\omega_\alpha\cos\omega_\beta - 357cos^2\omega_\alpha + 334)Ki_5(\tau) +$$

$$\left.\left(420\cos\omega_\alpha - 192\cos\omega_\beta\right)Ki_4(\tau) - 112Ki_3(\tau)\right]. \qquad \text{(A.25)}$$

$$P_{\alpha\beta}^{44} = \frac{2X306}{51^2\,\pi S_\alpha}\int d\phi \int dy \left[(51cos^2\omega_\alpha - 2)\left(51cos^2\omega_\beta - 2\right)Ki_7(\tau)\right.$$

$$- 60\left(51cos^2\omega_\alpha\cos\omega_\beta + 51cos^2\omega_\beta\cos\omega_\alpha - 2\cos\omega_\alpha - 2\cos\omega_\beta\right)Ki_6(\tau)$$

$$+ 16\left(51cos^2\omega_\alpha + 51cos^2\omega_\beta + 225\cos\omega_\alpha\cos\omega_\beta - 4\right)Ki_5(\tau)$$

$$\left. - 960\left(\cos\omega_\alpha + \cos\omega_\beta\right)Ki_4(\tau) + 256Ki_3(\tau)\right] \qquad \text{(A. 26)}$$

$$P_{\alpha\beta}^{50} = \frac{1}{\sqrt{11}}\left[-8\,P_{\alpha\beta}^{10} + \frac{60}{\pi S_\alpha}\int d\phi \int dy \cos\omega_\beta \sin\omega_\beta\ Ki_5(\tau)\right]. \qquad \text{(A.27)}$$

$$P_{\alpha\beta}^{05} = \frac{1}{\sqrt{11}}\left[-8\,P_{\alpha\beta}^{01} + \frac{60}{\pi S_\alpha}\int d\phi \int dy \cos\omega_\alpha \sin\omega_\alpha\ Ki_5(\tau)\right]. \qquad \text{(A.28)}$$

$$P_{\alpha\beta}^{51} = \frac{1}{\sqrt{11}}\left[-8\,P_{\alpha\beta}^{11} + \frac{120}{\pi S_\alpha}\int d\phi \int dy \sin\omega_\alpha \sin\omega_\beta \cos\omega_\beta\, Ki_6(\tau)\right]. \quad \text{(A.29)}$$

$$P_{\alpha\beta}^{15} = \frac{1}{\sqrt{11}}\left[-8\,P_{\alpha\beta}^{11} + \frac{120}{\pi S_\alpha}\int d\phi \int dy \sin\omega_\alpha \sin\omega_\beta \cos\omega_\alpha\, Ki_5(\tau)\right]. \quad \text{(A.30)}$$

$$P_{\alpha\beta}^{52} = \frac{4\sqrt{2}}{\sqrt{11}}\left[\frac{1}{\pi S_\alpha}\int d\phi \int dy \left[45\cos\omega_\alpha \cos\omega_\beta \sin\omega_\beta\, Ki_6(\tau) - (24\cos\omega_\alpha + 30\cos\phi_\beta)\sin\omega_\beta\, Ki_5(\tau)\right] + 4\,P_{\alpha\beta}^{10}\right]. \quad \text{(A.31)}$$

$$P_{\alpha\beta}^{25} = \frac{4\sqrt{2}}{\sqrt{11}}\left[\frac{1}{\pi S_\alpha}\int d\phi \int dy \left[45\cos\omega_\alpha \cos\omega_\beta \sin\omega_\alpha\, Ki_6(\tau) - \left(24\cos\omega_\beta + 30\cos\omega_\alpha\right)\sin\omega_\alpha\, Ki_5(\tau)\right] + 4\,P_{\alpha\beta}^{01}\right]. \quad \text{(A.32)}$$

$$P_{\alpha\beta}^{53} = \frac{1}{\sqrt{17}\sqrt{11}}\left[\frac{4}{\pi S_\alpha}\int d\phi \int dy \left[300\cos\omega_\beta \sin\omega_\beta\, Ki_7(\tau) - \left(180\cos\omega_\alpha \cos\omega_\beta + 160\right)\sin\omega_\beta\, Ki_6(\tau) + (96\cos\omega_\alpha - 105\cos\omega_\beta)\sin\omega_\beta\, Ki_5(\tau)\right] + 56P_{\alpha\beta}^{10}\right]. \quad \text{(A.33)}$$

$$P_{\alpha\beta}^{35} = \frac{1}{\sqrt{17}\sqrt{11}}\left[\frac{4}{\pi S_\alpha}\int d\phi \int dy \left[300\cos\omega_\alpha \sin\omega_\alpha\, Ki_7(\tau) - \left(180\cos\omega_\alpha \cos\omega_\beta + 160\right)\sin\omega_\alpha\, Ki_6(\tau) + \left(96\cos\omega_\beta - 105\cos\omega_\alpha\right)\sin\omega_\alpha\, Ki_5(\tau)\right] + 56P_{\alpha\beta}^{01}\right]. \quad \text{(A.34)}$$

$$P_{\alpha\beta}^{54} = \frac{4\sqrt{306}}{51\sqrt{11}}\left[\frac{1}{\pi S_\alpha}\int d\phi \int dy \left[15(51cos^2\omega_\alpha - 2)\cos\omega_\beta \sin\omega_\beta\, Ki_7(\tau) - \left(408\,cos^2\omega_\alpha + 900\cos\omega_\alpha \cos\omega_\beta - 16\right)\sin\omega_\beta\, Ki_6(\tau) + (480\cos\omega_\alpha + 240\cos\omega_\beta)\sin\omega_\beta\, Ki_5(\tau)\right] - 32P_{\alpha\beta}^{10}\right]. \quad \text{(A.35)}$$

$$P_{\alpha\beta}^{45} = \frac{4\sqrt{306}}{51\sqrt{11}}\left[\frac{1}{\pi S_\alpha}\int d\phi \int dy \left[15\left(51cos^2\omega_\beta - 2\right)\cos\omega_\alpha \sin\omega_\alpha\, Ki_7(\tau) - \left(408\, cos^2\omega_\beta + 900\cos\omega_\alpha \cos\omega_\beta - 16\right)\sin\omega_\alpha\, Ki_6(\tau) + (480\cos\omega_\beta + 240\cos\omega_\alpha)\sin\omega_\alpha\, Ki_5(\tau)\right] - 32P_{\alpha\beta}^{01}\right]. \quad \text{(A.36)}$$

$$P_{\alpha\beta}^{55} = \frac{1}{11}\left[\frac{8}{\pi S_\alpha}\int d\phi \int dy \left[225\cos\omega_\alpha \sin\omega_\alpha \cos\omega_\beta \sin\omega_\beta\, Ki_7(\tau) - 120\left(\cos\omega_\alpha + \cos\omega_\beta\right)\sin\omega_\alpha \sin\omega_\beta\, Ki_6(\tau)\right] + 64P_{\alpha\beta}^{11}\right]. \quad \text{(A. 37)}$$

All the above expressions are required in the discretized current equation. It is to be noted, however, that all of the above expressions need not be evaluated numerically. The numerical evaluation of these expressions is optimized using the reciprocity relations satisfied by them.

APPENDIX B

METHOD OF RAY TRACKING

A large part of the computational effort in two dimensional collision probability calculations is incurred in the evaluation of the coefficient matrices of collision probabilities. The collision probability integrals in two dimensions depend on azimuthal angle and space variable *y*. These integrals are numerically evaluated by trapezoidal rule or other quadrature formula. This is normally known as ray tracing. For present study, we have adopted equidistant ray tracing method. In this method, parallel rays are drawn for each angle and their intersection with the hexagon or circular regions are found. The coordinate system used for ray tracing is shown in Fig. A.1. The origin is taken as the centre of hexagon or circle.

A.1 Definition of tracking line

For calculating tracks inside hexagon or circle, we need to find the intersection points with sides of hexagon and circles. The tracking line is uniquely defined by a point on the line

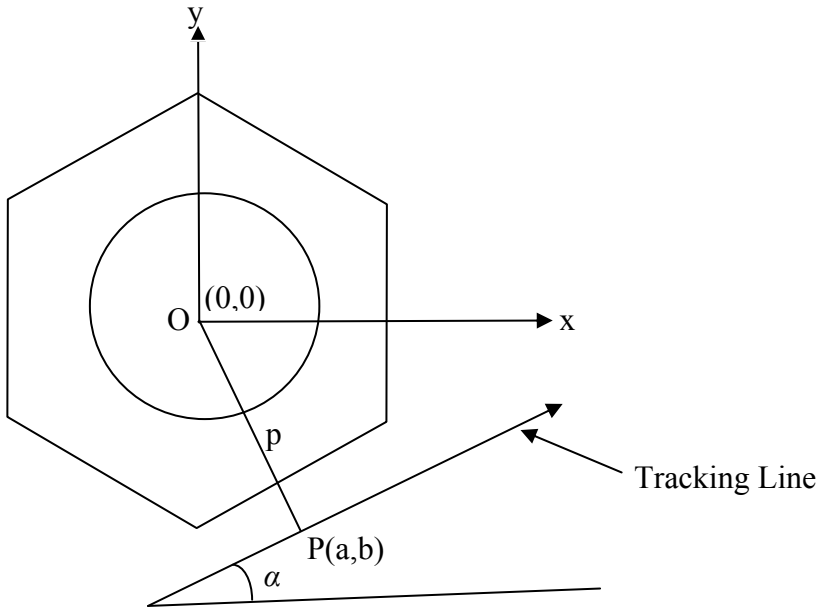

Fig. B.1 Definition of origin

and its slope. The tracking line is shown in the Figure A.1. Its slope is defined by $m_1 = \tan\alpha$. We have to define a point on this line to uniquely define it. For this a perpendicular OP is drawn on the tracking line from origin O.

If p is the length and (a, b) are the coordinates of the foot of perpendicular, then slope of perpendicular is given as

$$m_2 = -\frac{1}{m_1}$$

Equation of perpendicular line $y = m_2 x + c$

Since it passes through origin O, so *c=0*. Point P also lies on this perpendicular line. So

$$b = m_2 a$$

Now, distance between points O & P is p. so

$$a^2 + b^2 = p^2$$

$$a^2 + a^2 m_2^2 = p^2$$

$$a = \frac{p}{\sqrt{(1 + m_2^2)}} = \frac{m_1 p}{\sqrt{(1 + m_1^2)}}$$

$$b = m_2 a = \frac{-p}{\sqrt{(1 + m_1^2)}}$$

The coordinates (a, b) and slope m_1 uniquely define the tracking line. The value of p is chosen initially as the side of hexagon for the hexagonal cell.

A.2 Intersection of tracking line with Circle

Once the tracking line is defined, its intersection points are computed with each circular region. A circle is uniquely defined by coordinates of its centre (*p, q*) and radius *r*. The equation of circle is given as

$$(x - p)^2 + (y - q)^2 = r^2$$

For a line passing through point (x_a, y_a) and slope *m* we first calculate

$$c = y_a - mx_a$$

then we calculate following quantities

$$A = 1 + m^2$$

$$B = 2m(c - q) - 2p$$

$$C = p^2 + (c - q)^2 - r^2$$

$$D = B^2 - 4AC$$

If $D > 0$, the line intersects the circle. The two points of intersection are given as

$$x_1 = \frac{-B + \sqrt{D}}{2A}; y_1 = mx_1 + c.$$

$$x_2 = \frac{-B - \sqrt{D}}{2A}; y_2 = mx_2 + c.$$

These points are stored and then sorted in increasing or decreasing order. If the tracking line is vertical (slope=∞) then considering equation of line $x=k$, we calculate

$$D = r^2 - (k - p)^2$$

If $D > 0$, the line intersects the circle. The two points of intersection are given as

$$x_1 = k; y_1 = p + \sqrt{D}$$

$$x_2 = k \; ; y_2 = p - \sqrt{D}$$

After computing intersection points, the track length in a circle is computed as

$$t = \sqrt{(x_2 - x_1)^2 + (y_2 - y_1)^2}$$

A.3 Intersection of tracking line with Hexagon

The intersection of tracking line with hexagon involves the intersection of line with hexagonal surfaces. The surfaces of hexagon are numbered as shown in Fig. A.2. If the line crosses the hexagon, it will intersect any two surfaces defining the hexagon. The equations of surfaces of hexagon are stored and intersection with each surface is checked at a time. Here we will describe the method to calculate the point of intersection of two lines.

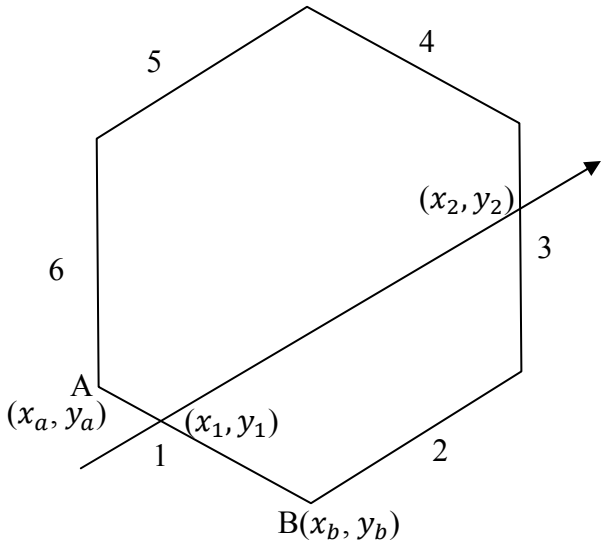

Fig. B.2 Surfaces of Hexagon

If $A_1x + B_1y = C_1$ and $A_2x + B_2y = C_2$ are the equations of two lines, then we calculate

$$D = A_1B_2 - A_2B_1$$

If $|D|$>0, the lines intersect and the point of intersection is give as

$$x = \frac{C_1 B_2 - C_2 B_1}{D} \; ; y = \frac{C_1 A_2 - C_2 A_1}{D}$$

The hexagon surface is defined by two vertices. For surface AB, as shown in Fig. A.2, the slope of the surface can be obtained using

$$m_{AB} = \frac{y_b - y_a}{x_b - x_a}$$

The intercept on *y*-axis can be obtained

$$c_{AB} = y_b - m_{AB} x_b$$

Now the equation of line can be written as

$$y = m_{AB} x - c_{AB}$$

or rearranging

$$-m_{AB} x + y = -c_{AB}$$

Thus

$$A_1 = -m_{AB}, B_1 = 1, C_1 = -c_{AB}$$

Similarly for tracking line defined in section A.1, we have

$$A_2 = -m_1, B_2 = 1, C_2 = -c \;\; where \; c = b - m_1 a$$

The intersection point can be found using above formula. Once the intersection point is calculated, we have to check whether it lies on hexagon. For this purpose, we will compare (*x, y*) with the coordinates of the vertices of that surface. If the line intersects, say, surface AB (Fig. A.2), then point (*x, y*) will lie on hexagon if x lies between x_a & x_b and y lies between y_a & y_b. After checking the intersection with all six sides, we get two points of intersections denoted by (x_1, y_1) and (x_2, y_2) in Fig. A.2. Now we want to know which

surface of the hexagon is intersected first. For this purpose, we arrange both x_1 and x_2 intersection points in increasing order of their magnitude. With these points we have associated surface numbers 1 and 2. This order of their magnitude will give us the order and number of the surfaces encountered. The track length inside hexagon is again given by the formula

$$t = \sqrt{(x_2 - x_1)^2 + (y_2 - y_1)^2}$$

The above procedure is repeated for all angles and all parallel lines of an angle. The coordinates of intersection are stored for calculation of optical length in each energy group with different total cross section.

After tracking the full geometry, the volume of each zone is numerically computed. The formula for numerical volume is given by

$$V_i^{num} = \frac{1}{\alpha} \sum_m \sum_n w_A^m \, w_y^n \, t_i^{m,n}$$

where t_i is the track length in region i and α is the angle of integration. The ratio between true and numerically integrated volume is a measure of integration accuracy and serves as a numerical check for detecting any anomaly in ray tracing.

BIBLIOGRAPHY

1. http://www.npcil.nic.in/main/allprojectoperationdisplay.aspx (Accessed on February 13, 2017)
2. Jain S K, "Nuclear Power in India – Past, present and future", http://www.npcil.nic.in /pdf/CMD_paper_07dec2010.pdf (2010) (Accessed on February 13, 2017)
3. Aragones J. M., Diop C., Rohde U., "Status and limits of current methods for plant analysis", Nuclear Reactor Integrated Simulation Project (NURISP)–Document D-1.0 (issued on 22/3/2010).
4. Tada K., "Study on pin–by–pin fine mesh core calculation method for BWR core analysis," Ph.D. thesis, Nagoya University, (2012).
5. Thilagam L., Sunny S. C., Jagannathan V. and Subbaiah K.V.," A VVER–1000 LEU and MOX assembly computational benchmark analysis using the lattice burnup code EXCEL", *Ann. Nucl. Energy*, 36, **505** (2009).
6. Jagannathan V., Mohanakrishnan P, Menon S. V. G. and Gupta H. C., 'A Fast and Reliable Calculation Model for BWR Fuel Assembly Burnup Analyses', *Ann. Nucl. Energy*, **7**, 641 (1980).
7. Krishnani P. D., "CLUB–A multigroup Integral Transport theory code for analysis of cluster lattices", *Ann. Nucl. Energy*, **9**, 255 (1982).
8. Mohankrishnan P., "Choice of angular current approximations for solving neutron transport problems in 2–D by interface current approach", *Ann. Nucl. Energy*, **9**, 261 (1982).
9. Krishnani P. D., "Analysis of 2–D LWR Benchmarks with an Interface Current Method for Solving the Integral Transport Equation", *Ann. Nucl. Energy*, **14**, 463 (1987).

10. Jagannathan V., Khan S. A. and Mathur A., "VISWAM–A Modular Code System for State of Art Analysis of Nuclear Reactors–Developmental Ideas and Current Status", *Proc. of ARP 2013–Advance in Reactor Physics: Simulation Techniques and Analysis Methodologies,* BARC Training School Hostel, Anushaktinagar, Mumbai, India, October 23–25, 2013 (2013)

11. Jagannathan V., Khan S. A. and Mathur A., "Recent Advances in 3D Core Diffusion Code TRIHEX–FA", *Proc. of ARP 2013–Advance in Reactor Physics: Simulation Techniques and Analysis Methodologies,* BARC Training School Hostel, Anushaktinagar, Mumbai, India, October 23–25, 2013 (2013)

12. Jagannathan V., Kulkarni A. K. and Jain R. P., "COMESH–A Corner Mesh Finite Difference Code To Solve Multi–group Diffusion Equations in Multi dimensions", *BARC Report*, B.A.R.C.–1367, Bhabha Atomic Research Centre, Mumbai, India (1987).

13. Jagannathan V., Krishnani P. D., Jain R. P., Kumar V., Gupta H. C., "The PHANTOM-CEMESH Code System For PHWR Design Computations", *BARC Report*, B.A.R.C.–1444, Bhabha Atomic Research Centre, Mumbai, India (1988).

14. Khan S. A. and Jagannathan V., "HEXPIN–A Pin–by–Pin 3D Core Diffusion Code with Space–Dependent Feedback Model", *Proc. of ARP 2013–Advance in Reactor Physics: Simulation Techniques and Analysis Methodologies,* BARC Training School Hostel, Anushaktinagar, Mumbai, India, October 23–25, 2013 (2013)

15. Kumar A. and Srivenkatesan R**.**, "Nodal Expansion Method for Reactor Core Calculation," *BARC Report*, BARC–1249, Bhabha Atomic Research Centre, Mumbai, India (1984).

16. Gupta A. and Modak R.S., “ATES3: Anisotropic Transport Equation Solver in 3D”, *Proc. of 16th annual meeting of Indian Nuclear Society (INSAC–05)*, Mumbai, Nov. 15–18, 2005 (2005).

17. Gupta A., "ARCH: A 3D Space–Time Analysis Code in Cartesian and Hexagonal Geometries", *Proc. of 19th National Symposium on Radiation Physics (NSRP–19)*, Dec 12–14, 2012, Mamallapuram, TN, India (2012)

18. Sanchez R., “Prospects In Deterministic Three–Dimensional Whole–Core Transport Calculations”, *Nuclear Engineering and Technology*, **44**, 2 (2012)

19. Smith K.S. and Rhodes J.D., “CASMO–4 characteristic method for two–dimensional PWR and BWR core calculations,” *Trans. Am. Nucl. Soc*., **83**, 294 (2000.)

20. Smith K.S. and Rhodes III J.D., “Full–Core 2–D LWR Core Calculations with CASMO–4E,” *Proc. Int. Conf. on Reactor Physics Safety and High-Performance Computing (PHYSOR 2002)*, Seoul, Korea, 7–10 October, 2002 (2002).

21. Lee G.S., Cho N.Z., Hong S.G., “Whole–Core Heterogeneous Transport Calculations and Their Comparisons with Diffusion Results,” *Proceedings of the Korean Nuclear Society Spring Meeting*, Kori, Korea, May 2000 (2000)

22. Joo H. G., Cho J. Y., Kim K. S., Lee C. C. and Zee S. Q., “Methods and Performance of a Three–Dimensional Whole–Core Transport Code DeCART”, *Proc. Int. Conf. on The Physics of Fuel Cycles and Advanced Nuclear Systems: Global Developments (PHYSOR 2004)* Chicago, Illinois, April 25–29, 2004 (2004)

23. Zhong Z., Downar T.J., Joo H.G., Cho J.Y., “Benchmark Analysis of the DeCART MOC Code with the VENUS–2 Critical Experiment”, *Proc. Int. Conf. on The Physics of Fuel Cycles and Advanced Nuclear Systems: Global Developments (PHYSOR 2004)* Chicago, Illinois, April 25–29, 2004 (2004)

24. Cho J Y., Kim K S., Shim H J., Song J S., Lee C C. and Joo H G., "Whole Core Transport Calculation Employing Hexagonal Modular Ray Tracing and CMFD Formulation," *Journal of Nucl. Sci. and Technology*, **45**, 740–751 (2008)

25. Kucukboyaci V.N., Ouisloumen M., and Franceschini F., "Two–Dimensional Whole Core Transport calculations using PARAGON," *Proc. Int. Conf. on Mathematics,Computational Methods & Reactor Physics (M&C 2009)*, Saratoga Springs, New York, May 3–7, 2009. (2009)

26. Sanchez R., Zmijarevic I., Coste-Delclaux M., Masiello E., Santandrea S., Martinolli E., Villate L., Schwartz N. and Guler N., "APOLLO2 YEAR 2010', *Nuclear Engineering and Technology*, **42**, 5 (2010)

27. Yang X. and Satvat N., "MOCUM: A two–dimensional method of characteristics code based on constructive solid geometry and unstructured meshing for general geometries", *Ann. Nucl. Energy*, **46**, 20, (2012)

28. Altiparmakov D. and Wiersma R. "The Collision Probability Method in Today's Computer Environment", *Nucl. Sci. Eng*, **182**, 395 (2016).

29. Prabha H., Marleau G., "Computation of 3D neutron fluxes in one pin hexagonal cell", *Ann. Nucl. Energy*, **56**, 1, (2013)

30. Prabha H., Marleau G, Hébert A., "Tracking algorithms for multi-hexagonal assemblies (2D and 3D)", *Ann. Nucl. Energy* , **69**, 175, (2014)

31. Khan S. A., Jagannathan V., Pal U., Karthikeyan R. and Srivastava A., "Need for High Temperature Nuclear Data Library for LWR Design Computations", *Journal of the Korean Physical Society*, Vol. **59**, No. 1, July 2011 (2011)

32. WIMS Library Update Project – https://www–nds.iaea.org/wimsd/(Accessed on September 15, 2015)

33. Edenius M., Forssen B.H., Häggblom H., "Physics model development in CASMO", *In Int. Conf. Physics of Reactors: Operation, Design and Computation*, Marseille, France, P.IV–25 (1990).

34. Weiss Z.J. and Stamm'ler R.J.J., "Nodal coupling of heterogeneous pin cells", *Trans. Am. Nucl. Soc*. **26**, 223 (1977).

35. Kavenoky A. and Sanchez R., "The APOLLO assembly spectrum code", *In Int. Topl. Mtg. Advances in Reactor Physics, Mathematics and Computation*, Paris, France, 1461 (1987).

36. Marleau G., Hébert A., Roy R., "*A User Guide for DRAGON Version 4"*, Institut de génie nucléaire, Département de génie mécanique, École Polytechnique de Montréal (2011).

37. Sanchez, R., "A transport multicell method for two–dimensional lattices of hexagonal cells", *Nucl. Sci. Eng*. **92**, 247. (1986)

38. Ouislumen M, Marleau G., Hébert A, Roy R., "Computation of Collision Probabilities for Mixed Hexagonal-Cylindrical Cells Using the DP1 Approximation to the $J_{\pm}$ technique", *Proc. Int. Topl. Mtg. Advances in Mathematics, Computations, and Reactor Physics*, Pittsburgh, PA, April 28 – May 02, 1991 (1991).

39. Sanchez R. and McCormick N.J., "A Review of Neutron Transport Approximations", *Nucl. Sci. Eng*, **80**, 481 (1982).

40. Sanchez R., "Approximate Solutions of the Two–Dimensional Integral Transport Equation by Collision Probability Methods", *Nucl. Sci. Eng*, **64**, 384 (1977).

41. Marleau G, Dragon Theory Manual Part 1: Collision Probability Calculations, IGE–236 Rev. 1, (2001)

42. Marleau G, "DRAGON Theory for 3D CANDU Problems", Atomic Energy of Canada Limited, (2004)

43. Lewis E.E. and Miller W. F. Jr., *Computational Methods of Neutron Transport*, John Wiley & Sons Inc, New York, (1984)

44. Krishnani P. D., "A Method for Solving Integral Transport Equation for Pressurized Heavy Water Reactor Cluster Geometry", Ph.D. Thesis, University of Bombay, Bombay (1984)

45. Blair J. M., Edwards C. A. and Johnson J. H., "Rational Chebyshev Approximations for the Bickley Functions $Ki_n(x)$", *Mathematics of Computation*, Volume **32**, Number 143, 876-886 (1978)

46. Abramowitz M. and Stegun I.A., *Handbook of Mathematical Functions,* Dover Publications Inc, New York, (1972).

47. Villarino E.A., Stamm'ler R.J.J., Ferri A.A., Casal J.J., "HELIOS: angularly dependent collision probabilities" *Nucl. Sci. Eng*. **112**, 16–31 (1992).

48. Jagannathan V., Khan S. A. and Mathur A., Thilagam L. and Mohapatra D. K., "Analysis of EPR Fuel Assembly by VISWAM and Comparison with DRAGON and MCNP", *Proc. of ARP 2013 – Advance in Reactor Physics: Simulation Techniques and Analysis Methodologies,* BARC Training School Hostel, Anushaktinagar, Mumbai, India, October 23–25, 2013

49. Zhang Z., Rahnema F, Zhang D., Pounders J.M., Ougouag A.M., "Simplified two and three dimensional HTTR benchmark problems", *Ann. Nucl. Energy,* **38**, 1172 (2011).

50. A VVER–1000 LEU and MOX Assembly Computational Benchmark, NEA/NSC/DOC (2002)10, (2002)

51. Stamml'er R.J.J. and Abbate M.J., '*Methods of Steady–State Reactor Physics in Nuclear Design*', Academic Press (1983).

52. Hebert A., "Development of A New Resonance Self-Shielding Methodology Based on Probability Table Information", *Nuclear Mathematical and Computational Sciences: A Century in Review, A Century Anew,* Gatlinburg, Tennessee, April 6-11, 2003, on CDROM, American Nuclear Society, LaGrange Park, IL (2003)

53. Kochunas B. M. "A Hybrid Parallel Algorithm for the 3–D Method of Characteristics Solution of the Boltzmann Transport Equation on High Performance Compute Clusters", Ph.D. Thesis, University of Michigan (2013)

54. Zhang Z., Rahnema F., Pounders J. M., Zhang D. and Ougouag A. "A Simplified 2D HTTR Benchmark Problem", *Proc. Int. Conf. on Mathematics, Computational Methods & Reactor Physics (M&C 2009)*, Saratoga Springs, New York, May 3–7, 2009. (2009)

55. VVER–1000 MOX Core Computational Benchmark, NEA/NSC/DOC 17 (2005)

56. Simeonov T., "Release Notes–Helios System Version 1.8," Studsvik Scandpower Report, *SSP–03/221*, November 26 (2003).

57. Smith K.S. and Forget B., "Challenges in the Development of High-Fidelity LWR Core Neutronics Tools," *Proc. of the International Conference on Mathematics and Computational Methods Applied to Nuclear Science and Engineering (M&C 2013)*, Sun Valley, ID, USA, May 5–9 (2013)